Zeitschrift: Helvetica Physica Acta
Band: 65 (1992)
Heft: 6

Vereinsnachrichten: Rapport de la réunion d'automne de la SSP
Autor: [s.n.]

Helv Phys Acta
Vol. 65 (1992)

0018-0238/92/060820-66$1.50+0.20/0

A Scanning Force Microscopy Investigation of DNA Adsorbed on Mica

F. Zenhausern*, L. M. Eng, M. Adrian+, S. Kasas++,
A. L. Weisenhorn++ and P. Descouts

Group of Applied Physics, University of Geneva, CH-1211 Geneva 4, Switzerland
+Laboratoire d'Analyse Ultrastructurale, University of Lausanne, CH-1015 Dorigny
++Inst. Histology and General Embryology, University of Fribourg, CH-1700 Fribourg

We report on our recent developments in imaging of plasmid DNA attached on a mica substrate by scanning force microscopy (SFM). At a nominal concentration of about 15 molecules/μm^2, several DNA molecules are investigated on a 600 x 600 nm^2 viewing field yielding a good transfer ratio. The measured dimensions of the molecules (length: 840 nm, width: 2.2 nm, height: 0.4 nm) agree reasonably well with the biophysical data after deconvoluting the pictures for tip shape. We directly observed variant features of DNA, including the supercoiling.

The scanning force microscope (SFM) is able to image the surfaces of soft materials in air as well as a liquid with a lateral and vertical resolution inferior to 1 nm [1, 2]. Several groups have attempted to image DNA by SFM but one major difficulty to success has been reliability to locate an isolated molecule of nucleic acid deposited onto a solid substrate [3]. Although the specimen preparation has been the subject of much investigations [4], little is known to understand the processes determining adhesion of DNA at surfaces. Recently, we reported on the adsorption of plasmid DNA on coated magnesium mica, yielding strong enough an interaction to be imaged reproducibly with SFM in air [5]. Here, we adapted this preparation method to supercoiled pUC9 plasmid DNA at high concentration. An uniform coverage of isolated plasmids (fig.1A) was observed providing routinely imaging of DNA molecules down to the nanometer scale. The supercoiled plasmids are bound to the mica substrate by means of an electric double layer of adsorbed ions (Helmholtz layers). Our purpose was to optimize the spreading and to inhibit the motion of the molecules induced by scanning the tip of our SFM. The SFM measurements were performed in air with a Nanoscope II (Digital Instruments, California) installed on a vibration air damped table. We used commercially available V-shaped cantilevers with an integrated pyramidal tip having a total length of 100 μm and a spring constant of 0.37 N/m. These short cantilevers with a relatively large spring constant yield a high image contrast revealing the DNA molecules with a reduced height but an enhanced width (see fig. 1). Figure 1B shows the molecular distortion due to the response of tip load. The corresponding height of DNA molecules measures δz=0.4 nm which is much below the biophysical data. The circular DNA is well discerned in Fig.2, but most of the supercoiling was lost during the adsorption process [7]. Please note, that the force magnitude exerted on the specimen by the tip during a scan was determined to be in the range of 10^{-8} N. When imaging in air, additional forces are present (capillary and hydration forces) due to a thin layer of water and contaminants on the surface of both specimen and tip [6]. The comparison in length, width and height of the DNA molecules with the biophysical data reveals sufficient consistence. Differences in the observed lateral dimensions can be explained by simple geometric arguments due to the radius of curvature of the tip[8]. Hence our SFM results show that reproducible imaging of DNA is possible but limited by tip geometric effects and by elastic deformation of the molecule due to high loadings in air.

* To whom correspondence should be addressed

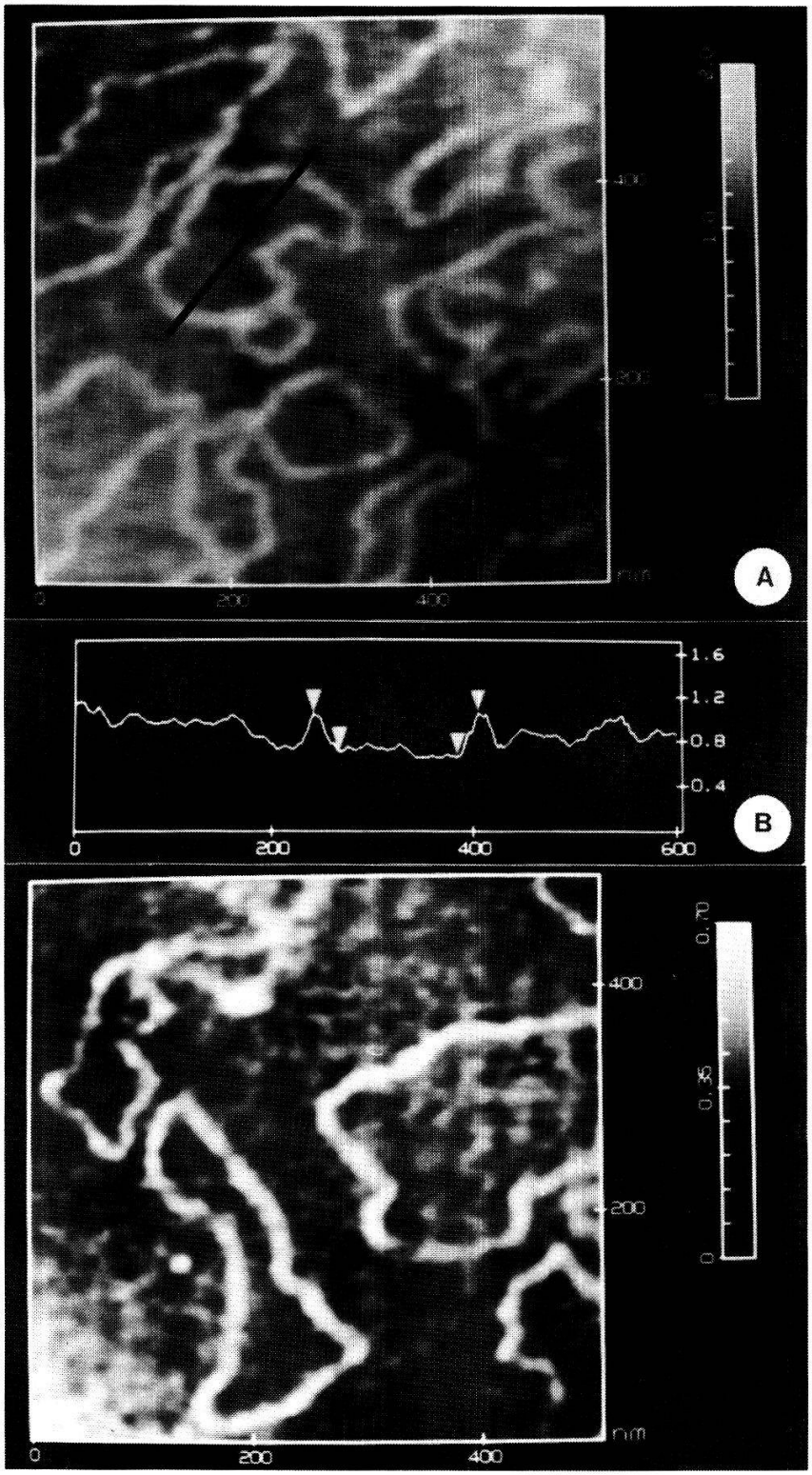

Fig. 1. *(A)* Top view SFM image of pUC9 plasmid DNA (33μg/ml in 30 mM triethanolamine, pH 7.9, 10 mM $MgCl_2$, 0.1% glutaraldehyde) adsorbed on mica in air. *(B)* Cross-section along the black line indicated in *(A)*. The molecular height of DNA is reduced to 0.4 nm while the width measures 20 nm.

Fig. 2. SFM image of isolated double-stranded DNA molecules. One has lost supercoiling during the adsorption process.

REFERENCES

[1] G. Binnig, C. F. Quate, Ch. Gerber, *Phys. Rev. Lett.*, **56**, 930 (1986)

[2] D. Rugar and P. K. Hansma, *Physics Today*, **43**,23 (1990)

[3] H. G. Hansma, A. L. Weisenhorn, S. A. C. Gould, R. L. Sinsheimer, H. E. Gaub, G. D. Stucky, C. M. Zaremba and P. K. Hansma, *J. Vac. Sci. Technol.*,**B9(2)**, 1282 (1991).

[4] P. G. Arscott, V. A. Bloomfield, *Methods in Enzymology*, **Feb. 18**, (1991)

[5] F. Zenhausern, M. Adrian, B. ten Heggeler-Bordier, R. Emch, M. Jobin, M. Taborelli and P. Descouts, *J. Struc. Biology*, **108**, 69, (1992)

[6] A. L. Weisenhorn, P. K. Hansma, T. R. Albrecht and C. F. Quate, *Appl. Phys. Lett.*, **54**, 2651 (1989)

[7] T. H. Eickbush, E. N. Moudrianakis, *Cell*, **13**, 295, (1978)

[8] F. Zenhausern, M. Adrian, R. Emch, M. Taborelli, M. Jobin and P. Descouts, *Ultramicroscopy*, in press, (1992)

Mechanisms of strain relaxation in epitaxial CaF_2/Si(111) studied with atomic force microscopy

S. Blunier[1], H. Zogg[1], C. Maissen[1], A.N. Tiwari[1], R.M. Overney[2], H. Haefke[2], G. Kostorz[3]

[1]AFIF (Arbeitsgemeinschaft für industrielle Forschung) at Swiss Federal Institute of Technology, ETH Hönggerberg, CH-8093 Zürich

[2]Institute of Physics, University of Basel, CH-4056 Basel

[3]Institute of Applied Physics, Swiss Federal Institute of Technology, ETH Hönggerberg, CH-8093 Zürich

Received 7 April 1992

Abstract Atomic force microscopy reveals straight slip steps resulting from dislocation glide in the primary {100}<110> glide system in "low mismatch" CaF_2/Si(111) structures. From the height and spacing of the steps, the strain relieved by misfit dislocations is compatible with ~1.7% tensile thermal mismatch strain change on cool down. In the high mismatch system BaF_2/CaF_2/Si(111) an array of dislocations is observed at the BaF_2/CaF_2 interface by HTEM. These dislocations are most probably sessile and have Burgers vectors parallel to the interface.

CaF_2 grown epitaxially onto Si has attracted attention for potential device applications [1], as buffer layer for overgrowth with different semiconductor films [2], and because of interesting structural and electronic properties of the ionic/covalent interface [3-5]. At room temperature (RT), the lattice constant of CaF_2 is only 0.6% higher than that of Si, while at 750°C (typical for MBE growth) it is as much as 2.4 % higher owing to the different thermal expansion coefficients. The critical thickness for misfit dislocation formation during growth is about 3 nm. Therefore, the lattice misfit strain in 180 nm thick layers is nearly completely relaxed at growth temperature. Thermal mismatch is expected to introduce a high strain upon cool down. However, this strain is also relaxed as first shown by RBS channeling [1]. This must be due to dislocations which are still mobile down to room temperature. The primary glide system in fluorides is {100}<110>.

These dislocations where studied for the first time. Since TEM is rather difficult to perform, we used AFM to image the insulating CaF_2. The images (see figure) show three sets of parallel straight steps with angles of 60° between each set. The line directions correspond to <1-10> directions of the sample, i.e. to the intersections of the {100} glide planes with the (111) surface. We did not observe such lines with AFM on bulk fluorides, and cleavage steps in bulk materials have very different morphologies. All step heights can be explained by multiples of $a/\sqrt{3}$ (a is the lattice constant) i.e. to the spacings of (111) oriented triple F^--Ca^{++}-F^- atomic layers. This corresponds to multiples of the perpendicular projection $b_\perp$ of the a/2<110> Burgers vectors. The heights are consistent with the interpretation that the surface steps are due to glide of one or a few dislocations along an individual {100} glide plane, leaving a slip step behind. Due to the three-fold symmetry, the steps lead to triangular terraces with differences in altitude corresponding to these step heights. Quantitative analysis of the step heights and the spacings leads to the following model of strain relaxation:

The misfit is mainly overcome by glissile dislocations during growth (lattice misfit) and after growth on cool down (thermal misfit). Most probably they nucleate at the surface, glide

down on {100} glide planes, leave a slip step behind, and become misfit dislocations. Their Burgers vector is inclined 54.7° with respect to the surface. The system prefers dislocations acting in the primary glide system although such dislocations do not relieve as much strain as dislocations with Burgers vectors parallel to the interface.

In systems with higher mismatches like $BaF_2/CaF_2/Si(111)$ (14% mismatch, the intermediate CaF_2 serves for compatibility) an array of additional dislocations is observed by HTEM at the CaF_2/BaF_2 interface. These dislocations have Burgers vectors parallel to the interface, they are sessile. The slip steps at the surface observed by AFM are mainly due to the thermal mismatch. A similar behaviour is observed in PbSe layers grown on $BaF_2/CaF_2/Si(111)$.

[1] L.J. Schowalter, R.W. Fathauer, CRC Crit. Rev. Solid State and Mat. Sci. **15**, 367, 1989.

[2] H. Zogg, S. Blunier, T. Hoshino, C. Maissen, J. Masek, and A.N. Tiwari, IEEE Trans. Electron Devices **38**, 1110 (1991).

[3] R.M. Tromp and M.C. Reuter, Phys. Rev. Lett. **61**, 1756 (1988).

[4] J.L. Batstone, J.M. Phillips, and E.C. Hunke, Phys. Rev. Lett. **60**, 1394 (1988); **61**, 2274 (1988).

[5] J. Zegenhagen and J.R. Patel, Phys. Rev. **B41**, 5315 (1990).

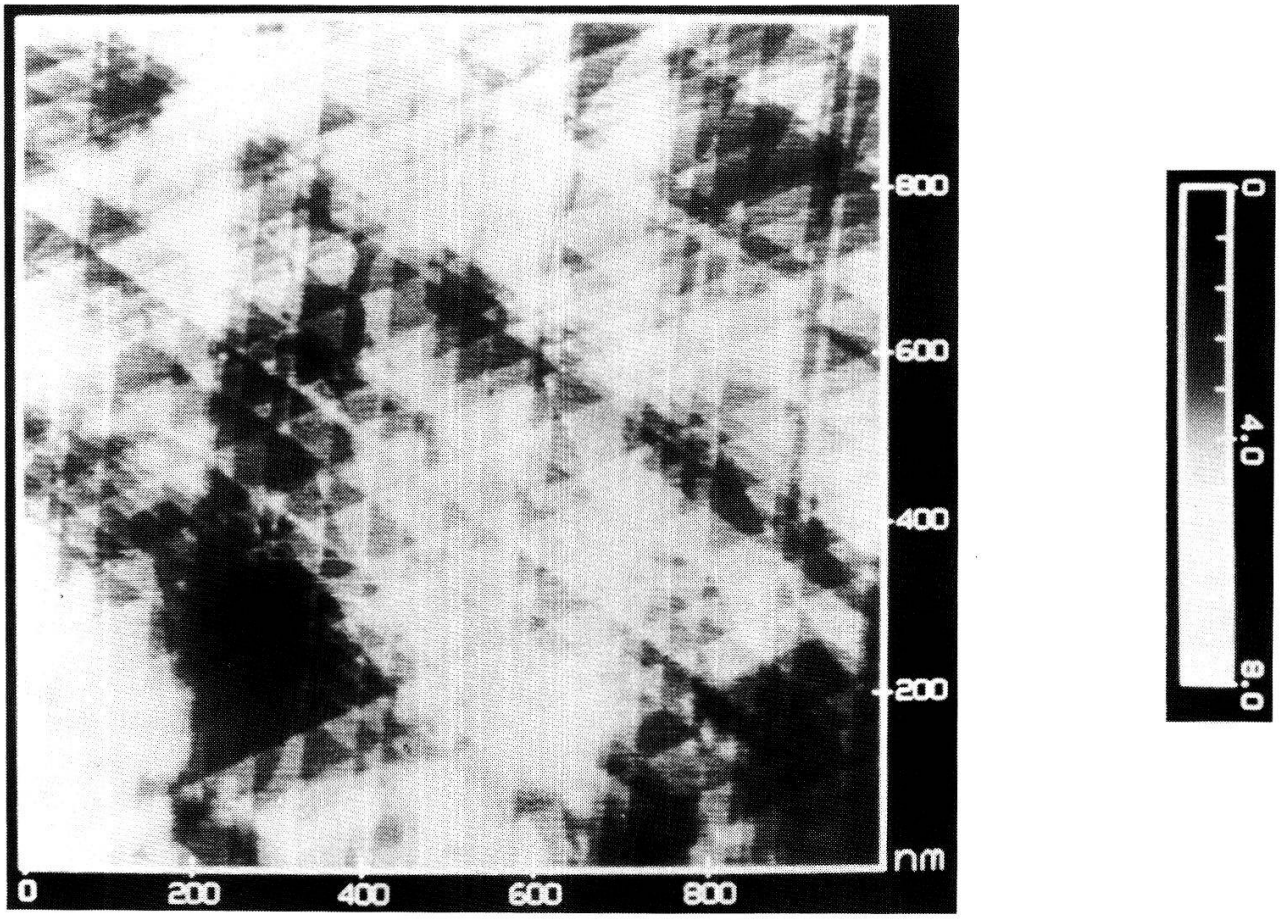

Figure 1. AFM image of a 180 nm thick epitaxial CaF_2 layer on Si(111). The straight slip steps are parallel to the three <1-10> directions. The offsets in height of the triangles within the slip step lines are multiples of the projection of the Burgers vectors.

REAL-TIME CONTROL OF CHAOS WITH HIGH-DIMENSIONAL EMBEDDINGS

C. Reyl•, L. Flepp•, R. Badii*, J. Parisi•, J. Simonet•, R. Holzner• , and E. Brun•

* Paul-Scherrer Institut, LUS, 5232 Villigen PSI
• Physik Institut der Universität, Schönberggasse 9, 8001 Zürich

We proved the usefulness of the Ott-Grebogi-Yorke control method by stabilizing a chaotic NMR-laser system about an unstable period-one orbit. We used a six-dimensional delay-coordinate embedding technique to fully determine the stability properties of the controlled orbit. This analysis yields small time-dependent perturbations of the quality factor capable to perform real-time control.

A nonlinear dynamical system may exhibit chaotic temporal behavior as a suitable control parameter is varied. Elimination of the aperiodicity is often desired. The difficulty of the task is clearly related to the complexity of the dynamics. Ott, Grebogi and Yorke (OGY) [1] put forward the idea to use the properties of a chaotic system, i.e., the sensitivity to small perturbations and the ergodicity of the motion, in order to control the dynamics. Control means steering the system so as to bring it close to a determined unstable orbit. This can be achieved by an intelligent feedback technique in which small, carefully chosen, time-dependent perturbations are supplied to one of the control parameters.

We start from the assumption that a chaotic attractor is interspersed with an infinite number of dense unstable periodic orbits, providing a convenient reservoir of possible trajectories to stabilize on. The goal is to hold the chaotic motion close to such an unstable orbit and not to force the system to follow some arbitrary periodic perturbation. This is realized by pushing the trajectory onto the stable (attracting) manifold of the chosen unstable orbit by means of repeated intelligent perturbations. We have applied this method to a parametrically modulated NMR-laser [2] and proceeded as follows: (i) we extract the unstable periodic orbits from a chaotic time series embedded in a six-dimensional phase space; (ii) we determine the local unstable and stable manifolds at some point (control station) on a given unstable periodic orbit; (iii) we investigate the influence of the control parameter (i.e., the quality factor of the laser system) on the position of the control station in phase space; (iv) then, the real-time control procedure sets in by constructing and analyzing the laser state in the embedded space; the analysis yields the magnitude of the perturbation that changes the control parameter.

Figure 1 shows first results of successful control of the period-one orbit with perturbations of magnitude no larger than four percent of the absolute value of the control parameter. The control has been reproduced many times and tested during long-term operation (more than one hour). It even resisted strong external disturbances and outbursts were observed for no longer than fractions of a second [3].

We have demonstrated the validity of a control method based on weak perturbations which do not alter the nature of the system considered. There are several remarkable features:

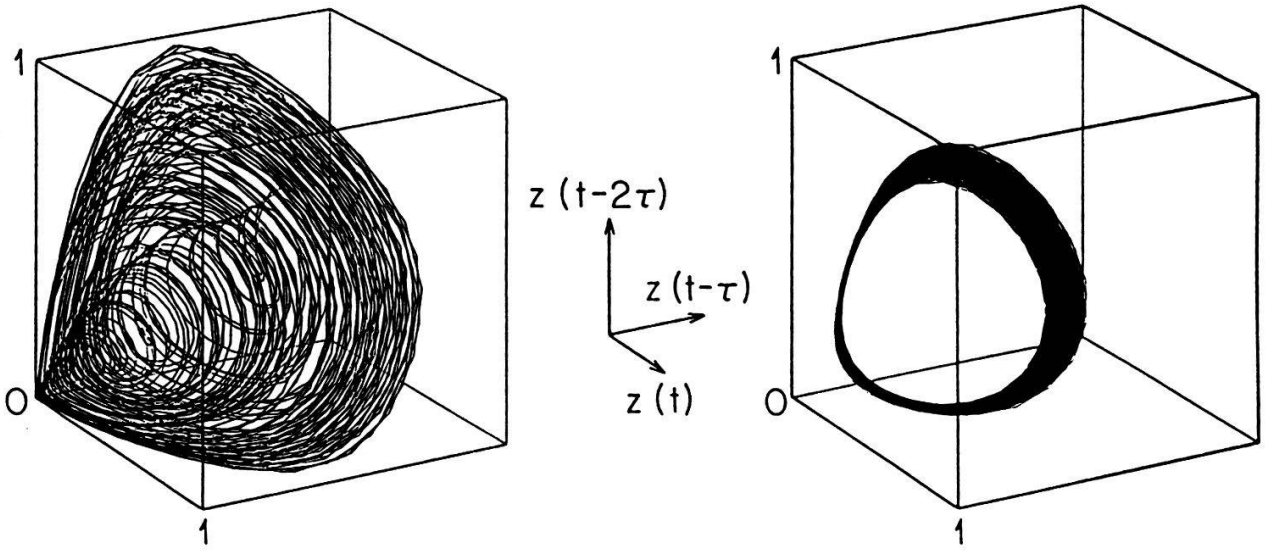

Figure 1: Three-dimensional projection of the originally chaotic (l.h.s.) and of the well-controlled period-one orbit (r.h.s.).

stabilization on any of the observed unstable orbits is possible, no dynamical equations describing the underlying physics are needed, the computational effort is small and opens the door to various real-time applications. Control of many complex systems may be possible in the future.

References

[1] E. Ott, C. Grebogi, J. A. Yorke, Phys. Rev. Lett. **64**, 1196 (1990).

[2] E. Brun, B. Derighetti, D. Meier, R. Holzner, M. Ravani, J. Opt. Soc. Am. B **2**, 156 (1985).

[3] C. Reyl, Diploma Thesis (Zürich, 1992).

SYMBOLIC DYNAMICAL ANALYSIS OF A HETEROCLINIC CRISIS IN THE NMR-LASER

M. Finardi•, R. Badii•, L. Flepp*, J. Parisi*, C. Reyl*, R. Holzner* and E. Brun*
• Paul-Scherrer Institut, LUS, 5232 Villigen PSI
* Physik Institut der Universität, Schönberggasse 9, 8001 Zürich

Abstract: Experimental chaotic signals generated by an externally modulated NMR laser are studied by means of symbolic-dynamical methods. The aim is to construct global models for the dynamics that incorporate the most relevant topological and metric features of the system in a hierarchical order of importance. This approach allows to estimate the critical exponent associated with a crisis in both experiment and model.

Recently, we have shown that a complete and efficient characterization of laser chaos experiments can be provided through a symbolic-dynamical approach [1]. In the present work, we focus on the dynamics near a heteroclinic tangency crisis, i.e., on a sudden change occurring in the chaotic attractor upon variation of a control parameter as a consequence of the collision between the closure of the unstable manifold of some periodic orbit A with the stable manifold of a different orbit B. This phenomenon is accompanied by a characteristic temporal scaling of the trajectories above the critical threshold defining the onset of the crisis [2]. The experimental system consists of a parametrically modulated nuclear-magnetic-resonance (NMR) laser, the dynamics of which can be modelled by a generalization of the Bloch-type differential equations [1,3].

Crises in chaotic attractors manifest themselves through an intermittent bursting between two subsets of phase space. It has been conjectured that the average time $\tau(p)$ between successive burstings (crisis-induced intermittency) obeys the power law $\tau(p) \sim |p - p_c|^{-\gamma}$ in the vicinity of the critical value p_c of the control parameter p. The critical exponent γ has been predicted to lie in the interval $1/2 \leq \gamma \leq 3/2$ (corresponding to the strongly dissipative and conservative limits, respectively) [2]. Since a precise definition of the two domains in phase space is not easy to achieve (in particular, for experimental data so far analyzed just by taking an arbitrary partition in the embedding space), we construct an approximation to a generating partition and identify the two subsets of phase space through different symbolic labels. In this way, we have a clear cut definition of the times spent in the two regions.

Poincaré sections have been obtained for both experimental and model data by sampling the trajectories synchronously with the forcing term and by embedding them in a

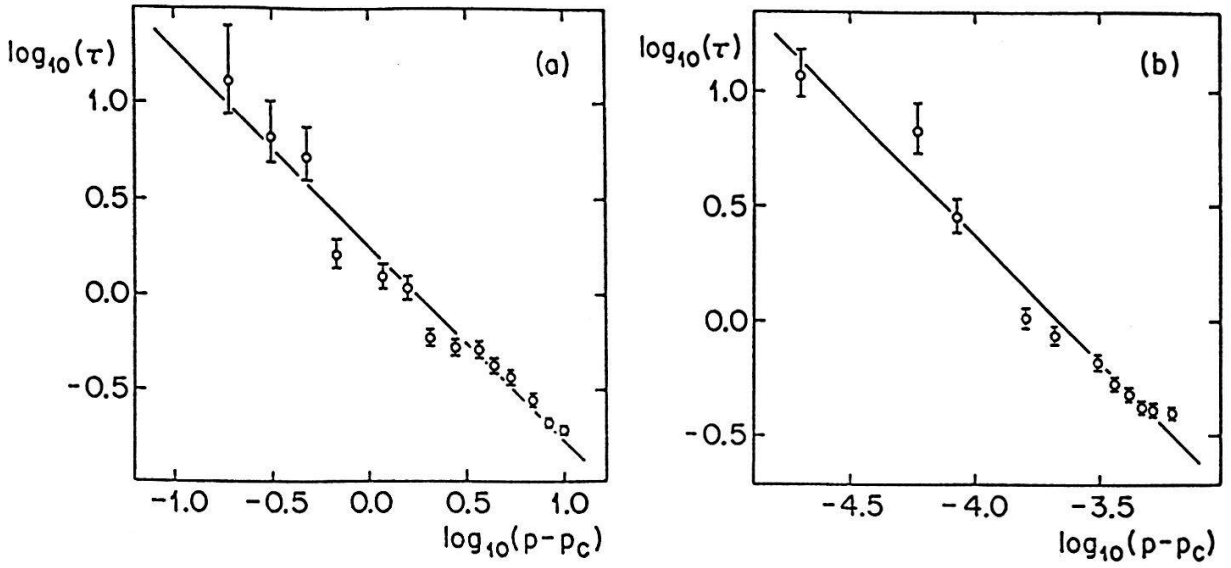

Figure 1: Average time between successive bursts as a function of the distance of the control parameter from the critical value, obtained from experiment (a) and model (b). The critical exponents are determined from the slopes of the straight lines obtained by a least squares fit in a doubly-logarithmic scale.

6- to 16- dimensional space (in fact, the dimension of the attractor is about 2.5). All unstable periodic orbits up to length 9 have been located in the embedding space and a binary generating partition (whose elements are labelled by 0 and 1) has been then approximated by attributing a different symbolic label to each point belonging to an unstable periodic orbit. The only short sequence which is forbidden below crisis ($S = 00$) becomes allowed when the crisis has taken place [1]. Accordingly, we have estimated the characteristic times $\tau(p)$ for 14 different values of p and determined the critical exponent γ from the slope of the corresponding log-log plots (shown in Fig. 1), obtaining $\gamma_e = 1.02 \pm 0.05$ and $\gamma_m = 1.10 \pm 0.05$ for experiment and model, respectively. The values of γ lie in the predicted interval and are consistent with the value 2.5 for the dimension, since the latter is well approximated by $2 + \lambda_1/|\lambda_2|$ and, in the heteroclinic case, $\gamma = 1/2 + \lambda_1/|\lambda_2|$, where λ_i is the i-th Lyapunov exponent of the orbit A [2].

References

[1] L. Flepp, R. Holzner, E. Brun, M. Finardi and R. Badii, Phys.Rev.Lett. **67**, 2244 (1991); M. Finardi, L. Flepp, J. Parisi, R. Holzner, R. Badii and E. Brun, Phys.Rev.Lett. (to be published).

[2] C. Grebogi, E. Ott, F. Romeiras and J.A. Yorke, Phys.Rev. **A36**, 5365 (1987).

[3] E. Brun, B. Derighetti, D. Meier, R. Holzner and M. Ravani, J.Opt.Soc.Am. **B2**, 156 (1985); G. Broggi, B. Derighetti, M. Ravani and R. Badii, Phys.Rev. **A39**, 434 (1989).

A Continuously Tunable CO_2 Laser for Photoacoustic Detection of Trace Gases

P. Repond, T. Marty, and M.W. Sigrist
Institute of Quantum Electronics, ETH Hönggerberg, 8093 Zurich, Switzerland

A UV preionized pulsed high pressure CO_2 laser has been developed. The system operates at a pressure of 11.5bar. With a "near grazing incidence grating" resonator continuous tuning has been obtained in the following ranges: 9R(32) to 9R(8), 9P(10) to 9P(24), 10R(30) to 10R(6) and 10P(10) to 10P(30).

The air quality plays a key role with regard to relevant environmental issues. In order to measure trace amounts of pollutants, mobile detection systems with high sensitivity and high selectivity are desirable. We have developed and since several years successfully operated a detection system using the photoacoustic effect [1]. With a conventional CO_2 laser as radiation source our system achieves a high detection sensitivity of the order of a few parts per billion (ppb). The selectivity of the scheme is also rather good: the simultaneous monitoring of five components in rural air has recently been reported [2]. Yet, the potential selectivity is limited by absorption interferences due to the line tunability of the conventional CO_2 laser. However, continuous tunability can be achieved for laser gas pressures above 10bar due to overlapping of the pressure-broadened laser emission lines [3].

We developed such a high pressure CO_2 laser which is operated at a pressure of 11.5bar. The excitation circuit is a conventional scheme with transverse excitation and UV preionization provided by auxiliary discharges parallel to the electrodes [4]. At high pressures the main problem is to get arc-free discharges. This can be partly overcome by a careful mechanical and electrical design. Arc discharges are seldom observed at low charging voltages but their occurrence increases with increasing voltage. This is the main limiting factor for the operation of our device at pressures above 12bar. The resonator shown in Fig. 1 is a so-called "near grazing incidence grating" resonator [5]. The beam reflected from the back mirror is diffracted by a grating blazed for 10.6μm. The first order beam is incident on a flat mirror which reflects it back into the gain medium, while the zeroth order represents the output. The tuning is performed by rotating the flat mirror. We usually operate the laser at an incidence angle α of 77^0. The overall resonator length is 145 cm. This resonator type offers the advantage of a 6 fold reduction in the bandwidth in comparison with the corresponding Littrow arrangement. This is mainly due to the increased dispersion caused by the double pass of the beam on the grating and by the large incidence angle. The bandwidth is estimated to be about 1GHz. The pulses have a peak power of 0.78MW ± 12% and a duration (FWHM) of 68ns ± 6% whereas the pulse energy varies by ± 8% under the best working conditions. In order to avoid damage to the optics the pulse energy has to be limited to 70mJ by adjusting the charging voltage. Our device provides a large range of continuous tunability as summarized in Table 1. An example of the continuous tunability between two neighbouring lines is presented in Fig. 2 for the 10P branch. The pulse energy is

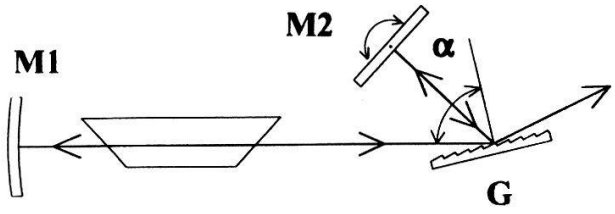

Figure 1. "Near grazing incidence grating" resonator. M1: back reflector with 10m curvature radius; M2: tuning flat mirror; G: 150 lines/mm grating

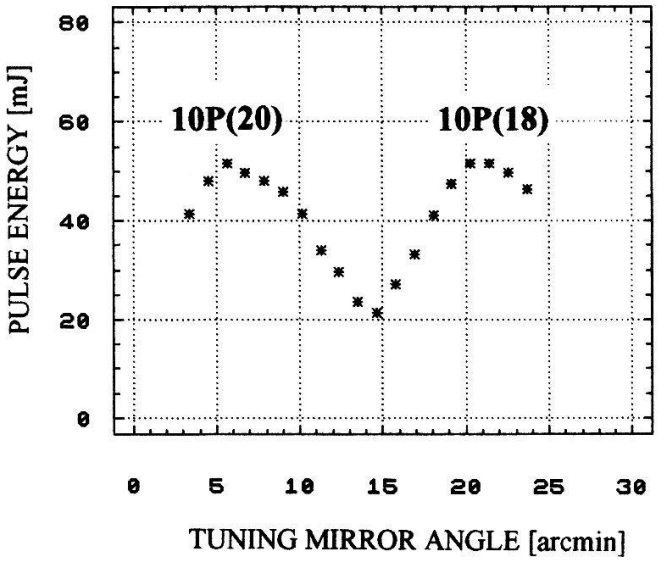

Figure 2. Continuous tunability of the laser between two adjacent lines in the center of the 10P branch

plotted versus the tuning mirror angle which we assume to be proportional to the wavelength since frequency pulling effects are not expected with this resonator type [3,6]. This will be investigated in detail by direct wavelength measurements by means of a high resolution monochromator. As seen in Fig. 2 the modulation in the energy spectrum amounts to 58%. The situation is more favorable in the R branch because of the smaller line spacing resulting in a better line overlap such that the energy spectrum is nearly flat. The measurements of Fig. 2 were performed between two lines in the central part of the branch, where the gain is highest. The charging voltage is thus relatively low. It is therefore possible to compensate the modulation in the energy spectrum by adjusting the charging voltage while tuning the laser. In the subsequent experiments the charging voltage will be computer controlled in order to get the highest attainable pulse energy between the laser lines. This is not possible at the border of the range of continuous tunability because in those cases the charging voltage would have to be increased above a critical value.

9R(32) - 9R(8) 9R(6)	**9P(10) - 9P(24)** 9P(26)/9P(28)	**10R(30) - 10R(6)**	**10P(10) - 10P(30)** 10P(8)/10P(32)
9.210 - 9.342 μm 9.354 μm	**9.473 - 9.586 μm** 9.604/9.261 μm	**10.182 - 10.349 μm**	**10.494 - 10.696 μm** 10.477/10.719 μm

Table 1. Range of continuous tunability (bold). The bottom half indicates the corresponding wavelengths in μm. Additional discrete laser lines are indicated in plain text.

In future studies this new laser will be applied to photoacoustic trace gas monitoring in multicomponent mixtures with enhanced selectivity as well as to time-resolved investigations on molecular energy transfer in the gas phase.

This work is supported by the Swiss National Science Foundation.

References

[1] M.W. Sigrist, in "Progress in Photothermal & Photoacoustic Science & Technology" (ed. A. Mandelis), vol. 1 (Elsevier 1992), ch. 7
[2] A. Thöny, B. Brand, M. Ferro-Luzzi, and M.W. Sigrist, Proc. 7th Int. Top. Meeting on Photoacoustic and Photothermal Phenomena, Springer Ser. Opt. Sci. (1992), in print
[3] T.W. Carman and P.E. Dyer, Opt. Commun. **29**, 218 (1979)
[4] R. Kesselring, Ph D Thesis, ETH Zurich No. 9684 (1992)
[5] D.N. Raouf, Ph D Thesis, University of Hull (1987)
[6] W. Chong-Yi et al., Opt. Commun. **46**, 311 (1983)

Lateral Displacement of a Laser Beam by a precessing magnetic dipole

Tilo Blasberg and Dieter Suter

Institute of Quantum Electronics, ETH Zürich, CH-8093 Zürich

The transverse magnetization-components of an optically pumped atomic vapour induce a longitudinal component in a laser beam propagating through the medium. We show, how the resulting beam displacement is required for the conservation of angular momentum and present an experimental measurement of the beam displacement in Na vapour.

In 1950, Kastler suggested that it should be possible to use polarized light to produce population differences between angular momentum substates of atomic systems [1]. His prediction was based on a detailed analysis of the conservation of angular momentum during absorption of a photon by an atom [2]. While this early theoretical [1] and experimental [3] work dealt exclusively with the modification of the sublevel *populations*, it was shown later, in the 'quantum theory of optical pumping' [4], that also *coherences* between ground state sublevels are affected by the optical pumping process. Physically, these sublevels coherences correspond to angular momentum components perpendicular to the quantization axis. The effect of the pump field on the sublevel coherences is twofold: a damping process reduces their lifetime and a virtual level shift causes a precession of the angular momentum vector. Via the modification of the sublevel dynamics, the light changes therefore the atomic angular momentum. Since the total angular momentum is a conserved quantity, this change of the atomic contribution must be compensated by a change of the angular momentum of the radiation field. A detailed analysis of the situation shows, that this compensation leads to a lateral displacement of the laser beam: a transfer of one quantum of angular momentum in x (y) direction to every photon in the laser beam which propagates along the z-direction leads to a lateral displacement of the laser beam by a distance $\lambda/2\pi$ in -y (x) direction.

As the influence of the light on the dynamics of the atomic angular momentum includes contributions from the damping as well as from the light shift effect, it is also possible to distinguish two contributions to the beam displacement compensating for these effects. The damping of an atomic angular momentum oriented, e.g., along the y axis, should lead to a displacement in the x-direction. Like the damping effect, this beam displacement should have an absorption-like dependence on the detuning of the laser frequency from the optical resonance, independent of the polarization of the light. The light-shift effect, on the other hand, causes a rotation of the angular momentum around the direction of propagation of the laser beam. If the atomic angular momentum is initially oriented along the y-axis, the light-shift effect corresponds to a transfer of angular momentum in x-direction from the radiation field to the atomic medium and the laser beam should be displaced in y-direction. Like the light-shift itself, this displacement should be antisymmetric with respect to the laser detuning and change sign when the polarization of the light changes between opposite circular polarizations. These predictions are in agreement with a semiclassical analysis of the situation [5].

For an experimental verification, we have used the experimental setup of figure 1: the atomic medium, consisting of Na vapour in the presence of 200 mbar of Argon buffer gas, is contained in a glass cell which is heated to a temperature of 124 °C; at this temperature, the absorption at the centre of the resonance line is of the order of 40%. The Na vapour is polarized by irradiation with a pump laser beam in the presence of a transverse magnetic field. The polarization of the pump beam is modulated at a frequency close to the Larmor frequency of the Na ground state [6] to create a

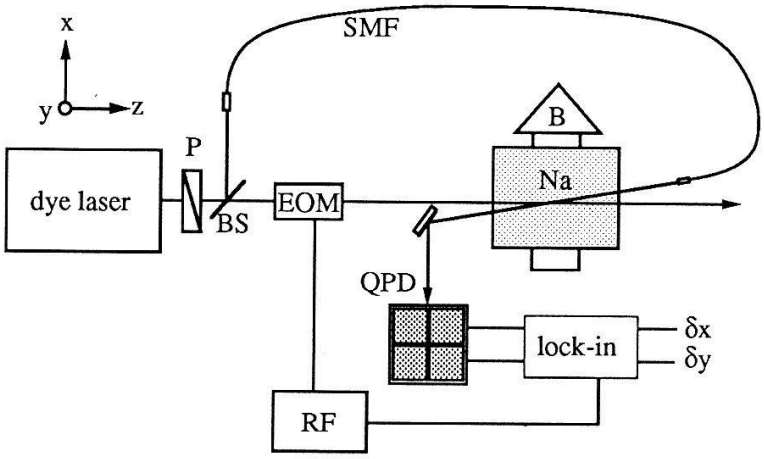

Figure 1: Schematic representation of the experimental setup used for measuring the beam displacement. P = polarizer, BS = beam splitter, EOM = electrooptic modulator, SMF = single-mode fiber, QPD = quadrant photodiode, B = magnetic field, RF = radio frequency synthesizer.

precessing atomic angular momentum. A second laser beam was used to measure the resulting beam displacement. This probe beam was passed through a single mode optical fiber in order to eliminate fluctuations of the beam position originating in the dye laser. For a precise measurement of the beam position, we used a quadrant photodiode with a home-built amplifier and focused the beam into the centre of the four diodes, so that the signal from the detector vanished if the sample was not optically pumped. The intensity of the probe beam was 0.9 mW/cm^2, the intensity of the pump beam 9 mW/cm^2. The two beams overlapped in the sample cell at an angle of ~0.5°.

The detector provides two signals which are proportional to the position of the laser beam. They are passed through a lock-in amplifier in order to extract the contributions from the transverse component of the atomic angular momentum. We measured the amplitude of the components which were out-of-phase with respect to the modulation as a function of the laser frequency in the vicinity of the Na D_1-transition, in order to get the amplitude of the beam displacement. The result is shown in figure 2: the amplitude of the displacement in y-direction, perpendicular to the magnetic field, shown on the left hand side, exhibits the predicted dispersion-like dependence on the laser frequency. The width of the resonance line is determined by the width of the pressure-broadened D_1-transition. Comparison of the upper and lower traces shows that if the polarization of the probe beam is changed between opposite circular polarizations, the displacement changes sign. The corresponding signals for the x-direction (parallel to the magnetic field) are shown on the right hand side. In this case, the displacement amplitude has an absorption-like dependence on the laser frequency detuning and is independent of the probe beam polarization, as expected. These experimental results represent therefore a verification of the predicted displacement of the laser beam.

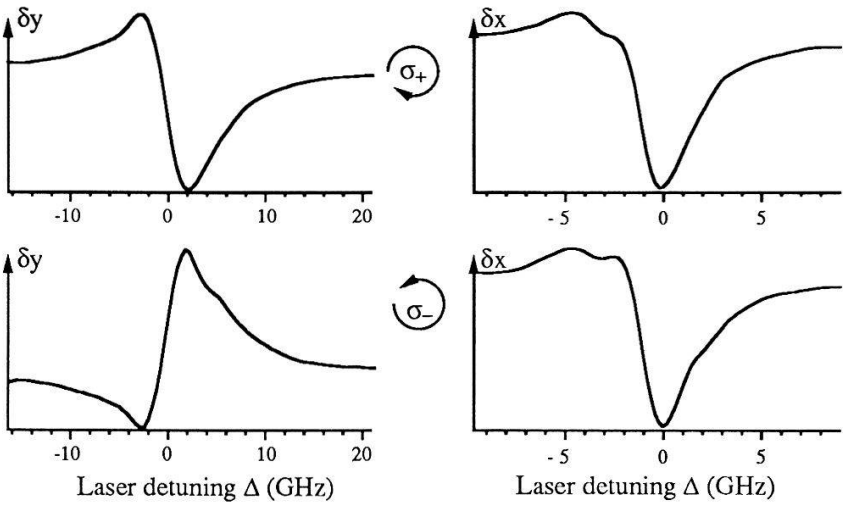

Figure 2: Experimentally measured beam displacement. Shown is the amplitude of the signal at the Larmor frequency, out of phase with respect to the modulation perpendicular (left) and parallel (right) to the magnetic field as a function of the laser frequency. The upper row was measured with a right circularly polarized probe beam, the lower row with a left circular polarization.

We gratefully acknowledge helpful discussions with Jürgen Mlynek, Raoul Schlesser and Antoine Weis. This work was supported by the Schweizerischer Nationalfonds.

References

[1] A. Kastler, J. Phys. 11, 255 (1950).
[2] A. Kastler, Science 158, 214 (1967).
[3] W.B. Hawkins, Phys. Rev. 98, 478 (1955).
[4] J.P. Barrat and C. Cohen-Tannoudji, J. Phys. Rad. 22, 329 (1961); J.P. Barrat and C. Cohen-Tannoudji, J. Phys. Rad. 22, 443 (1961).
[5] D. Suter, Optics Commun. 86, 381 (1991).
[6] H. Klepel and D. Suter, Optics Commun., in print (1992).

Two-dimensional Spectroscopy of 'Forbidden' Raman Transitions by Laser-Induced Coherence Transfer

Dieter Suter and Harald Klepel

Institute of Quantum Electronics, ETH Zürich, CH-8093 Zürich

We demonstrate a new spectroscopic technique that makes it possible to obtain information from 'forbidden' Raman transitions. The technique, which is based on time-resolved two-dimensional spectroscopy, uses laser-induced transfer of sublevel coherence from the Raman-inactive transition to an adjacent transition that can be observed in a Raman-process.

The interaction between atomic systems and radiation is often described in terms of a model that treats the atom as a system of two energy levels interacting with a classical electromagnetic wave [1]. In reality, however, most atomic systems have considerably more complicated level structures. The electronic ground state of atomic sodium, e.g., consists of eight energy levels grouped into two hyperfine multiplets. As is well known, this multiplicity leads to many interesting effects, like optical pumping, that cannot be explained in terms of the simple two-level model. We are interested primarily in the dynamics of such multilevel systems coupled to optical fields. Our experiments involve therefore primarily time-resolved experiments, in contrast to the more conventional steady-state experiments [2].

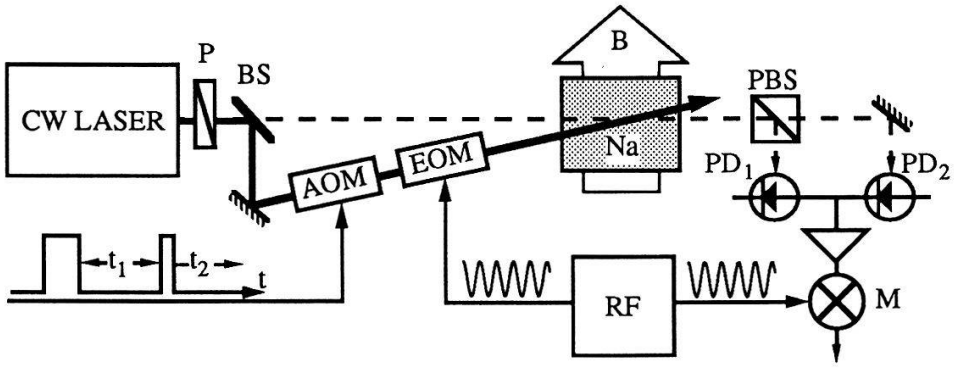

Figure 1: Experimental set-up used for time-resolved pump-probe experiments in atomic multilevel systems. P = polarizer, BS = beam splitter, AOM = acoustooptic modulator, EOM = electrooptic modulator, RF = radio-frequency synthesizer, B = magnetic field, PBS = polarizing beamsplitter, $PD_{1,2}$ = photodiodes, M = mixer.

The experimental setup used for this type of experiment is shown schematically in figure 1. The laser beam, which is derived from a single mode ring dye laser, is split into two parts, a pump beam with an intensity of the order of 100 mW/mm^2, and a probe beam with an intensity of the order of 1 mW/mm^2. The amplitude of the pump beam is controlled with an acoustooptic modulator (AOM) and its polarization can be modulated with an electrooptic modulator (EOM). For an efficient excitation of the atomic medium, which is located in a transverse magnetic field, the polarization of the pump laser beam is modulated between opposite circular polarizations at a frequency close to the Larmor frequency [3]. Pump and probe beam overlap in the sample region, where the metallic sodium is heated to a temperature of ~140°C in the presence of 200 mbar of Ar. The argon is used as a buffer gas to suppress the inhomogeneous Doppler broadening of the optical resonance line and to increase the time the atoms spend inside the laser beam. Behind the sample cell, the probe laser beam is passed into a polarization-selective detector . With the arrangement shown in figure 1 and the polarization of the incident probe beam rotated by 45° with respect to the axis of the polarizing beam splitter, the detector produces a signal proportional to the angular momentum component of the Na atoms parallel to the laser beam.

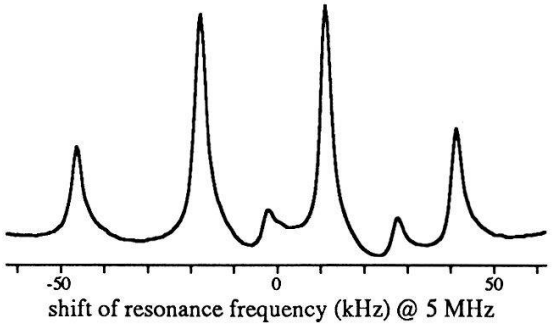

Figure 2: Raman spectrum of the Na ground state.

When a pump laser pulse is applied to the system, it initially induces transient oscillations. After a time of the order of 10 μsec, it settles into a stationary state and after the end of the pulse, the magnetization again starts to precess around the magnetic field; this precession is observed as a free induction decay (FID) signal. The interpretation of the signal can be simplified considerably if it is Fourier transformed.

The resulting spectrum, which is shown in figure 2, contains in general 6 distinct frequency components which can be assigned to the six possible Raman transitions between adjacent sublevels of the Na ground state, i.e. between sublevels whose magnetic quantum numbers m_F differ by $|\Delta m_F| = 1$.

The absence of transitions between sublevels whose magnetic quantum numbers differ by $|\Delta m_F|>1$ can be understood by considering a hypothetical Na atom with vanishing nuclear spin. The electronic ground state consists then of only two sublevels and therefore only a single transition with $|\Delta m_J| = 1$. In the limit of a weak hyperfine interaction, we expect a similar behaviour, i.e. to find only transitions with $|\Delta m_F| = 1$. This and other selection rules can be circumvented by two-dimensional time-resolved spectroscopy. This technique is used extensively in the field of nuclear magnetic resonance (NMR) [4] while applications to optical spectroscopy have not been demonstrated so far. In such an experiment, an initial laser pulse creates order in the form of population differences and coherences within the sublevel multiplets [5]. Since this laser pulse may be arbitrarily strong, multiple Raman transitions can excite coherences also in 'forbidden' transitions, e.g. in transitions with $|\Delta m_F|=2$ [6]. During the subsequent evolution period, these coherences are allowed to precess freely for a time t_1. This free precession period 'labels' the coherences with a phasefactor $\exp(i\,\omega_{ik}\,t_1)$. A second laser pulse causes an exchange of sublevel coherences between the various transitions. As a result, part of the coherence that evolved in transition ik may be transferred, together with the accumulated phase information, into a different transition. If this transition is Raman-active, it is then possible to observe the coherence and thereby measure the phase information associated with the forbidden Raman transition. The resulting signal depends then on the two independent time variables t_1 and t_2, where t_2 represents the time after the second laser pulse. Fourier transformation in both dimensions leads then to a two dimensional spectrum.

An example of a resulting spectrum is shown in figure 3 in contour plot representation. In this case, we suppressed all transitions except the $|\Delta m_F|=2$ transitions after the first pulse by using the different effect that phase shifts of the modulation frequency have on the different types of coherences [6] in order to simplify the spectrum. In the spectrum, we expect therefore along the vertical axis only frequencies corresponding to transitions between next-nearest neighbours. The corresponding frequencies are indicated in the form of a one-dimensional spectrum to the right of the two-dimensional spectrum. After the second pulse, only the 'natural' selection rule $|\Delta m_F|=1$ is active; as a result, the same frequencies as in the one-dimensional spectrum appear along the (horizontal) ω_2-axis. This experimental procedure allows therefore for the first time an observation of all possible transitions between Zeeman substates of the Na ground state.

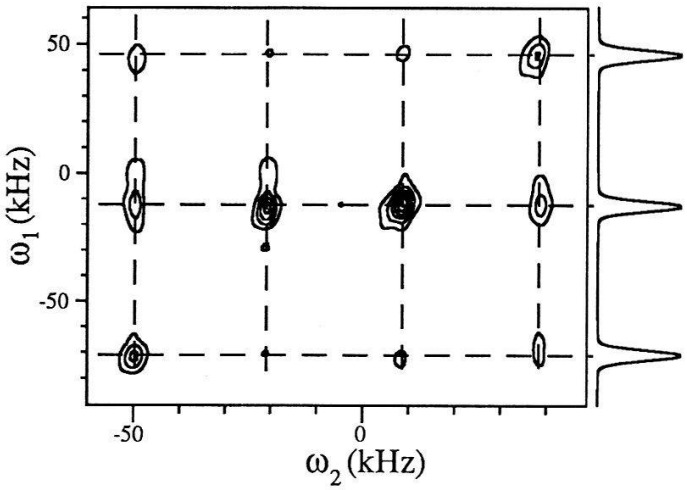

Figure 3: Example of a two dimensional spectrum demonstrating the possibility to use this method for observing 'forbidden' Raman transitions. The vertical axis represents the double quantum ($|\Delta m_F| = 2$) spectrum, while the horizontal axis corresponds to the single quantum spectrum.

We thank Tilo Blasberg for experimental and the Schweizerischer Nationalfonds for financial support.

References

[1] L. Allen and J.H. Eberly, Optical Resonance and Two-Level Atoms, Dover Publications, New York, 1987.
[2] A. Kastler, Science. 158, 214 (1967).
[3] Harald Klepel and Dieter Suter, Optics Commun., in print (1992).
[4] R.R. Ernst, G. Bodenhausen and A. Wokaun, Principles of Nuclear Magnetic Resonance in One and Two Dimensions, Oxford University Press, Oxford (1987).
[5] Dieter Suter, Harald Klepel and Jürgen Mlynek, Phys. Rev. Lett. 67, 2001 (1991).
[6] Dieter Suter, Martin Rosatzin, and Jürgen Mlynek, Phys. Rev. Lett. 67, 34 (1991).

INCOUPLING OF INCOHERENT LIGHT IN AN INFRARED FIBER

O. Oehler, S. Kunz and J. Wieland
Institute for Quantum Electronics,
Swiss Federal Institute of Technology, CH-8093 Zurich, Switzerland.

An elliptical reflector, equipped with a counter-reflecting plane mirror, was used for incoupling of the radiation of a thermal light source into an infrared fiber. The system was applied to CO_2 monitoring.

The availability of optical fibers which are transparent in the mid-infrared (3 μm - 7 μm) enables their application to selective gas detection [1], since most substances show very specific absorptions in this spectral range. The use of lasers in the mid-infrared is often inconvenient because of their high price and their need for cooling to very low temperature. At first sight it seems unreasonable to replace a laser by an incoherent light source, like an infrared LED or even a thermal source, because of their very low radiation density in comparison with the one of lasers. Nevertheless investigations based on a thermal light source are possible [2].

A highly efficient thermal source has been described earlier in connection with photoacoustic measurements [3]. It consists of a kanthal filament S positioned in the focal point of an axially symmetric ellipsoid E (Fig. 1). The elliptical reflector is equipped with a counter-reflecting plane mirror P which is positioned in the central normal plane with respect to the two ellipsoidal focal points. The plane mirror reflects the light back onto the helix-shaped filament S. After multiple passes the source the beam approaches the major axis of the ellipsoid. Finally a collimated light beam is decoupled through an opening O in the center of the plane mirror P. This optical arrangement results in a decrease of the divergence angle of the exiting beam. This way the exit angle of the light source can be matched better to the small numerical aperture of the fiber F_1. The small divergence angle of the exiting light beam also allows it to be effectively filtered by a narrow band interference filter I.

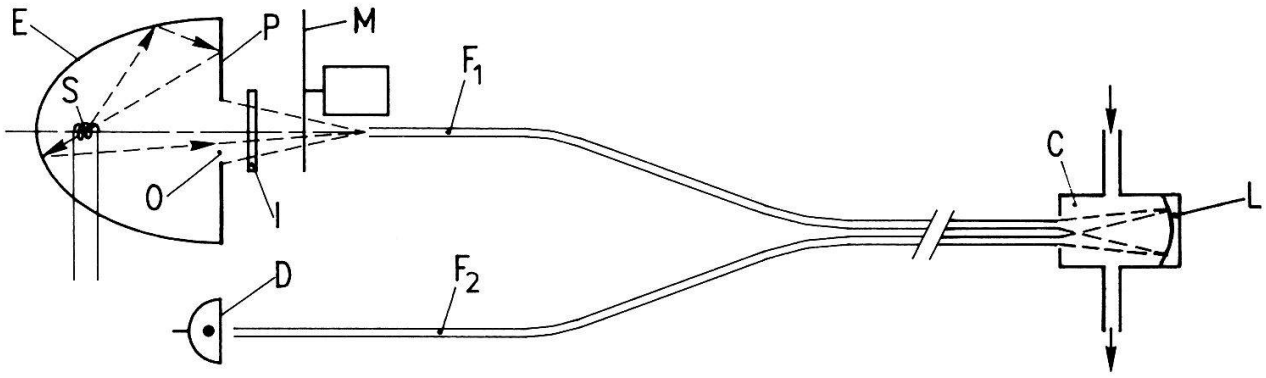

Fig. 1 Optical arrangement for incoupling of thermal radiation into an infrared fiber and remote CO_2 sensing (the denotation is given in the text).

The infrared fluorglass fiber [4] used has a core diameter of 350 μm, an outer diameter of 400 μm and a numerical aperture of 0.2. The incoupling of the light was studied at different apertures O of the plane mirror P and transparencies T of

the filament and was compared with calculations (Table I). For this purpose it was assumed that the ellipsoid of the dimensions A = 40 mm, B/2 = 40 mm has a surface reflectivity of 71 %, the plane mirror a reflectivity of 95 % and the filament an average transparency T = 65 %.

Table I Efficieny of the thermal light source

aperture O		efficiency in % of light incoupling into the fiber		
mm	num. aperture	calc. (T = 65 %)	measured (T = 0)	measured (T = 25 %)
2	0.06	0.23	0.08	0.10
4	0.12	0.64	0.12	0.22
6	0.17	1.44	0.15	0.25
10	0.29	1.82	0.29	0.33
12	0.35	1.53	0.26	0.36
14	0.40	1.24	0.27	0.38
16	0.46	0.98	0.30	0.27
40	1.16	0.19	0.33	0.25

It is obvious from the calculations and the measurements that the counter reflector P gives rise to an increase of the efficiency only at a high transparency of the filament (Table I). For verification further experiments are planed.

The device was applied to measurements of the CO_2 concentration in respiration air. For this purpose the monochromatic and intensity-modulated radiation, which was guided through the fiber F_1, was coupled into a second fiber F_2 via a spherical lense L of focal length 8.3 mm (Fig. 1). The radiation exiting from fiber F_2 was detected (D) thereafter. At a free light pass length of the absorption cuvette C of 33.2 mm, and at a typical CO_2 concentration of exhaled air of 10 %, a reduction of the 4.3 μm infrared radiation by 30 % was measured. Owing to the high sensitivity of the PbSe-detector [5] used ($D^* = 0.6\ 10^{-10}$ at room temperature, 750 Hz) the resolution of the gas concentration measurement was sufficient. At a modulation frequency of 200 Hz (M) with the uncooled detector an output power of 0.5 μW was found at the fiber F_2, corresponding to a signal/noice ratio of 33.5 dB.

This gas detection method allows to avoid any galvanic connections between the gas cuvette and the light source, a well as with the light detector. The energy transfer to the absorption cuvette is established via the glass fibers only.

Besides medical applications the possible use in explosion-protected gas detection devices is obvious.

We would like to thank Dr. J. Brunner of Hamiltion Bonaduz AG, CH-7402 Bonaduz for helpful discussions and partial support of this project.

References

[1] D. Pruss, P. Dreyer and F. Koch, SPIE, **799**, New Material for Optical Waveguides, 117 (1987).
[2] M. Saito, M. Takizawa and M. Miyagi, J. Lightwave Technology. **6**, 233 (1988).
[3] D. Sourlier and O. Oehler, J. de Phys.-coll., suppl. No 10, **44**, C6, 587 (1983).
[4] Le Verre Fluorid, Z.I. du champ martin, F-357770 Vern-sur-Siech, France.
[5] Infrared Industries Inc., 12151 Research Parkway, Orlando, Fl 32826, USA.

Optimization of the Front Contact of Solarcells

W. Rehwald

Paul Scherrer Institut Zürich, Badenerstr. 569,
8048 Zürich (Switzerland)

The front geometry of a solar cell is a compromise between a value as low as possible for the series resistance, resulting in a high fillfactor, and minimum shadowing losses by the metal grid. An optimization procedure is described, and results are given for two common forms of front contacts.

In general, solar cells carry a front contact, structured in the form of a comb or a tree. This structure should have a low resistance in order to avoid ohmic losses and keep the fillfactor high. On the other hand, it should also occupy an area as small as possible to minimize shadowing losses. The optimum geometry is a compromise between these two postulates.

The charge carriers, produced by the absorption of light, are separated by the electric field within the p-n-junction. Since the emitter is generally very thin compared to the distance of the finger contacts,- typical values are 1 micrometer compared to 1 mm -, the current in the emitter flows practically parallel to the surface. It is picked up by the fingers and collected in a busbar, either at its ends in the comb, or in its centre in the tree structure. The current increases from the centre of the emitter spaces between the fingers linearly towards the fingers. Similarly it increases along the fingers towards the busbar and in the busbar, when the contact pad is approached. The ohmic losses in the various parts are calculated by integration, summed up and divided by the square of the cell current to yield the series resistance R_S [1]. In laboratory cells, which are discussed here exclusively, the contact structure is etched into the passivating oxide in a microlithographic process; then titanium and palladium are evaporated to yield a stable ohmic contact; afterwords the metallization is reinforced by electrolytic deposition of silver.

Denoting the size of the square cell by a, the finger width by s, and the busbar width by b, simple formulae can be obtained in the limit of a large number N of fingers and sufficiently narrow fingers, $N\,s << a$, for the comb

$$R_S = r_e / (12\,N^2) + r_m\,a / (3\,N\,s) + r_m\,a / (3\,b)$$

and for the tree

$$R_S = r_e / (12\,N^2) + r_m\,a / (12\,N\,s) + r_m\,a / (3\,b).$$

The sheet resistances r_e and r_m of the emitter and the metallized contact areas are given by the fabrication process. The series resistance deteriorates the fillfactor by a factor <1, containing in addition the short-circuit current I_k and the open-circuit voltage U_l:

$$FF = FF_0\,(1 - R_S I_k / U_l).$$

The shadowing efficiency is determined by the ratio of the contact area to the total cell area. The target function to be optimized contains both the R_S-dependent factor in the fillfactor and the shadowing efficiency. The number of fingers N, their width s and the width b of the busbar are considered as variable parameters. The optimization is done by the Simplex Algorithm [2]. First runs yielded fingers too narrow be handled in the fabrication process. Therefore we kept s constant at a value of 25 micrometers and varied only N and b as a function of the cell size a.

The results are shown in Figs. 1 and 2. Both, the busbar width b and the optimum number of fingers increase with a, stronger than linearly, but in a different manner for the comb and the tree. For the comb

structure the optimum N rises more strongly, the optimum b less strongly then in the tree structure. Fig. 3 shows the resulting series resistance and shadowing efficiency for both structures as a function of the cell length a. A similar complementary behaviour is found here. Comparing the target function for both structures, there is a small advantage in the comb structure, but the differences are minimal.

Further improvements can be achieved if the widths of both the fingers and the busbar are varied according to the current load. Another method is to change the aspect ratio of the finger metallization in a way resulting in narrow but thick stripes. This step requires producing deep trenches that are filled with metal.

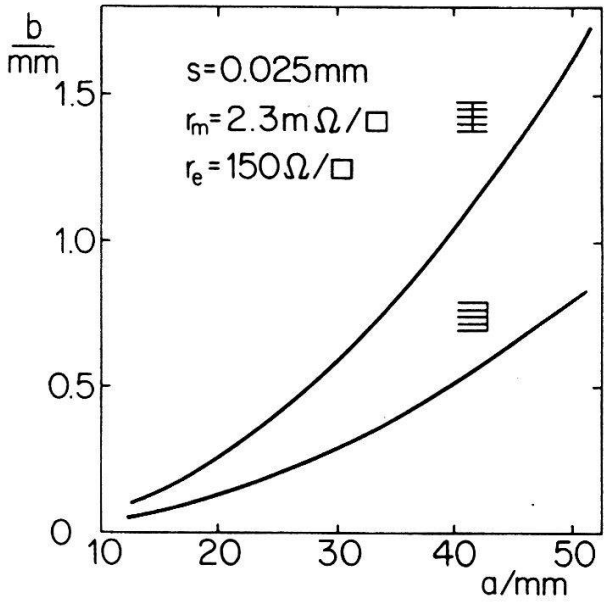

Fig. 1: Optimum busbar width b as a function of cell size

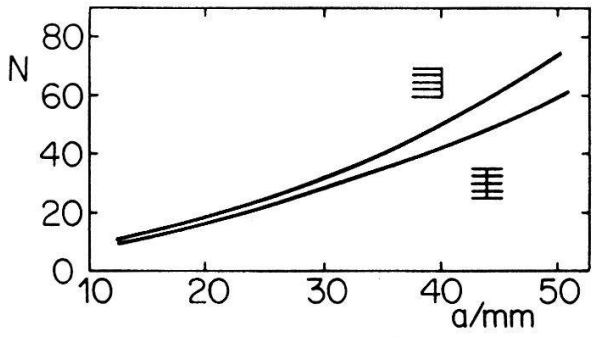

Fig. 2: Optimum number N of fingers as a function of cell size

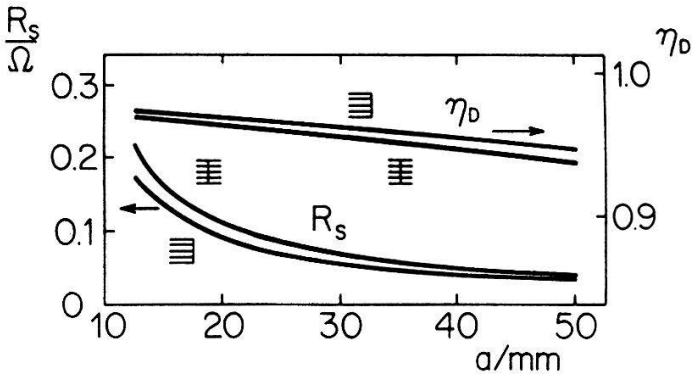

Fig. 3: Optimum series resistance and shadowing efficiency as a function of cell size

References

[1] R. J. van Overstraeten, R. P. Mertens: Physics, Technology and Use of Photovoltaics; Ad. Hilger, Bristol, 1986, p. 33-36.

[2] M. S. Caceci, W. P. Cacheris, Byte **9**, 340 (1984)

Possible mechanisms and effects of strong electron-phonon coupling in high T_c oxides.

T. Jarlborg

DPMC, Université de Genève, CH-1211 Genève 4, Switzerland.

The two-dimensional structures in combination with large ionicity lead to large electron phonon coupling λ in high-T_c oxides. The low z-dispersion of the bands weakens the screening of high frequency q_z-phonons, and leads to a further enhancement of λ. Results from first-principle LMTO electronic structure calculations are used in simple models of the coupling and its consequencies. Here, possible effects on resistivity and Hall effect are outlined.

Electron-phonon coupling has been calculated from electronic bandstructures and leads to the conclusion that it has unusual long-range origins in high-T_c oxides [1]. Large ionicity in combination with the 2-dimensional structure of high-T_c oxides makes the Madelung shifts of the potentials large for atomic movements in the z-direction. This leads to a $\Delta\ell = 0$ contribution to the electron-phonon coupling which is larger than the usual dipole contribution [2]. Movements due to high frequency oxygen modes or due to heavy ions (Ba etc) give the largest effects [3]. Superconductivity in the range 30-40 K can be explained by this effect but for higher T_c one needs additional effects.

The fact that also the electronic structure is 2-dimensional is reflected in the very low Fermi velocities v_f in the z-direction. For the cylindrical 'barrel' bands v_f is comparable to the velocity of atomic vibrations in the z-direction. This situation leads to non metallic screening of high frequency fields with q perpendicular to the planes, which in turn implies a further enhancement of λ. Simple real space arguments suggest that a static electronic structure is instable against the formation of charge density fluctuations [4]. The reason is that states near E_f can diminish their energy by being in phase with atomic vibrations in order to coincide with the favourable Madelung shifts. Local electronic fluctuations around single sites with large Madelung shifts lead to smearing effects, while for favorable phonon group velocity, extended band states can gain energy. Internal Coulomb repulsion opposes the effect, but for small charge fluctuations it is possible to gain energy without cancellation of the Madelung shifts. The mechanism is most effective for the low dispersive 'barrel' bands, and the energy shifts create corrugations at some q_z on the cylindrical Fermi surface.

A model of a hole band as in the ab-initio calculation is obtained by $E_k = -a(k_x^2 + k_y^2) + bk_z$, where a is about 0.8 Ryd for $k_x, k_y \leq 0.5\ (a.u.)^{-1}$ and b is small (about 0.01 Ryd for $k_z \leq 0.2\ (a.u.)^{-1}$). E_f is fixed at -0.15 Ryd. The effect from the fluctuation is achieved by subtracting from E_k, $\Delta/(1 + (E - E_f)^2/\Delta^2)\Theta(E_f - E)$ for k_z smaller than about 1/10 of k_z^{max}. From this model it is possible to evaluate resistivity and Hall coefficient. The former is expected to decrease at low T since the k_z-derivatives increase for corrugated

bands, but the effect on the scattering time τ makes the calculation uncertain. In the Hall coefficients, the dependence on τ is cancelled, and band features have a direct influence on calculated values [1]. Although the band model is temperature independent there are T-variations via the Fermi-Dirac function so that mostly states far from E_f dominate the total contribution for large T. Band broadening is not explicitly included in the model, but in practise smearing enters via the limited resolution of the k-point mesh. The result for the Hall coefficient R_{xyz} with $\Delta = 1$ mRyd is shown in the figure. The parameter is chosen quite arbitrarily with the objective to produce a partial 'gap' comparable to the maximum z-dispersion at E_f, with the effect rapidly disappearing below E_f. Experiments show the similar type of upturn for low T [5].

It is clear that this model only give qualitative trends. But it shows that the type of band distortions that are expected from the strong electron phonon coupling and the fluctating charge density wave, are able to produce temperature anomalies in many normal state properties. The specific mechanism cannot be separated from other mechanisms that give similar band distortions. Other explanations, not relating to bands, are coming from non Fermi-liquid theories [6].

References

[1] W Pickett Rev of Mod Phys 61 433 (1989); R E Cohen W E Pickett and H Krakauer Phys Rev Lett 65 2575 (1990)

[2] T Jarlborg Helv Phys Acta 61 421 (1988); Sol State Commun 67 297 (1988); Sol State Commun 71 669 (1989)

[3] T Jarlborg Physica B172 245 (1991)

[4] T Jarlborg Phys Lett A (to be published) (1992)

[5] M Affronte et al Phys Rev B43 11484 (1991); M Affronte PhD thesis 971 EPFL (1991)

[6] T R Chien, Z Z Wang and N P Ong Phys Rev Lett 67 2088 (1991); P W Anderson Phys Rev Lett 67 2092 (1991)

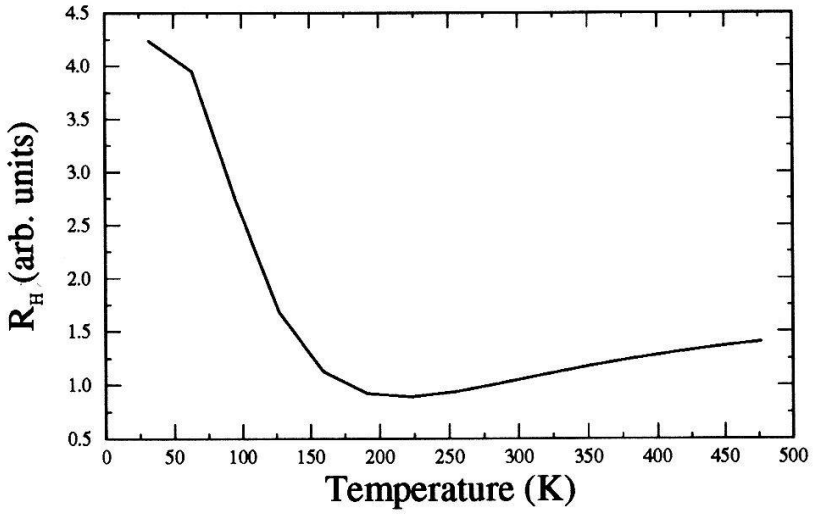

Calculation of positron annihilation in High T_c copper oxides.

B. Barbiellini, T. Jarlborg, M. Gauthier and A. Shukla

DPMC, Université de Genève, CH-1211 Genève 4, Switzerland.

LMTO calculations have been done in order to obtain electronic and positronic states in YBaCuO compounds. The annihilation rates have been calculated including the enhancement effects. Folded momentum density spectra are calculated and used for prediction of Fermi surface signals. The influence of lattice defects on the spectra is studied by the comparison between experimental and calculated positron lifetimes.

The calculations show that positrons in YBaCuO compounds are good probes of Cu-O chain related electronic states [1, 2]. Therefore clear Fermi Surface (FS) signals related to these states should be seen. Experimentally these FS structures have escaped observation for long time in $YBa_2Cu_3O_{7-\delta}$ (1:2:3) [3]. A possible explanation of the difficulty to observe a clear Fermi surface (FS) signal in 1:2:3 is that in less oxygenated samples the Cu-O chains give smaller signals than in an ideal pure sample ($\delta = 0$). The presence of oxygen defects would explain the observed complex temperature dependences of the lifetime and that calculated lifetimes are smaller than the experimental ones [7].

The $YBa_2Cu_4O_8$ (1:2:4) superconductor may be a better candidate since the oxygen content is stable [4] and it forms twin-free crystals. Therefore, we have studied the 1:2:4 structure in order to determine the amplitudes of the positron annihilation signal.

Self-consistent calculations of the electronic structure have been performed using the LMTO (Linear Muffin Tin Orbitals) method. The positron potential is taken as the inverse of the electron Coulomb potential. The positron is assumed to be thermalized when annihilating and its wave function is then calculated only at $k = 0$. Then the positron wave function calculation is carried out using the LMTO method. The annihilation rates are calculated using the electronic and positronic states and an enhancement factor proposed by Jarlborg and Singh which take in account the screening around the positron inpurity [5]. In 1:2:4 as in 1:2:3, we find that the positron in mostly distributed in the layers containing the Cu-O chains. The calculated lifetimes in (ps) are 156 for 1:2:3 (if $\delta = 0$) and 183 for 1:2:4. If $N(t) = N(0)\sum_i I_i \exp(-\mu_i t)$ is the number of positrons remaining at time t, then the experimental lifetime known as bulk lifetime is calculated as $1/\tau = \sum_i I_i \mu_i$. The experimental values using Posfit [7] for 1:2:3 and 1:2:4 are respectively 170 ± 5 and 198 ± 5. These results were confirmed by the MaxEnt method [6]. The details of the experimental setup can be found in reference [7]. The different τ in the two compounds can be understood by the fact that more open space exists in the 1:2:4 (chain layers). In 1:2:3, when δ increases, the lifetime increases reaching a calculated value of 200 (ps) and an experimental one of 215 ± 5 (ps) for $\delta = 1$. This is explained by the positron tendency to localize in the oxygen-deficient zones [8].

The 1:2:4 FS is composed of 4 sheets: 2 *barrels* for the two-dimensional Cu-O planes and 2 *ridges* for the one-dimensional Cu-O chains. The 1:2:3 FS is also composed by 4 sheets: 2 barrels, only one ridge and a small area hole pocket around the S point. In Figure 1, we show the LCW Momentum Density in the folded k-space for the 1:2:4 without (a) and with (b) positron wavefunction and enhancement effects (the signal is convoluted with experimental resolution ~ 0.5 (mrad) in 1(b)). Figure 1(a) gives essentially the electronic occupation as a function of the Bloch wave vector. The non-homogeneity of the positron ditribution destroys the Cu-O plane FS modulation in figure 1(b). The Cu-O ridge signal is larger almost by a factor 2 with respect to 1:2:3 and should allow for an experimental detection.

We are grateful to Dr. L. Hoffmann, P. Lerch, Dr. A.A. Manuel, Professor M. Peter, Dr. W. Sadowski and Dr. E. Walker for numerous discussions.

References

[1] T. Jarlborg *et al.*, J. Phys. and Chem. of Solids **52**, 1515 (1991).

[2] B. Barbiellini *et al.*, *Proc. 9th Int. Conf. on Positron Annihilation* (Mater. Sci. Forum at press).

[3] M. Peter *et al.*, Europhys. Lett. **18**, 313 (1992).

[4] J. Karpinski *et al.*, Nature **336**, 660 (1988).

[5] T. Jarlborg and A.K. Singh, Phys. Rev. B **36**, 4660 (1987).

[6] A. Shukla and M. Peter, *Proc. 9th Int. Conf. on Positron Annihilation* (Mater. Sci. Forum at press).

[7] M. Gauthier, Archs Sci. Genève **44**, 341 (1991).

[8] R. M. Nieminen, J. Phys. and Chem. of Solids **52**, 1577 (1991).

Figure 1: LCW Momentum Density (a) without and (b) with positron effects.

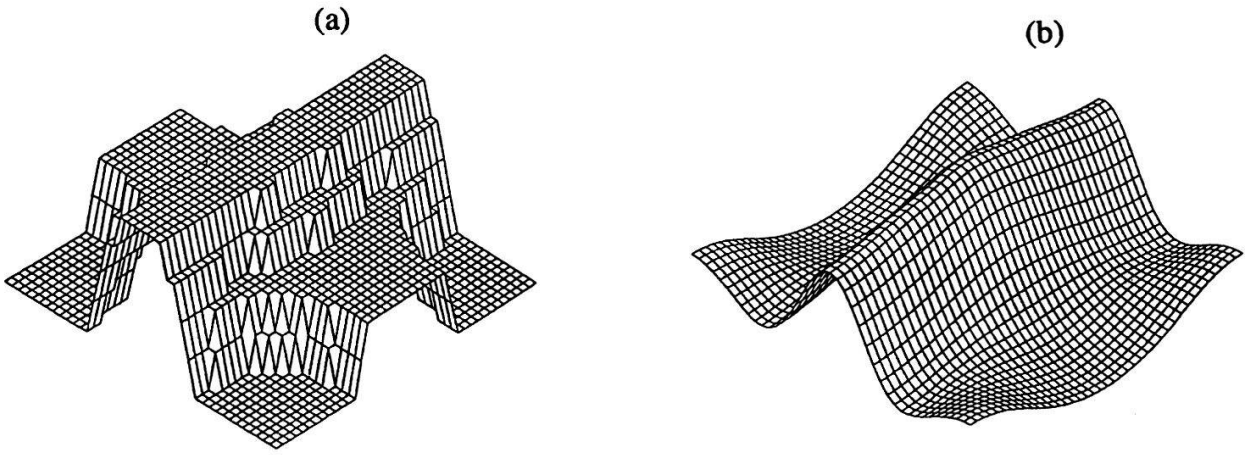

Post–Hartree–Fock Calculations of Hyperfine Properties for Anomalous Muonium in Diamond

N. Paschedag, Dj. M. Maric and P. F. Meier
Physik–Institut der Universität Zürich-Irchel, 8057 Zürich

Accurate prediction of hyperfine coupling constants is still a difficult task for *ab initio* calculations and is highly dependent on the method used. In particular, the values for the contact term obtained from various Hartree–Fock level calculations are unsatisfactory for most atoms and molecules. Using the configuration interaction method applied to C_8H_{18} clusters the spin densities and hyperfine constants have been calculated for anomalous muonium and ^{13}C nuclei.

Detailed information about hydrogen in semiconductors has been provided by various muon spin rotation (μSR) experiments. Theoretically, the electronic structure of the anomalous muonium state (Mu*) has recently been thoroughly investigated by Vogel [1] and Maric [2] using cluster calculations at the Hartree–Fock level. The muon (hydrogen) is localized in the middle of the bond between two neighboring host atoms which are symmetrically displaced from their ideal lattice positions. Using clusters of eight host atoms ($(XH_3)_3X$–Mu–$X(XH_3)_3$), where X = C or Si, geometry optimisation led to a relaxation of the X–Mu–X bonds of 42.3 % for C and 34 % for Si, all other atoms being assigned to idealized lattice positions.

The calculation of hyperfine properties, however, is a more difficult task, since they depend sensitively on the detailed distribution of unpaired electrons. The contact term ν_c is zero in restricted Hartree–Fock (ROHF) calculations due to a node of the orbital of the unpaired electron at the bond–centered impurity but is largely overestimated by unrestricted Hartree–Fock (UHF) methods.

In this report first results from calculations using the configuration interaction (CI) method for diamond are presented. This method can accurately take into account correlation effects while maintaining the correct spin eigenstate, a problem for the UHF method.

The CI expansion was obtained from the orbitals of an ROHF–calculation and included all single and double excitations from the groundstate. To solve problems imposed by the necessary truncation of the huge number of generated configurations, application of perturbation theory was essential in selecting the subset of configurations with the largest energy contribution. The quantum chemistry package MELDFX [3] allowed the use of Rayleigh-Schrödinger B_k theory [4,5] for this selection and correction of effects originating from neglecting less important configurations, such as the disturbed ratio among individual coefficients. The final electronic properties were then calculated from the resulting CI wave function.

The CI results for the optimized symmetric displacement of the two neighbouring carbon atoms differ only slightly from the HF values, the relaxation being 41.3 %.

In Figure 1 the convergences of the calculations for the contact terms for the muon and the neighboring C nuclei are shown as a function of the number of selected configurations.

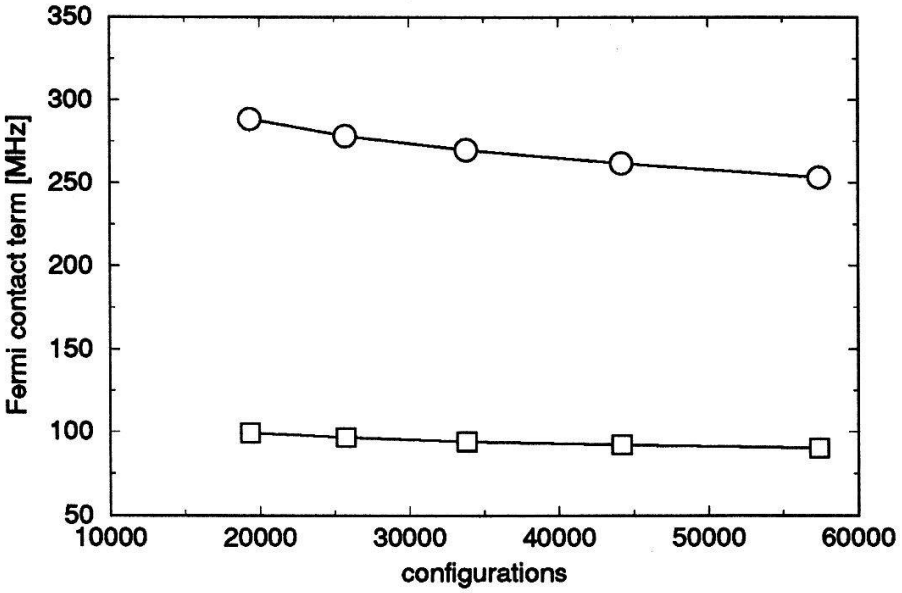

Figure 1: Absolute values of the contact terms for Mu* (o) and ^{13}C (□) as a function of the number of configurations. A total of $2 \cdot 10^4$ ($6 \cdot 10^4$) configurations corresponds to an effective selection threshold of $1.3 \cdot 10^{-5}$ ($0.5 \cdot 10^{-5}$) Hartrees.

$C_8H_{18}Mu$	basis set	ν_c (Mu)	ν_{dip} (Mu)	ν_c (C)	ν_{dip} (C)
UHF	dzp	-851	320	222	57
CI	dz	-291	261	96	53
CI	dzp	-253	287	90	55
experiment		-206	187	-	-

Table 1: Hyperfine parameters (MHz) for anomalous muonium in diamond calculated at various levels of theory.

In Table 1 the hyperfine frequencies ν_c (contact term) and ν_{dip} (dipolar term) calculated at the HF level and with CI, using double zeta (dz) and dz+polarisation (dzp) basis sets, are presented. In these values the influence of the spread of the muon wave function is not yet taken into account.

The experimental muon hyperfine frequencies are taken from ref. [6]. New μSR–experiments to determine the carbon hyperfine parameters using ^{13}C enriched diamonds are in progress.

References

[1] S.Vogel, PhD Thesis, University of Zürich (1991).
[2] Dj.M.Maric, PhD Thesis, University of Zürich (1991).
[3] MELDFX, Molecular Science Research Group, Richland, Washington 99352, 1991.
[4] I.Shavitt, The method of configuration interaction, in: Methods of electronic structure theory, ed. H.F.Schaefer III (Plenum Press, New York 1977).
[5] B.Engels, Chem.Phys.Lett. **179**, 398 (1990).
[6] E. Holzschuh, W. Kündig, P.F. Meier, B.D. Patterson, J.P.F. Sellschop, M.C. Stemmet and H. Appel, Phys. Rev. A **25**, 1272 (1982).

Passivation of Acceptors in Silicon by Hydrogen or Muonium: Ab–Initio Calculations of Electric Field Gradients

Dj. M. Maric and P. F. Meier
Physik–Institut der Universität Zürich–Irchel, 8057 Zürich

Hydrogen passivation of acceptors and donors in semiconductors has recently attracted great interest. We report on *ab initio* Hartree–Fock cluster calculations for the hydrogen or muonium passivation of shallow acceptors (B, Al and Ga) in silicon. The equilibrium microscopic structures are obtained and the electric field gradients at the quadrupolar nuclei are estimated from the calculated wavefunctions. The quadrupole resonance frequencies are thereby predicted. Detection via cross–relaxation techniques is proposed, notably muon level crossing resonance (μLCR), and illustrated by spin dynamics simulation of the time dependence of the muon polarization functions.

The passivation of both donor and acceptor impurities in semiconductors by hydrogen or muonium (Mu=μ^+e^-) has a profound effect on the electrical properties of semiconductors. The complexes have been detected experimentally by infrared (IR) and Raman spectroscopy and by channeling studies [1]. Generally, three different sites of the hydrogen relative to the impurity are discussed, namely bond-centred (BC), antibonding to the defect or antibonding to an adjacent host atom.

Employing *ab–initio* Hartree–Fock calculations [2] on clusters of the type Si_7XMuH_{18} with X = B, Al or Ga, we have investigated the microscopic structure of these complexes. Optimization within C_{3v} symmetry of the positions of the central Si, X and Mu were carried out, keeping all other atoms at their idealized lattice position. Polarized double–zeta basis sets were used for the valence orbitals, and *ab–initio* pseudopotentials for the core orbitals. All–electron wavefunctions calculated at these equilibrium configurations were used to obtain the electric field gradients at the quadrupolar nuclei.

Table 1 shows the calculated equilibrium structures of all three acceptor passivation pairs in silicon, together with the resulting electric field gradients at the acceptor nuclei.

Acceptor	d (Å)	$V_{xx} = V_{yy}$ (au)	V_{zz} (au)
B	1.499	0.188	-0.376
Al	1.618	0.505	-1.010
Ga	1.617	1.225	-2.450

Table 1: Calculated equilibrium structures of the acceptor passivation complexes in silicon. The hydrogen–acceptor distance d and the elements of the electric field gradient tensor V_{xx}, V_{yy} and V_{zz} (in principal axes) experienced by the acceptor nuclei (in atomic units; $1\,\text{au} = 0.972\,\text{V/cm}^2$) are shown. The results are presented for the lowest energy configurations (BC), where H is placed at the bond–minimum site.

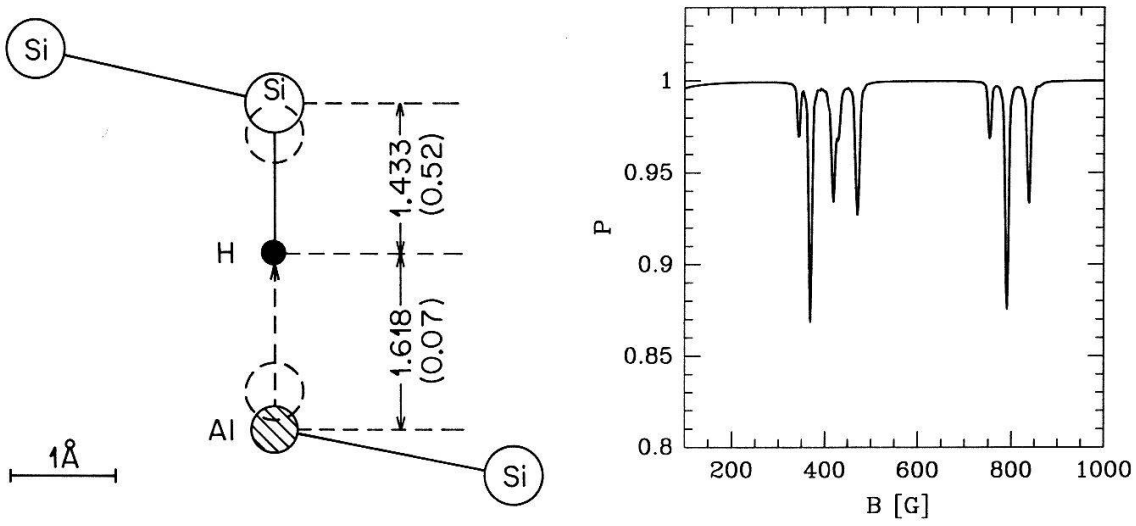

Figure 1: Hydrogen or muonium passivated Al (spin 5/2) in silicon. Left is the calculated geometry of the lowest energy configuration of the (Al,H) complex. The distances are given in Å, and the dashed circles indicate the location of the undisturbed substitutional sites. The bond indices are given in parenthesis. Right is the simulated integrated polarization curve P as a function of the external magnetic field for this passivation complex.

Using the calculated microscopic structures of the passivation complexes and the obtained electric field gradients at the quadrupolar nuclei, the quadrupole resonance frequencies are predicted. These frequencies are expected to provide the spectroscopic signatures of the various configurations. This opens the possibility of studying these complexes by Muon Level Crossing Resonance (μLCR) spectroscopy, as the expected muon depolarization spectra are here numerically simulated.

The calculations for the bond–centered configuration of the (B,H) pair in Si have already been published [3]. These calculations have now been extended for deeper acceptors Al and Ga. The predictions for the positions and amplitudes of the resonances in the case of the hydrogen or muonium passivated Al in silicon are given in Figure 1 (right) for the bond–centre configuration of the complex (shown left). In this presentation, residual muon polarization is displayed, integrated over a time window which is delayed relative to the muon implantation so that the exchange of polarization has had an appropriate time to develop.

New μLCR experiments to study the microscopic structure of the shallow acceptors passivated by hydrogen (Mu) in silicon are in progress.

References

[1] *Hydrogen in Semiconductors*,
Ed. J.I. Pankove and N.M. Johnson, (Academic Press, New York, 1990).
[2] Dj.M. Maric, Ph.D. Thesis, University of Zürich (1991).
[3] Dj.M. Maric, S.Vogel, P.F.Meier, S.F.J. Cox, E.A. Davis and J.W. Schneider,
J. Phys.: Condens. Matter **3**, 9675 (1991).

Martensitic transformation in Ni-Al alloys by NMR

S.Rubini*, C.Dimitropoulos*, R.Gotthardt** and F.Borsa***

*IPE, ** IGA, Ecole Polytechnique Fédérale de Lausanne, CH-1015 Lausanne Switzerland
*** Department of Physics, Iowa State University, Ames, IA50011
and Dipartimento di Fisica "A. Volta", Università di Pavia, I-27100 Pavia Italy

The process of nucleation and growth of the martensite in the parent phase during the cooling of two NiAl alloys of different composition and particles size has been investigated by the evolution of the NMR ^{27}Al spectra. The results are presented and compared with the previous investigation in a CuZnAl alloy.

Introduction

Ni rich NiAl alloys (60-65% Ni), undergo, by lowering the temperature, a martensitic phase transformation (MPT) from the metastable cubic β phase (austenite), to a monoclinic close packed structure (martensite). The transformation is thermoelastic and proceeds by nucleation and growth of the martensite in the parent β-phase.

Nuclear Magnetic Resonance (NMR) technique, providing local microscopic informations about the changes arising in the crystal at the transformation, has already proved his potential in the study of the MPT in CuZnAl alloys[1].

In this work we study the evolution of the ^{27}Al NMR spectra in order to investigate the process of nucleation and growth of the martensite by cooling, in two NiAl alloys (62%Ni and 63%Ni) and as a function of the particles sizes: large particles (1mm) and powder (less than 150 μm). We will concentrate here to the features of the transformation. The details of the experimental conditions are described elsewhere[2].

Results and discussion

^{27}Al absorption spectrum is composed in all samples and at all temperature by a narrow unperturbed central line, superimposed to a residual broad distribution of quadrupole satellites. The NMR frequency of the line changes during the transformation.

In Fig. 1 (a) we report the values of the ^{27}Al Knight shift vs temperature and in Fig. 1 (b) the linewidth, as obtained from the fit of the central line by a gaussian lineshape, for

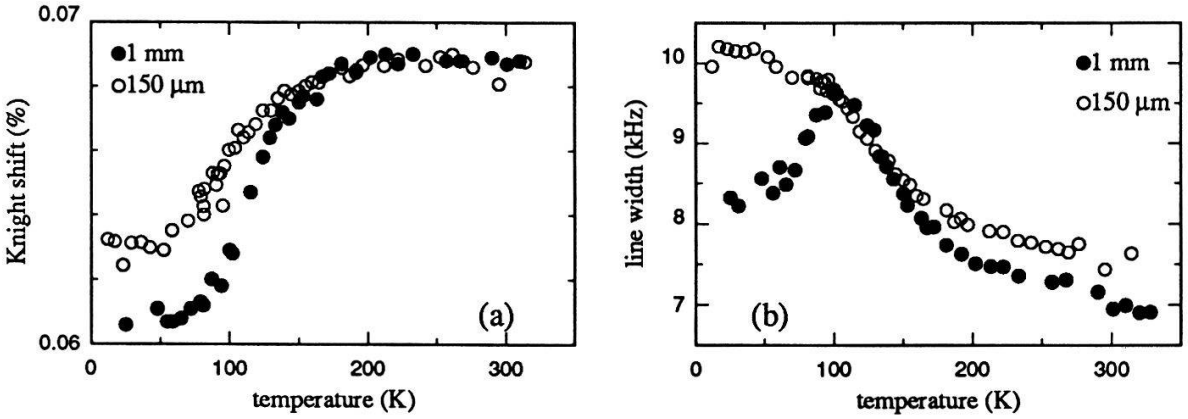

Figure 1

the 62% Ni alloys. Similar results have been obtained on the 63% Ni alloys, around the transition temperature at 300K. Let us consider the large particles sample. A broadening of the ^{27}Al line is clearly visible at the transformation, superimposed to a temperature dependent background of magnetic origin. As the frequency of the signal is different in the two phases, this broadening should be interpreted as due to the superposition of signals arising from regions of the sample in different phases. In the temperature region of the transformation the ^{27}Al central line was fitted by the superposition of two gaussians, and in order to get a good fit we had to assume that while the austenite line remains fixed at a the austenite frequency, the second one is centered at a frequency which varies with the temperature. To reduce the number of parameters of the fit, we assume that the the second line shifts proportionally to the fraction of transforming phase already present. In Fig. 2 (a) we report the fraction, and in Fig. 2 (b) the linewidth of transforming phase present in the sample, as obtained from the fit for the two 62% Al alloys.

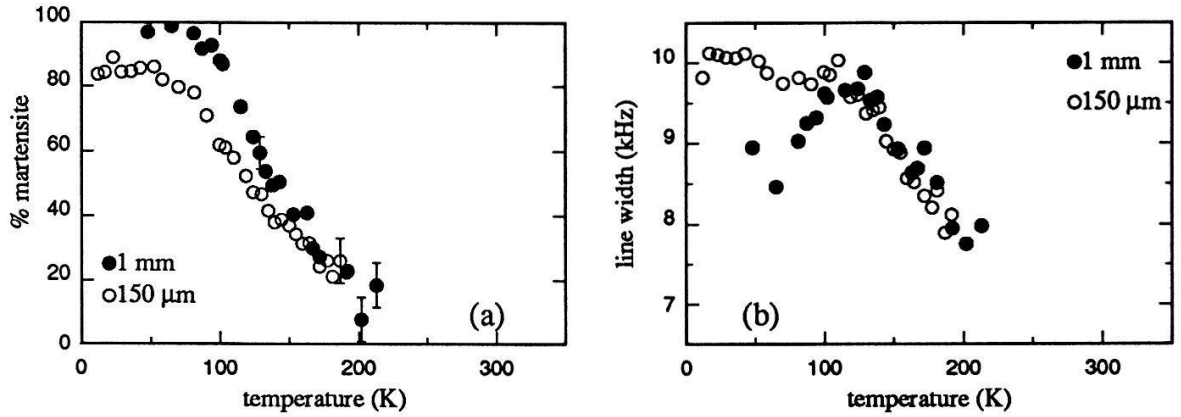

Figure 2

From the results of the fit, two main features become apparent, which do not depend critically on the parameterization used in the fit: the gradual variation of the Knight shift and the broadening of the line pertaining to the transforming phase. The picture emerging from the above results is the one of a formation of nuclei of martensite with an incomplete degree of deformation. The growth of each nucleus is accompanied by a progressive lattice deformation, up to the fully transformed martensite structure. At each temperature, regions of the sample at different degree of transformation coexist in thermoelastic equilibrium, as indicated by the distribution of Knight shift which generates the broadening of the line of the transforming phase. This behaviour is very different from the one of CuZnAl alloys, where one observes a sudden nucleation of about 30 % of fully transformed martensite[1]. In the small particles sample the MPT is not complete and even at low temperature a fraction of about 20 % of austenite is still present, as denoted by the value of the Knight shift and of the linewidth.

[1] S.Rubini, C.Dimitropoulos, R.Gotthardt and F.Borsa, Phys. Rev. B **44**, 2019,(1991)
[2] C.Dimitropoulos, F.Borsa, S.Rubini and R.Gotthardt Journ. de Physique IV **1** C4-307, (1991)

Integral Parameters of Xenon Dendrites

J.H. Bilgram, U. Bisang and E. Hürlimann
Laboratorium für Festkörperphysik, ETH, CH 8093 Zürich

The wide variety of structures of dendrites is due to two nonlinear processes: the formation of sidebranches and the coarsening. Dendritic structures can be characterized by parameters which describe the properties of the integral dendrite. Such integral parameters are the volume, the surface or the contourlength of a projection of the dendrite. Measurements show that parameters which describe the shape of the dendrite scale with the radius of curvature of the dendrite tip R.

We have studied the growth of xenon dendrites into supercooled pure melt [1-3]. We have measured Z_{SB} the distance between the dendrite tip and the position where the first sidebranch has the amplitude 1R. $\bar{Z}_{SB}$ is plotted in units of R as a function of the dimensionless supercooling Δ. We find $\bar{Z}_{SB}/R \sim 18$. This value is independent of the supercooling (fig.1). We compare this result with a prediction [4] based on the hypothesis, that thermal noise in the solidifying melt is selectively amplified to produce sidebranches. The stable region of the tip would be more extended, if pure thermal

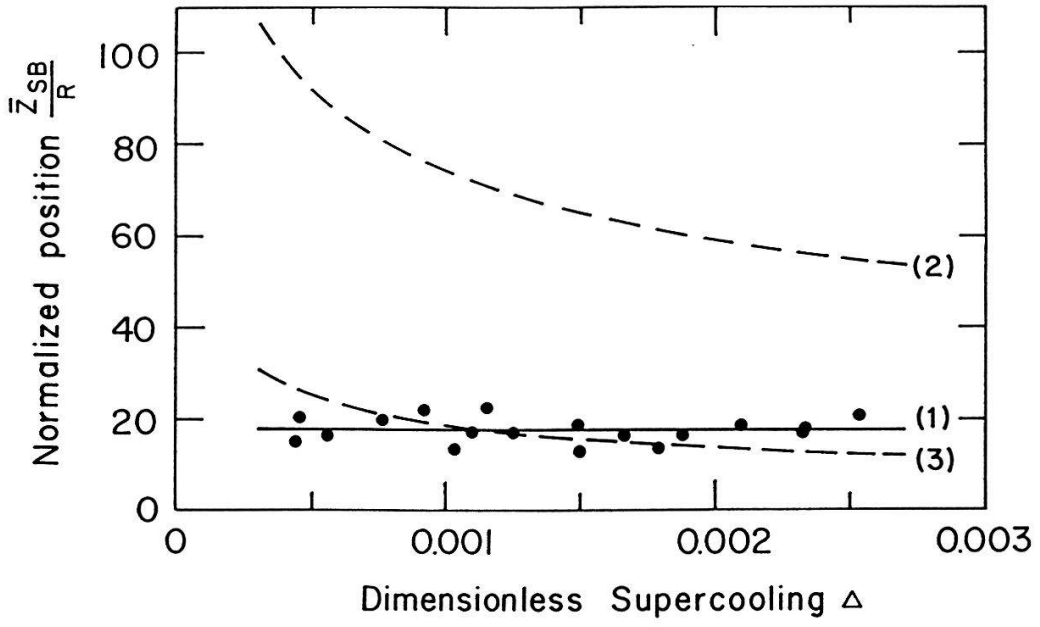

Fig. 1. Normalized average position of the sidebranches with an amplitude of about one tip radius vs. the dimensionless supercooling. The solid line (1) is a linear fit of the data. The theoretical prediction is represented by line (2). (3) is the theoretical prediction fitted to the data. (3) corresponds to the theoretical behaviour with an amplitude of thermal fluctuations increased by a factor of 50.

noise were the reason for the instability leading to side branches. This observation is in agreement with an estimate of Langer [4]. The linear model [4] predicts a temperature dependence of $\bar{Z}_{SB}/R$ which is not observed in the experiment. Tip oszillations have been proposed [4] to be a plausible alternative mechanism to thermal noise. In this case sidebranches would behave like dendrites itself and nonlinear calculations should be performed.

The coarsening of sidebranches far from the dendrite tip is due to nonlinear interactions of sidebranches. We have measured parameters which describe the integral dendrite. These parameters take into account the interaction of the sidebranches. Such integral parameters are e.g. the volume V of the whole dendrite, the surface of a dendrite or the contour surrounding a projection of a dendrite. The integral parameters scale with R as well as the parameters which describe the dendrite close to the dendrite tip:

1.) The thermal gradient close to the dendrite tip is characterized by a length of diffusion. This diffusion length is of the order of magnitude of R.
2.) The length $\bar{Z}_{SB}$ is 18 R.
3.) The sidebranch spacing S near the tip scales with R. S/R is independent of the supercooling [1].
4.) The amplitude w_p of the sidebranches which build the envelope increases with the distance from the tip ℓ_p. $(w_p/R) \propto (\ell_p/R)^{1.72}$.
5.) The projection area F of a dendrite is proportional to the contour length U. The proportionality is 4R [3].
6.) The filling factor $V/(\frac{4\pi}{3}L^3)$ of a sphere which contains a dendrite with an overall dimension L, is proportional to R [2]. Dendrites are no volume fractals.

One might speculate whether the scaling with R is a property of the nonlinear processes active in dendritic solidification. The approach of searching for integral parameter is one that may well prove useful in a wide variety of pattern-forming systems.

Acknowledgements: We thank Prof. H.R. Ott for his support. This work is supported by the Swiss National Science Foundation.

[1] J.H. Bilgram, M. Firmann and E. Hürlimann, J. Cryst. Growth, 96,185(1989)
[2] E. Hürlimann, R. Trittibach and J.H. Bilgram, Helv. Phys. Acta 63,473(1990)
[3]E. Hürlimann, U. Bisang and J.H. Bilgram, Helv. Phys. Acta 65,111(1992)
[4] J.S. Langer, Phys. Rev. A 36,3350(1987)

Synchrotron Radiation Photoemission Study on Amorphous $Au_{30}Sb_{70}$

H.-G. Boyen, G. Indlekofer*, A. Taleb*, R. Gampp, A. Cossy-Favre, P. Oelhafen and F. Baumann‡

Institut für Physik, Universität Basel, Klingelbergstr. 82, CH-4056 Basel, Switzerland; *LURE, Orsay; ‡Physikalisches Institut, Universität Karlsruhe

We report on a photoemission experiment on the valence band structure of amorphous $Au_{30}Sb_{70}$ making use of synchrotron radiation. A strong variation of the photoionization cross section ratio between Au derived d states and Sb derived p states could be observed as a function of the photon energy, qualitatively similar to what is expected for the corresponding gas phase. However, this ratio seems to be reduced by one order of magnitude in the solid phase, indicating the transition from localized to extended Au d-states.

The use of synchrotron radiation has proved to be a powerful tool to determine the electronic structure of matter [1]. The tunability of the photon energy can be used to get information about partial densities of states, since the photoionization cross sections of different angular momentum states depend heavily on the excitation energy.

This work reports on photoelectron spectroscopy on *in-situ* prepared amorphous $Au_{30}Sb_{70}$ in the photon energy range of between 18 and 90 eV. The sample was prepared by quench condensation at about 100 K in a vacuum better than 10^{-9} mbar. In fig. 1a valence band spectra are presented for different photon energies. For better comparison, the spectra have been normalized to the same height at the Fermi level. Two main features can be observed. At binding energies between 7.5 and 3.5 eV all electron distribution curves show a double peaked structure, which is typical for the emission from the Au-5d band [2]. For binding energies lower than 3.5 eV, the curves are characterized by a decrease towards the Fermi edge. This was found to be a consequence of the interaction between the nearly free electrons and the disordered atomic structure [2]. In this binding energy range the intensity can mainly be assigned to Sb-5p states with an additional contribution of Au-6s states. Obviously there is a significant difference in the evolution of the band shape between these two regions. With increasing photon energy the distribution of the Sb-5p electrons remains more or less unchanged. On the other hand, a rapid increase of the Au-5d band emission followed by a similar rapid decrease can be recognized.

In order to estimate these changes, the intensities of both the Au-5d as well as Sb-5p bands have been integrated using a linear background (see fig. 1a). Although this seems to be a crude approximation it should be sufficient to obtain the right order of magnitude of the observed changes. Because of the small number of Au-6s electrons compared to the Sb-5p states in the alloy (1:7), the Au-6s contribution has been neglected. The resulting intensity ratio between the Au-5d and Sb-5p intensities has been plotted in diagram 1b, where a maximum occurs at a photon energy between 30 and 40 eV. Theoretical data have been added, which are based on atomic orbital cross sections [3]. They should represent a good approximation of the properties of a mixture of isolated atoms. There is a clear correspondance between the two sets of data, concerning the overall shape of the curves. However, the absolute values differ by more than one order of magnitude. Such discrepancy can be understood as a consequence of overlapping d orbitals from different Au sites, i.e. as the beginning of the formation of a common Au d band in this alloy.

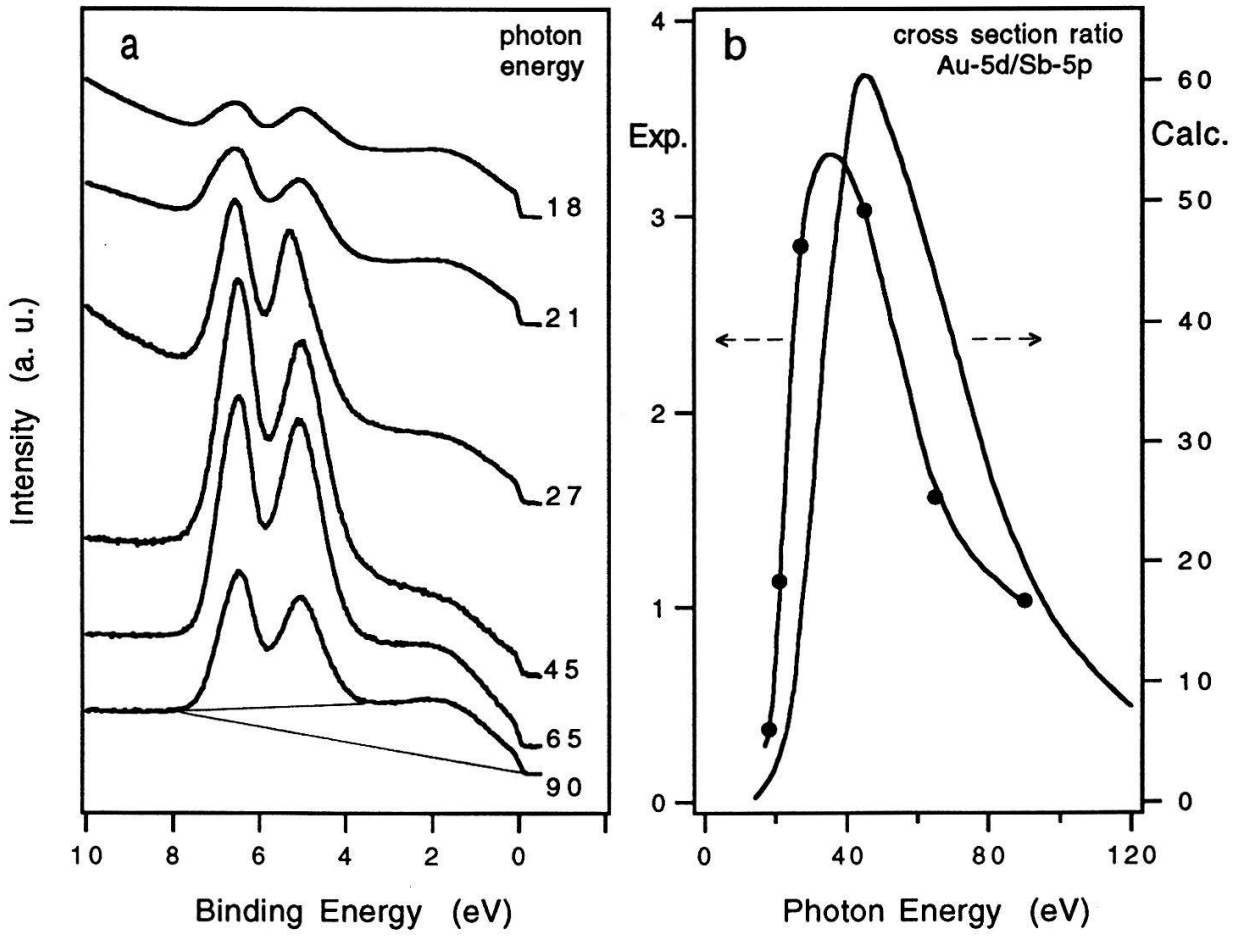

Figure 1:
a) valence band spectra of amorphous $Au_{30}Sb_{70}$ measured at different photon energies. b) experimental (left scale) as well as theoretical (right scale) ratio between Au-5d and Sb-5p cross sections as function of the excitation energy.

In conclusion strong variations of the partial photoionization cross sections have been found, quite similar in shape to what is expected for isolated atoms. However a quantitative analysis reveals strong differences, indicating the building up of a common d band in the condensed state.

Financial support by the Swiss National Science Foundation is greatfully acknowledged.

References

[1] P. Oelhafen, A. Pflugi, G. Indlekofer : J. Non-Cryst. Solids **117/118**, 267 (1990)

[2] P. Häussler : *Glassy Metals III* (Springer Topics in Applied Physics 53) ed H. Beck and H.-J. Güntherodt (Berlin: Springer) submitted

[3] J.J. Yeh, I. Lindau : At. Data and Nucl. Data Tables **32**, 1 (1985)

Preparation and Sputtering Effects in Amorphous Fe_XZr_{100-X}

A. Cossy-Favre, H.-G. Boyen and P. Oelhafen

Institut für Physik, Universität Basel, Klingelbergstr. 82, CH-4056 Basel, Switzerland

Amorphous Fe_XZr_{100-X} films have been prepared *in-situ* by means of electron beam evaporation. Whereas *ex-situ* methods like melt-spinning and splat-cooling are restricted to very narrow concentration ranges, co-evaporation of the pure components allows the synthesis of alloys over an extended concentration range. Most importantly, sputter cleaning of the sample surface can be avoided, which may cause significant changes in the electronic structure as seen by photoemission.

Because of its technologically very interesting properties such as ferromagnetism combined with a high stability against crystallization, amorphous Fe-Zr has attracted much interest in the last decade. A lot of experimental as well as theoretical efforts have been undertaken to learn about the basic properties of this alloy. So far, most experimental work has been done on *ex-situ* prepared alloys within very restricted concentration ranges (x = 20-40, 88-92 [1]). We report about an *in-situ* photoemission study on vapour-quenched alloys in a concentration range between 25 and 82 atomic percent Fe.

Fig. 1a shows valence-band spectra which were measured at a photon energy of 21.2 eV. The electron distribution curves consist of a main peak located between 2 eV and the Fermi energy, a shoulder at about 2.5-3 eV, and an additional feature at a binding energy of 5-6 eV. The latter structure is mainly due to adsorbed residual gas atoms as demonstrated in fig. 1b, which displays the time evolution of the spectral shape. This peak is found to increase slightly with time even at a pressure below 10^{-10} mbar and can be correlated with an increasing oxygen signal in the core level spectra. Fig. 1b clearly demonstrates that the observed amout of contamination has no significant influence on the band shape between 4 eV and the Fermi edge, where the main part of the occupied electronic states density is located. Therefore all spectra in fig. 1a can be interpreted in terms of the electronic density of states without the need of a sputter cleaning procedure (a detailed comparison with theoretical photoemission data will be the subject of a further publication [2]).

The influence of sputtering is shown in fig. 1c. Drastic changes in the band shape are visible for the ion bombarded sample. In addition to the cleaning effect, the concentration of the sample seems to be highly altered. According to fig. 1a the cleaned alloy resembles very closely to an alloy with x = 60. However, such a change in composition could not be detected by core-level analysis, which can easily be understood as due to an inhomogeneous vertical concentration profile at the sample surface. Furthermore sputter cleaning seems to increase the intensity of the shoulder which is located at a binding energy of 3 eV.

We conclude, that investigations on such alloy systems with surface sensitive methods should be carried out on *in-situ* prepared samples in order to prevent possible changes in the surface region generated by destructive cleaning methods.

Financial support by the Swiss National Science Foundation is greatfully acknowledged.

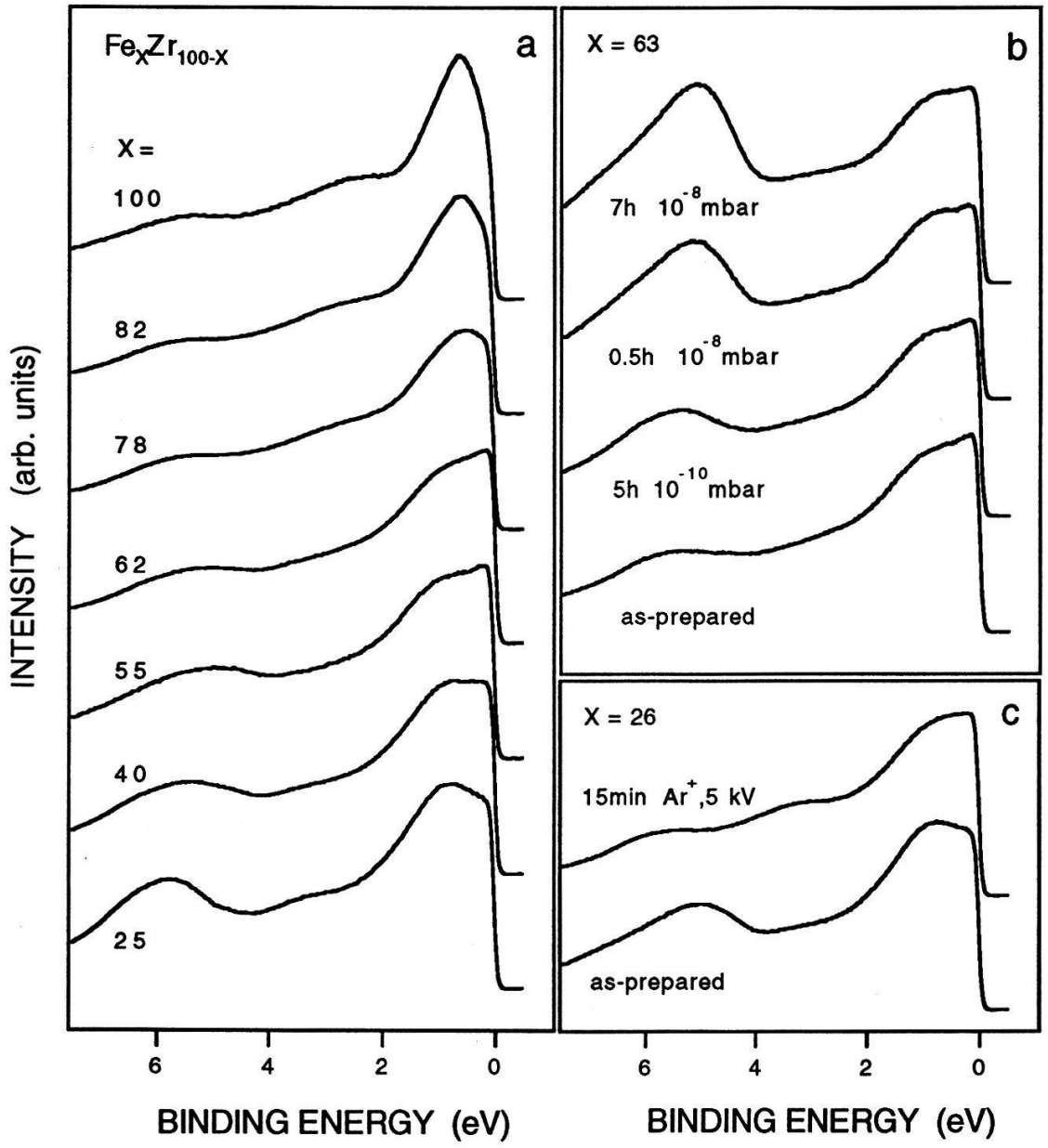

Figure 1:
a) valence band spectra of amorphous Fe_XZr_{100-X} films measured at a photon energy of 21.2 eV (HeI). b) HeI spectra of $Fe_{63}Zr_{37}$ as function of time and pressure. c) HeI spectra of an as-prepared and sputter cleaned $Fe_{26}Zr_{74}$ sample.

References

[1] *Physical Data of Amorphous Metals*, eds. H. Behrens and H.-W. Müller, Fachinformationszentrum Karlsruhe

[2] A. Cossy-Favre, H.-G. Boyen, P. Oelhafen : to be published at the 8th conference on Liquid and Amorphous Metals, Vienna

Inverse-photoemission in Kondo systems.

D. Malterre, M. Grioni, P. Weibel, B. Dardel and Y. Baer

Institut de Physique, Université de Neuchâtel, CH-2000 Neuchâtel Switzerland

abstract : Physical properties of Kondo systems are governed by the existence of a characteristic energy scale (the Kondo energy k_BT_K). For $T \ll T_K$, the f electrons form a local Fermi liquid whereas at high temperature ($T \gg T_K$), the localized character of the f state is restored. We show that, despite its poor resolution ($\Delta E \sim 700$ meV), inverse-photoemission spectroscopy is sensitive to the relevant low-energy scale.

Thermodynamical properties like magnetic susceptibility or specific heat indicate a crossover between the low-temperature singlet state and the high-temperature magnetic regime. This behaviour is interpreted as the breakdown of the singlet ground state resulting in the disappearance of the Kondo resonance when temperature increases. The aim of our study is to demonstrate that high-energy spectroscopies are not only sensitive to the correlation energy ($U \approx 6$eV) but also can reflect the low-energy excitations corresponding to the thermal evolution.

Figure 1 shows the inverse photoemission spectrum of a typical Kondo compound $CeSi_2$ (T_K=35 K) for T=15 K and T=300 K. A significant temperature dependence is clearly observed: the intensity of the low-energy structure is strongly depleted with increasing temperature. In order to extract the 4f contribution, we remove a background (dashed line in figure 1) which represents the transition toward non-f states and the inelastic contribution and

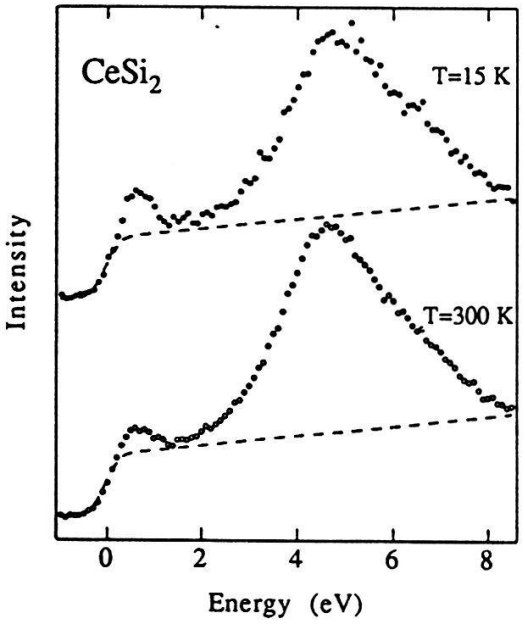

Figure 1 : Inverse-photoemission spectra of $CeSi_2$ for T= 15 K and T=300 K. The dashed line represents the non-f contribution.

we plot the resulting 4f spectral function in figure 2(a). The two experimental structures at E=0.5 eV and E=5 eV represent final states with a f^1 and f^2 character respectively. As demonstrated by calculations in the framework of the Anderson model [1], the f^1 structure contains two contributions : the Kondo resonance at $\delta=k_BT_K$ and a spin orbit satellite at $\delta+\Delta_{S.O.}$ which are both depleted with the characteristic Kondo temperature scale. This temperature dependence can be qualitatively understood: the singlet ground state is an hybridized state ($n_f<1$) separated by k_BT_K from the excited magnetic states ($n_f=1$). At low temperature ($T\ll T_K$), only the singlet ground state is populated and the low-energy BIS-structure reflects the amplitude of the $4f^0$ configuration in the initial state. With increasing temperature, the excited states are progressively populated ($<n_f>$ increases) leading to a reduction of the f^0 amplitude in the initial state. As a consequence, the weight of the f^1 structure follows the evolution of the average 4f occupation number with temperature and as shown in fig. 2(b), a qualitative agreement is obtained between experimental and theoretical spectra calculated in a simplified model [3]. To summarize, inverse-photoemission measurements on $CeSi_2$ clearly evidence the temperature dependence of the Kondo resonance. Then spectroscopic measurements, despite their high-energy character, are sensitive to the low-energy scale responsible for all the physical properties in Kondo systems.

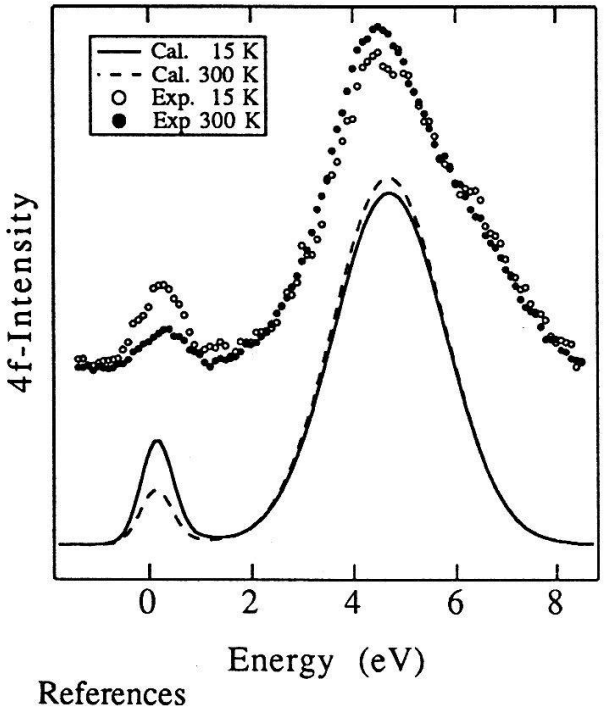

Figure 2 : Experimental (a) and calculated (b) 4f spectral function of $CeSi_2$ for T= 15 K and T=300 K.

References

[1] P.A. Lee et al Comm. in Condensed Matter Phys. 12, 99 (1986).
[2] N.E. Bickers, D.L. Cox and J.W. Wilkins, Phys. Rev. B 36, 2036 (1987).
[3] D. Malterre, M. Grioni, P. Weibel, B. Dardel and Y. Baer, submitted in Phys. Rev. Lett.

PHOTOEMISSION AND CHARACTERIZATION OF ONE-DIMENSIONAL SYSTEMS

B. Dardel, D. Malterre, M. Grioni, P. Weibel and Y. Baer
Institut de physique, Université de Neuchâtel

Abstract : Metallic systems are characterized by a finite density of states at the Fermi level (E_F) which is commonly reflected by a step in the photoemission spectral function. Although this step is always observed in two- and three-dimensional systems, we show that this is not the case for quasi-1D-systems where the spectral function vanishes at E_F.

From a theoretical point of view, one-dimensional (1D)-systems exhibit many pathological features such as an instability of the electron gas leading to formation of charge density wave, strong fluctuations which suppress any phase transition at finite temperature, and electronic correlations that modify the Fermi liquid picture [1]. One of the main difficulty in dealing with real low-dimensional compounds is their classification in 1D- or 2D-systems. Up to now only non-conclusive estimates of the dimensionality have been obtained from structure considerations, anisotropy of physical properties such as electrical resistivity, and geometry of the Fermi surface; however, considerable controversy exists between different techniques or authors.

In this paper we demonstrate that high resolution photoemission is a powerful tool for the determination of the dimensionality. The characteristic features of 1D-systems appear to be :
- the lack of dispersion in the plane perpendicular to the chains
- the extremely low intensity of the spectral function at the Fermi level.

We have studied 5 compounds, belonging to different families considered to be 1D [2], in their metallic phase. Their photoemission spectra were taken with an helium discharge lamp (21.22 eV). The energy resolution of the spectrometer was better than 20 meV, while its angular resolution was approximately ±3°. The samples were cleaved in ultra-high vacuum.

For 1D-systems, dispersion is expected only in the chain direction; angular dependence of the spectral function (in the plane perpendicular to the chains) that reflects electronic coupling between chains, was clearly observed for $HfTe_5$ (figure 1) and $Li_{0.9}Mo_6O_{17}$. This unambiguously indicates the bi-dimensional character of these systems. The other materials did not exhibit any dispersion (neither perpendicular nor along the chains direction), which suggests that the broad structure seen in these compounds (at 300, 500 and 1100 meV for $K_{0.3}MoO_3$, $(TaSe_4)_2I$ and $(TMTSF)_2PF_6$ respectively) does not reflect a one-electron band structure.

The figure 2 shows the photoemission spectra of the measured compounds around the Fermi energy. We expect a step at E_F reflecting the metallic character of these

systems. This step is present only for the two compounds that show dispersion; thus, as discussed in a previous paper [3], we regard its absence as an intrinsic feature associated with the exotic character of 1D-systems.

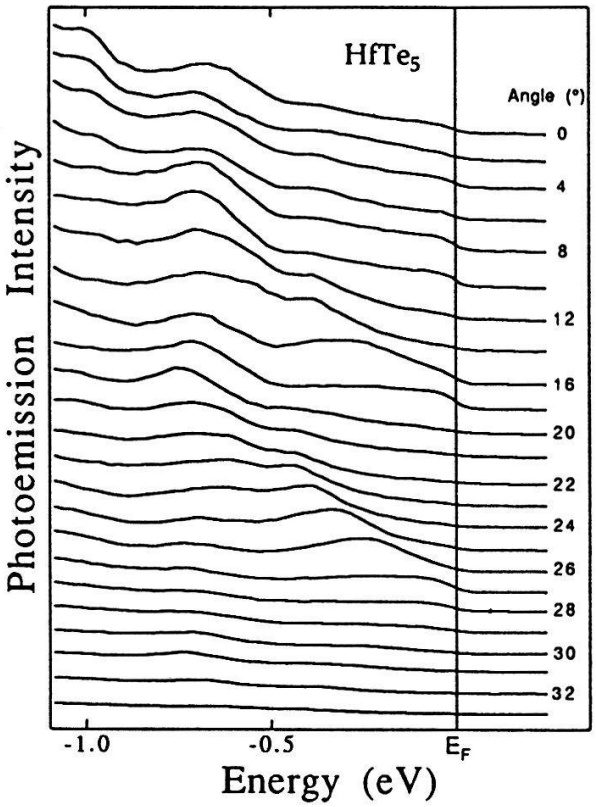

Figure 1 : Angular dependence (in the plane perpendicular to the chains) of the photoemission spectral function of $HfTe_5$. The angle 0 correspond to normal emission. The dispersion of the band structures reveals the 2D character of the system.

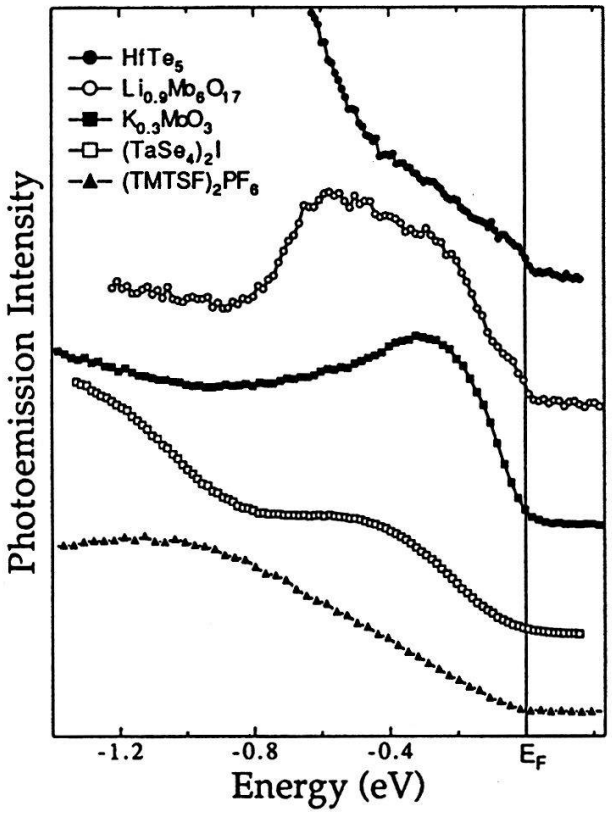

Figure 2 : Photoemission spectra of different samples in their metallic phase (at normal emission). The main feature is the absence of intensity at E_F for some of them which can be interpreted as the signature of uni-dimensionality.

These results support that high resolution photoemission can provide a phenomenological criterion (low spectral intensity at the Fermi level) for the determination of the 1D character owing to the peculiar features of 1D-systems.

References :

[1] S. Kagoshima, H. Nagasawa and T. Sambongi, One-Dimensional Conductors, 1988, Solid State Sciences 72 (Springer Series, Berlin/Heidelberg/New York).

[2] Physics and Chemistry of Materials with Low-Dimensional Structures, 1989, ed. F.Lévy, Kluwer Academic Publishers (Dordrecht/Boston/London)

[3] B. Dardel, D. Malterre, M. Grioni, P. Weibel, Y. Baer and F. Lévy, Phys. Rev. Lett. **67**, 3144, (1991)

Reflection of H Ly-Alpha from Rough Surfaces

Th. Zurbuchen

Physikalisches Institut, Universität Bern, CH-3012 Bern, Switzerland

In space research, electrostatic analyzers are often used in combination with time-of-flight spectrometers for the characterization of solar wind ions. Because these mass-analyzers are light-sensitive, it is important that an energy analyzer has good suppression qualities, in particular in the UV range. We have examined the UV absorption and reflection qualities of several materials which are frequently employed for the construction and surface treatment of ion-optical instruments. We present results of these investigations and compare them with model calculations.

We have investigated a set of surface samples which are of practical use for the manufacturing of electrostatic analyzers employed in space research. We measured two Al samples of different surface roughnesses. An Al surface mirror, produced at the NBS (National Bureau of Standards), and a polished Al surface are thought to be good specular reflectors. An Al_2O_3 ceramic was also included into this investigation because of its importance as a material for construction. Various surface treatments have been used to suppress foreward scattering of light and to obtain small reflection coefficients. Among them a copper-sulfide blackening, produced by Flühmann Limited in Dübendorf/Switzerland, has been measured because of its practical importance as the best and most widely used blackening.

In order to understand our measurements, we compare the results with calculations of the so-called Kirchhoff theory. This theory provides an approximation to the wave field on the surface of the scatterer. Any point on a scatterer is treated as if it were part of an infinite plane, parallel to the local surface tangent. Therefore, the theory is exact for an infinite plane scatterer. Because multiple scattering and shading effects are neglected, the approximation becomes poorer with increasing roughness. This theory and its applications have been reviewed by Ogilvy [1]. The theory in the formulation used here calculates the backscattering of a plane monochromatic wave from a surface with a Gaussian height probability distribution with a RMS deviation s. In addition, the autocorrelation function of the surface is Gaussian with a correlation length of l. s and l are always given in units of the wave length λ.

In the experiment, a parallel, nearly monochromatic beam with a wave length of 121.6 nm is sent to a surface sample and scattered there. The reflection profiles are measured by a channeltron in the plane of the surface normal and the incident beam. The channeltron sees a solid angle of 5×10^{-3}sr. The set-up is described in more detail by Zurbuchen [2].

Figure 1 shows the measured reflectivities of the two Al surfaces. It is evident that the intensities are growing with Θ_1 because of the finite value of the conductivity in this range. The differences of the measured stray characteristics are caused by differing roughnesses of the two surfaces. For a Gaussian distribution function and a pure Al_2O_3 surface, the reflected intensity can be calculated. The comparison between measurements and calculations is also shown in Figure 1.

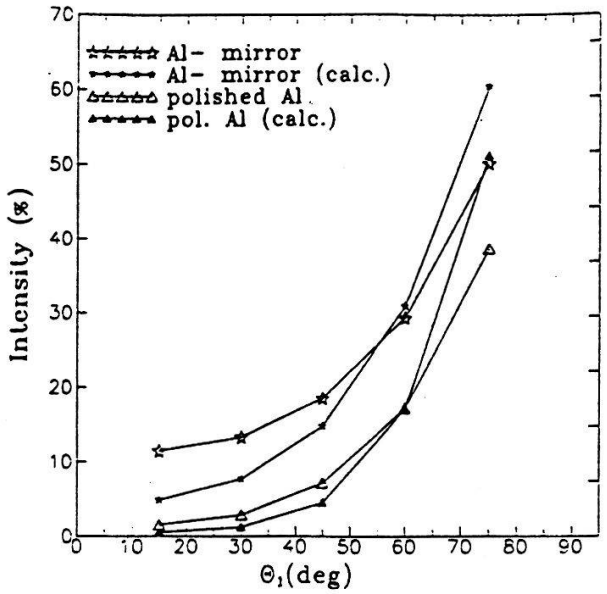

Figure 1:
Ratios of incident and specularly reflected intensities for varying Θ_1, measured on an Al mirror and a polished Al surface compared with the calculated reflectivities of Kirchhoff rough surfaces.

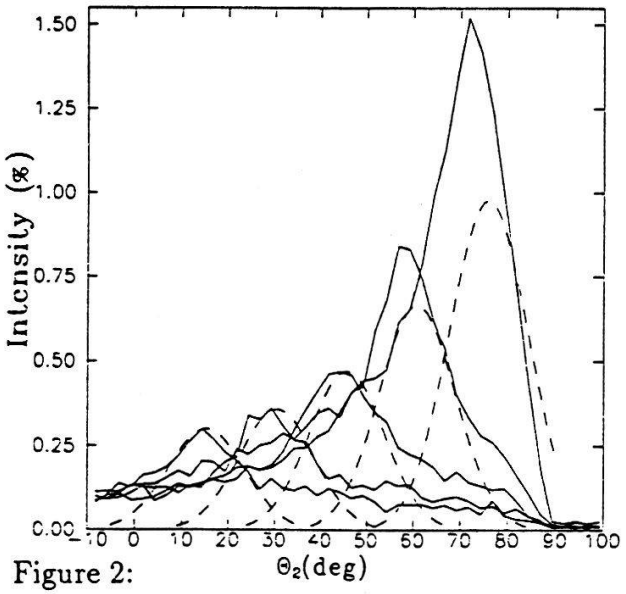

Figure 2:
Reflected intensity of an Al_2O_3 ceramic seen by a solid angle of 5×10^{-3}sr, compared with a calculated profile with l=100λ and s=5λ.

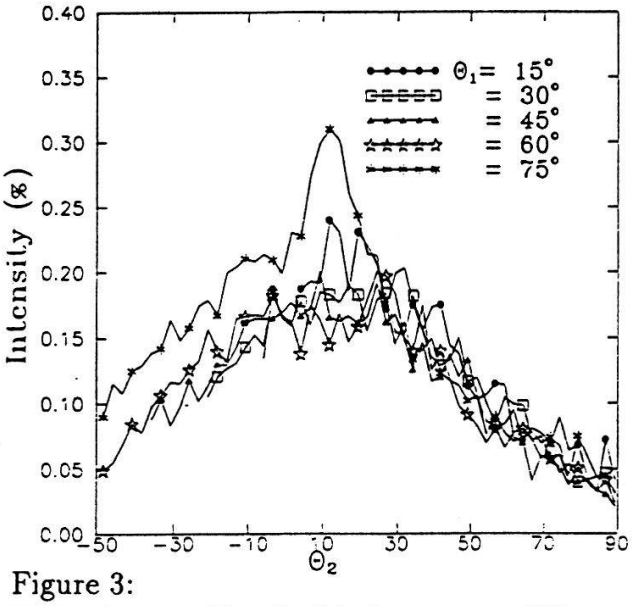

Figure 3:
Reflection profile of a black copper-sulfide surface sample with an almost Lambertian characteristic.

Figure 2 shows the reflected intensities for different Θ_1's as a function of Θ_2, the angle between surface normal and scattering direction in the plane of the incident beam and the surface normal. The reflection characteristics are fairly well reproduced by an Al_2O_3 surface with a Gaussian autocorrelation function of $l = 100\lambda$ and a height distribution function with $s = 5\lambda$. The observed deviations for big Θ_1's are possibly due a different composition of the surface or by different surface characteristics.

The results of the measurements on copper-sulfide are given in Figure 3. The profiles show a cosine shape as expected for a black body. The reflectivities depend on Θ_1, they are always below 0.5 percent.

References

[1] Ogilvy, Theory of Wave Scattering, Adam Hilger, Bristol (1991)
[2] Zurbuchen, Master Thesis, University of Bern (1992)

ELECTRONIC STRUCTURE OF SPUTTERED HYDROGEN FREE CARBON FILMS

S.Maurer, P.Oelhafen, P.Gantenbein, P.Kania, S.Schelz and R.Steiner
Institut für Physik der Universität Basel, Klingelbergstrasse 82, 4056 Basel, Switzerland

Carbon films have been prepared by rf sputtering using different plasma power densities and substrate temperatures. After deposition, the films have been analyzed in situ by photoelectron spectroscopy (UPS and XPS). The valence band spectra clearly reveal the features of disordered carbon network. In comparison with the semimetallic graphite the valence band edge is shifted to higher binding energies indicating the opening of a band gap at E_F. The relative amount of sp^2 bonds has distinctly decreased as compared with our findings on evaporated carbon films.

Introduction A wide variety of carbon based films with considerable technological interest, ranging from sputtered films to diamond-like films (a-C:H, CVD diamond) and the latest discovered fullerene films can nowadays be prepared. In order to understand the physical properties of these films, a detailed knowledge of the electronic structure is required. Photoelectron spectroscopy has proved to be a powerful tool for the characterization of these films [1]. In the present communication we apply this technique to the analysis of sputtered C films in order to get additional information on the electronic and atomic structure of these materials. A crucial question is the relative amount of threefold (graphite-like) sp^2 to fourfold (diamond-like) sp^3 bonds present in these materials.

Experimental The films have been prepared by rf (13.56MHz) magnetron sputtering using Ne in a custom built high vacuum plasma deposition chamber attached to a combined UPS, XPS and AES electron spectrometer (Leybold EA10/100). A polycrystalline graphite disk (diameter 90mm) and Si(100) wafers were used as target and substrates, respectively. The pressure during sputtering was typically $6 \cdot 10^{-3}$mbar and a flow of 30.0 sccm was used. The rf power has been varied between 50W and 400W, leading to self bias voltages between -160V and -430V and the deposition temperature independently controlled between room temperature (RT) and 275 °C. The UPS and XPS measurements on the films transferred to the UHV analysis chamber in situ have been performed by operating the spectrometer with a constant retardation ratio of 3 and a pass energy of 50eV leading to an overall energy resolution of 0.1eV. The binding energy calibration has been performed by setting the Au $4f_{7/2}$ line on a reference sample at 84.0eV.

Results Figure 1 shows valence band (VB) spectra (HeI (21.22eV) and HeII (40.8eV) excitation) of films prepared with different rf powers. The overall shape of these films is similar to those obtaind from a-C:H films [1]. The spectra display basically a dominant peak related to σ electron states at about 7eV and a shoulder near 4eV related to the π electrons. Figure 1 highlights the following points: (i) the influence of the rf power on the VB spectra is rather small; (ii) the extrapolated VB edge (E_{VB}) is located at about 0.5eV and (iii) the HeII spectra show a peak at binding energy of 14.6eV. A careful analysis of the data clearly attributed the origin of the latter peak to Ne 2p electron states. In fact, sample deposited at RT showed slight Ne contamination (below 1at%) as evidenced by XPS analysis. The VB spectrum of a sputtered C film is compared to those of an a-C:H [1] and an evaporated C film [3] in Figure 2, showing the substantially higher amount of π electrons in the evaporated film. The VB edge position E_{VB} with respect to E_F of the sputtered film is similar to that in a-C:H whereas the semimetallic character of the evaporated film is clearly reflected by the value of $E_F - E_{VB}$ close to zero. The influence of the substrate temperature is shown in Figure 3. An increased substrate temperature has basically three effects: (i) the π peak becomes more prominent, (iii) E_{VB} is shifted towards E_F and (iii) the peak at 14.6eV disappears.

These observations indicate a more graphitic structure for these samples. The C1s binding energies of all C films prepared by sputtering fall within a 284.5 to 284.8eV range and are close to those of graphite and diamond (284.8eV) [2] and a-C:H (284.6) [1]. The stability of the sputtered films turned out to be rather poor. A 5 min exposure to atmosphere showed a substantial oxygen uptake (about 6at%) and caused the peeling off of the films revealing their rather poor adhesion to the Si substrate.

In conclusion the films studied in this work exhibit a fairly low amount of sp^2 bonds when deposited at room temperature as compared to evaporated films. The VB edge indicates an opening of a band gap at E_F. The higher chemical reactivity to oxygen as compared to that of a-C:H implies an appreciable amount of non saturated bonds in the film. The observed peeling of the films upon exposure to air may be related to a significant stress in the film.

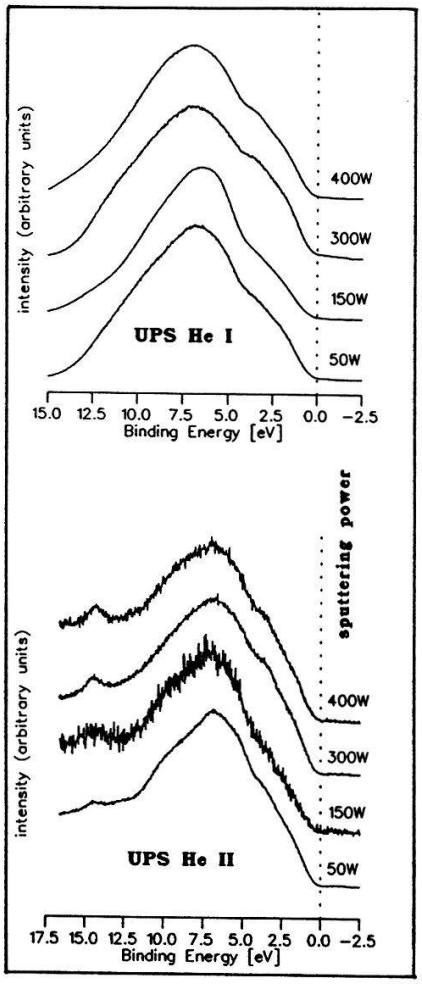

Fig.1:UPS VB spectra of sputtered C films deposited at different rf powers

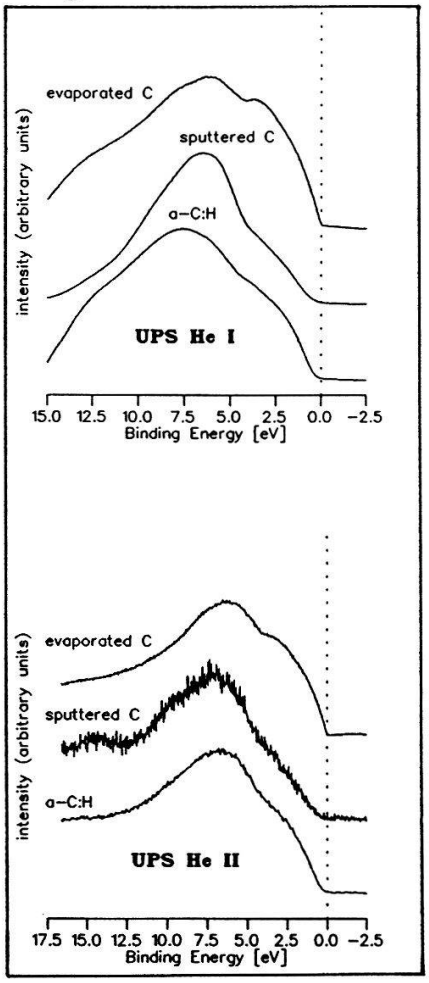

Fig.2:UPS spectra of three different C films: evaporated C [3], sputtered C and a-C:H [1]

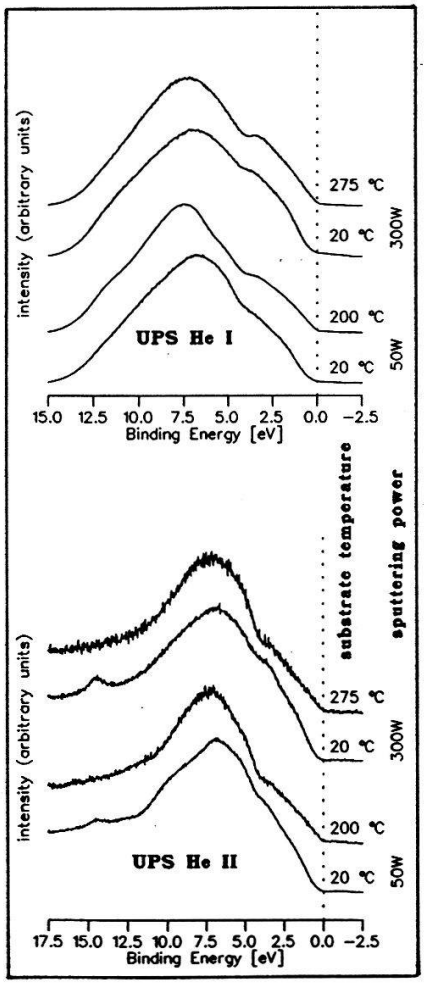

Fig.3:UPS VB spectra of sputtered C films deposited at different substrate temperatures and rf powers

Acknowledgements We thank Dr.J.Ullmann for valuable suggestions and Dr.A.Mansour for careful reading of the manuscript. Financial support of the Bundesamt für Energiewirtschaft, the Bundesamt für Bildung und Wissenschaft and the Swiss National Science Foundation is greatfully acknowledged.

References [1] P.Oelhafen, D.Ugolini, S.Schelz, J.Eitle, Diamond and Diamond-like Films and Coatings, Plenum Press, New York (1991)
[2] A.Mansour, G.Indlekofer, P.Oelhafen, Appl.Surf.Sci.48/49, 312 (1991)
[3] J.Ullman et al., to be published.

MICROSTRUCTURE AND ELECTRICAL PROPERTIES OF BISMUTH FILMS PREPARED BY RF SPUTTERING

Frank Bommeli, Takeshi Fukami*, Edgar Holguin and Leo Rinderer
Institut de Physique Expérimentale, Université de Lausanne, CH-1015 Lausanne.
*On leave from Department of Physics, Kyushu University, Fukuoka 812, Japan.

We found out a method to enhance the percent ratio of the 110 K phase of the Bi-Sr-Ca-Cu system and to prepare it reproducibly. The films were prepared by RF sputtering with raw compound powder target. The analysis of the microstructure of Bi-Sr-Ca-Cu samples revealed the existence of some non superconducting phases like CuO_2 nodules and $PbCa_2O_4$ needles. Finally we measured the temperature dependence of J_c for the $Bi_2Sr_2CaCu_2O_y$ phase that follows the Ambegaokar-Baratoff model.

1. INTRODUCTION

At least four distinct superconducting phases exist in thin films of the Bi-Sr-Ca-Cu-O system. The first one with a critical temperature $T_c \approx 20$ K discovered by Michel et al. [1] has the composition of $Bi_2Sr_2CuO_y$. Adding calcium creates at least three additional superconducting phases. One of them has the composition of $Bi_2Sr_2CaCu_2O_y$ and exhibits the superconducting transition at $T_c \approx 80$ K. Another one has the composition of $Bi_2Sr_2Ca_3Cu_4O_y$ and the one with the higher T_c is $Bi_2Sr_2Ca_2Cu_3O_y$ and $T_c \approx 110$ K.

Even when prepared from raw powder with the exact stoichiometric ratio of the 110 K phase, two phases with $T_c = 80$ K and 110 K generally coexist. Furthermore, it is very difficult to obtain the 110 K phase reproducibly without adding a proper quantity of lead. Here we describe a further method to increase the ratio of the 110 K phase with respect to the 80 K phase [2,3]. We used X-ray powder diffraction to estimate the percent ratio of these two phases. We analyzed the microstructure of the samples by EPMA (Electron Probe Micro Analyses). We measured J_c vs. $(1 - T/T_c)$ only for the 80 K phase because we could not obtain the pure 110 K phase.

2. SAMPLE PREPARATION

We prepared the target only by mixing raw powders of Bi_2O_3, PbO, SrO, CaO and CuO in the ratio of Bi:Pb:Sr:Ca:Cu = 2:0.8:2:2:3. Then we prepared the films by RF sputtering on a single crystalline MgO (100) substrate. Experimental conditions were as follows: Argon pressure 0.1 mb and the substrate temperature 600°C. After sputtering, we placed some films into a box made of Al_2O_3 along with a sintered ceramic (Bi:Pb:Sr:Ca:Cu = 1.6:0.4:2:3:4) and annealed them at 857°C for 10 hours. The other films were processed outside the box. Table 1 gives the percent ratio of the 110 K phase with respect to the 80 K phase for these two groups. The results clearly show that the percent ratio increases when we use the Al_2O_3 box. From a Fisher test made on both standard deviations, we can affirm with a probability of 95% that the use of the box also enhances the reproducibility of the 110 K phase. The results suggest that the ceramic compensates the matter loss from the film during the thermal process.

Table 1. Percent ratio between phases 110 K and 80 K estimated from the (002)-lines in a X-ray powder diffraction. **In** and **Out** means the cases with and without the Al_2O_3 box.

In (%)	Out (%)
68	5
68	47
86	33
66	80
average	
72	41
standard deviation	
8	27

3. RESULTS AND DISCUSSION

3.1. Microstructure

The composition of elements was analyzed for the sample with the highest ratio (87%) of the high T_c phase (110 K) by EPMA. The analysis gave the following composition: $Bi_{2.1}Pb_{0.2}Sr_{1.8}Ca_2Cu_{3.2}O_{9.8}$. It is notable that the ratio of the elements is close to the stoichiometric one that is $Bi_2Pb_{0.2}Sr_2Ca_2Cu_3O_y$ for a pure (110 K) phase. We could also identify some non superconducting phases such as CuO_2 nodules and $PbCa_2O_4$ needles.

3.2. Critical current

According to the Ambegaokar-Baratoff theory that is valid for samples consisting of superconducting domains and weak junctions between them [4], the critical current density J_c has a temperature dependence of

$$J_c \propto (1-\frac{T}{T_c})^n \qquad (1)$$

where the value of the exponent n changes from 0 to 3/2 depending on the range of temperatures (from $T \approx 0$ to T_c). Figure 1 shows the data obtained on a film with predominant 80 K phase. The critical temperature of $T_c \approx 69$ K was determined as the temperature where the derivative dR/dT on the resistive curve R(T) has a maximum value. The extrapolated critical current at T = 0, $J_c(0)$, is about $2 \cdot 10^3$ A/cm^2.

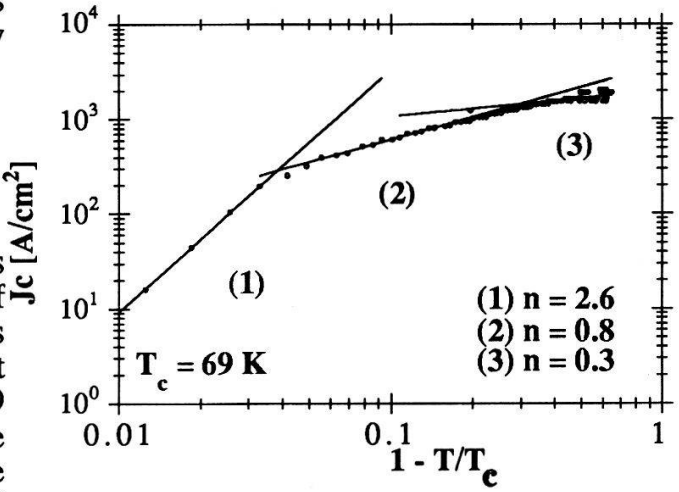

Figure 1. Plots of J_C vs. $(1 - T/T_C)$. $J_C(0) = 2 \cdot 10^3$ A/cm^2.

The experimental data show the similar trend of the temperature dependence as the one predicted by the theory except at the region near T_c. Since the temperature dependence near T_c is sensitively dependent on the value of T_c, we do not discuss the results close to T_c. As we could not reach temperatures below 20 K, the result n = 0.3 is not surprising and can only reflects a tendency. To confirm that the temperature dependence proposed in [4] is general, we must obtain the similar behavior of J_c vs. $(1 - T/T_c)$ for each single phase. For that purpose we have to improve our processing techniques to produce single superconducting phase films.

ACKNOWLEDGMENTS — The authors are indebted to G. Burri and G. Troillet for the analysis by EPMA. The Swiss National Science Foundation financially supported this work.

REFERENCES

[1] C. Michel, M. Hervieu, M.M. Borel, A. Grandin, F. Deslandes, J. Provost and B. Raveau, Z. Phys. **B68**, 412 (1987).
[2] T. Fukami, E Holguin, H. Nakano and L. Rinderer, Helv. Phys. Acta. **64**, 894 (1991).
[3] T. Fukami, E Holguin, H. Nakano, K. Schenk and L. Rinderer, Helv. Phys. Acta. **65**, No 2 (1992).
[4] B. Ambegaokar and A. Baratoff, Phys. Rev. Let. **10** (1963) 486 and ibid **11** (1963) 104.

Surface structure of thick $YBa_2Cu_3O_{7-\delta}$ films

H.P. Lang, H. Haefke, G. Leemann and H.-J. Güntherodt

Institute of Physics, University of Basel, Klingelbergstr. 82, CH-4056 Basel, Switzerland

(001) oriented $YBa_2Cu_3O_{7-\delta}$ films with a thickness up to 1.2 μm were prepared by pulsed laser deposition. Scanning tunneling microscopy surface investigations reveal a terrace structure with steps of one unit cell height and growth pits.

Thin film preparation of high T_c superconductors (HTSC) by pulsed laser deposition (PLD) [1] yields films with outstanding superconducting properties compared to polycrystalline bulk material. Since electrical properties of HTSC films and film structure are closely related, a thorough study of the film structure is essential for an improvement of the superconducting properties. Recently, scanning tunneling microscopy (STM) has been used to image the surface structure of magnetron-sputtered (001) oriented $YBa_2Cu_3O_{7-\delta}$ (YBCO) films [2,3] of a thickness of about 150-300 nm. It has been found that the surface structure of the films is dominated by spiral growth hills at emergence points of screw dislocations with a Burgers vector component perpendicular to the film surface. These screw dislocations could act as possible potential pinning centres for flux lines. In this paper we report on STM investigations on (001) oriented YBCO films with a nominal thickness of 1.2 μm prepared by PLD. Films of that thickness are commonly used for microwave device applications.

Thin films of YBCO were grown by PLD on $LaAlO_3$(100) crystals at substrate temperatures between 790 and 805 °C and 27 Pa O_2 using a KrF excimer laser (Lambda Physik LPX 301i, $\lambda = 248$ nm, 1.2 J/shot) focussed onto a stoichiometric high density YBCO target which was rotated to ensure continuous ablation. A deposition time of 20 minutes at a laser repetition rate of 8 Hz yields a nominal film thickness of 1.2 μm. Thereafter, the heating block with the sample was cooled to 500 °C at a rate of 5 deg/min in an oxygen atmosphere of 10^5 Pa, annealed for 30 minutes and then cooled to room temperature.

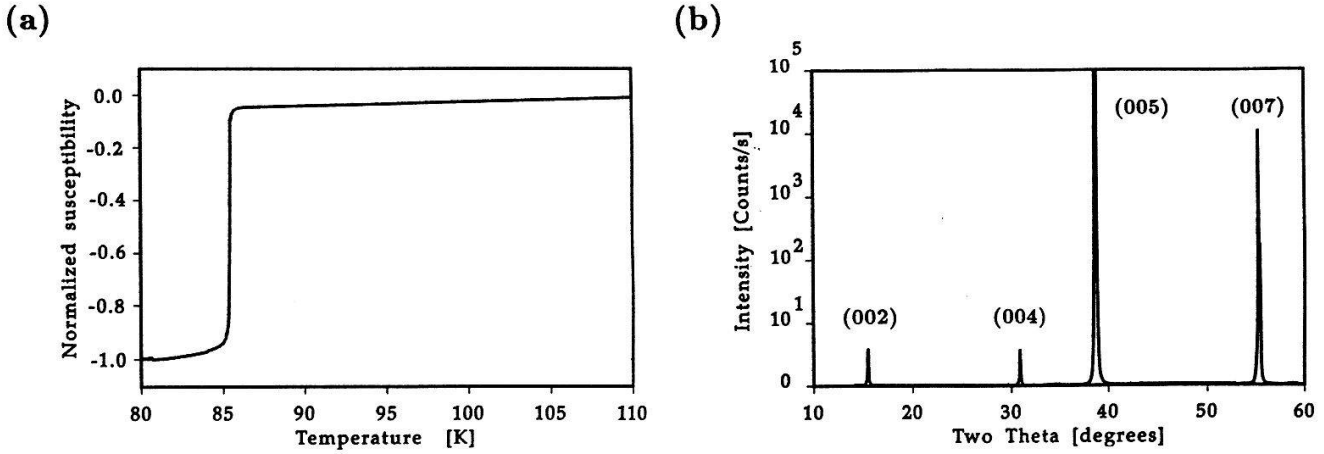

Fig. 1: (a) Temperature-dependent magnetic susceptibility (normalized to the value at 80 K) of a PLD YBCO sample. (b) Cu K_α X-ray diffraction pattern of a YBCO film on $LaAlO_3$(100). The diffraction peak originating from the substrate is not shown.

The critical transition temperature T_c of a typical film was measured by an inductive method. Figure 1a shows the transition to superconductivity at 86 K (onset) with a transition width of 0.5 K (determined from the first derivative of the transition curve). Critical current densities measured by a four-probe electrical transport method range from 1×10^6 to 4×10^6 A/cm^2 at 77 K. X-ray diffraction in conventional Bragg-Brentano geometry ($\Theta - 2\Theta$) exhibits a (001) orientation of the films (see fig. 1b).

Prior to determination of the superconducting properties, the YBCO thin film was investigated by STM in air at room temperature using mechanically prepared $Pt_{90}Ir_{10}$ tips. A tunneling current of 0.3 nA and a tip bias voltage of +1V were applied to image the topography in constant current mode. In contrast to STM images of YBCO films of a thickness of about 150-300 nm [2-4], thicker films (1.2 μm) exhibit a surface structure characterized by a terrace structure with unit cell steps (1.2 nm) and growth pits (marked by an arrow in fig. 2a). Film growth at this stage is dominated rather by regular propagation of flat terraces than by screw dislocation mediated growth. The steps are piled up at the border of growth pits or are annihilated by step propagation. The scanning electron microscopy (SEM) image in fig. 2b of the same sample also reveals such growth pits, whereas the unit cell structure does not provide enough contrast in SEM. A systematic STM study of YBCO films of varying thickness (different growth stages) will be published elsewhere [5].

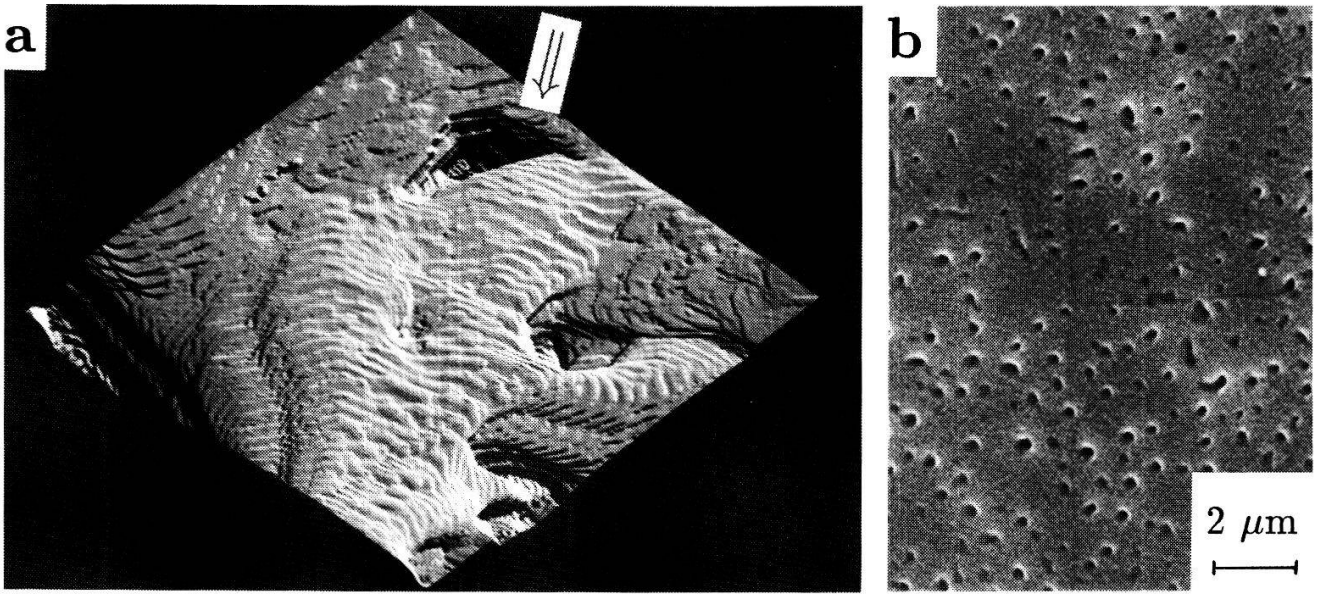

Fig 2: (a) Illuminated representation of a STM image (2 μm $\times$ 2 μm) from the YBCO film characterized in Fig. 1 showing propagating terraces, unit cell steps and growth pits (marked by an arrow). (b) SEM image of the same film (courtesy by E. Zuberbühler and R. Guggenheim, Labor für Rasterelektronenmikroskopie, Universität Basel).

REFERENCES

[1] D. Dijkamp, T. Venkatesan, X.D. Wu, S.A. Shaheen, N. Jisrawi, Y.H. Min-Lee, W.L. Mc Lean and M. Croft, Appl. Phys. Lett. **51**, 619 (1987).
[2] C. Gerber, D. Anselmetti, J.G. Bednorz, J. Mannhart and D.G. Schlom, Nature **350**, 279 (1991).
[3] M. Hawley, I.D. Raistrick, J.G. Beery and R.J. Houlton, Science **251**, 1587 (1991).
[4] H.P. Lang, T. Frey and H.-J. Güntherodt, Europhys. Lett. **15**, 667 (1991).
[5] H.P. Lang, H. Haefke, G. Leemann and H.-J. Güntherodt, Physica C (1992), in print.

Measurements on Langmuir-Blodgett Films by Friction Force Microscopy

R. Lüthi, R.M. Overney, E. Meyer, L. Howald,
D. Brodbeck and H.-J. Güntherodt

Institute of Physics, University of Basel, CH-4056 Basel, Switzerland

A bidirectional force microscope (friction force microscope FFM) of a beam deflection type was built up for experiments at ambient conditions. Normal and lateral forces are measured simultaneously by detecting the deflection of a reflected laser beam with a four-quadrant photodiode. The relation of the topography measured with normal force perpendicular to the surface and the lateral force is discussed. We present FFM measurements on multilayers of Langmuir-Blodgett (LB) films. The friction is largest on the uncovered substrate and is reduced by the LB films acting as lubricant.

The invention of the atomic force microscope (AFM) by Binnig *et al.* [1] which can image insulating surfaces has stimulated the development of new microscopes [2]. We built up an AFM of a beam deflection type [3] with the extension to measure friction which was suggested and described by others previously [4, 5]. Briefly, the interaction between sample and tip causes a deflection of the lever which is sensed by a four-quadrant photodiode acting as a position sensitive detector (PSD). The PSD measures the change of the reflection angle of the laser beam which is focused on the backside of a rectangular lever (figure 1a). The position of the reflected beam on the PSD is measured by the signals: (1) upper quadrants (A) minus lower quadrants (B) and (2) lefthand quadrants (C) minus righthand quadrants (D). The difference signal (A-B) is proportional to the bending and the (C-D) signal is proportional to torsion. The bending is caused by normal forces and torsion by lateral forces. Both forces can be measured simultaneously and independently by the PSD, an adequate electronics and data acquisition system [6]. The presented measurements were performed under ambient conditions and in repulsive force mode. To minimize external vibrations the instrument was operated on a commercially available damping table. During scanning the normal force was kept constant by moving the sample. To optimize the signal, caused by the lateral force, the scan direction was chosen perpendicular to the length side of the lever. Furthermore, we used microfabricated rectangular Si_3N_4-levers with normal spring constants between 0.1 to 0.2 N/m and torsion spring constants of 100 up to 200 N/m to be sensitive enough for lateral forces. This setup allows measurements of 0.1 Å resolution in normal direction and lateral forces of 10^{-10} N in lateral direction. To test our instrument for tribological applications we have chosen Langmuir-Blodgett (LB) films as samples, well-known in tribology as a model system for boundary lubrication. In a previous study it has been shown that molecular resolution can be achieved [7]. The samples were prepared by standard LB techniques transferring 1- and 2-bilayer films of Cd-arachidate to hydrophobized silicon wafers [8]. Fig. 1b) shows a 2×2.5 μm^2 topview image of Cd-arachidate film. The steps on the LB film are determined to be of 54 and 105 Å in height.

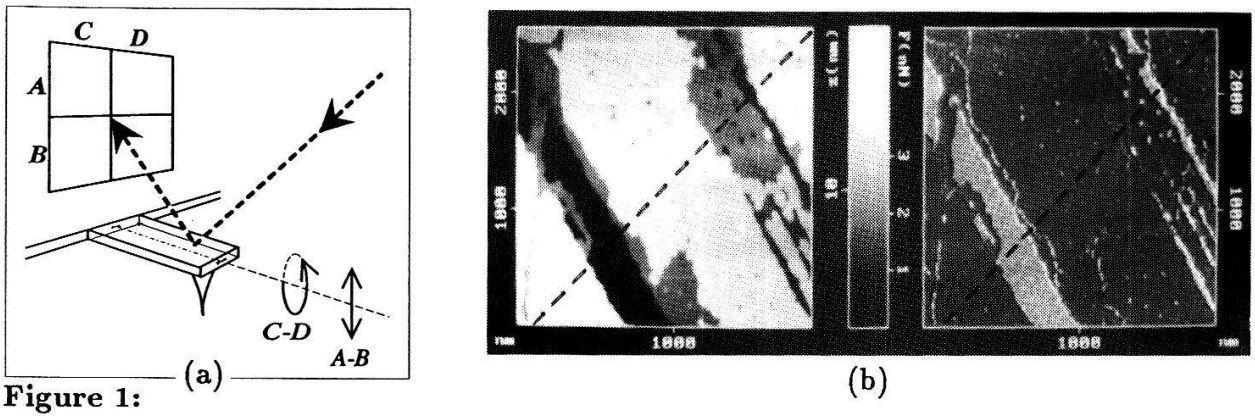

Figure 1:
(a) Principle scheme of the friction force microscope (FFM) using beam deflection technique. (b) The left image shows the topography map, the right image the torsion map. The scan range is $2 \times 2.5\ \mu m^2$. See text for more explanation.

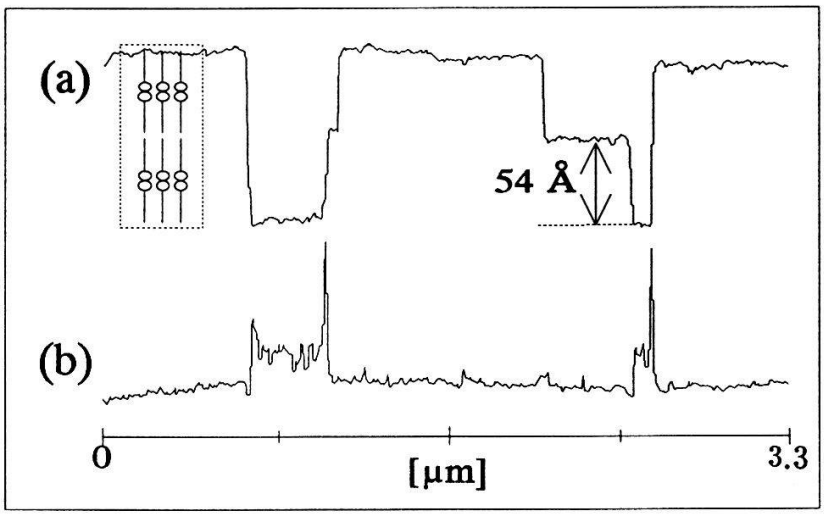

Figure 2:
The section lines along the dashed black line from figure 1b) are shown, (a) from topography and (b) from torsion. Lowest regions in topography are corresponding to regions with largest friction. The dashed inset in (a) shows schematically the arrangement of the Cd-arachidate film.

In the friction image regions with increased friction are observed. They correspond to the lowest regions in the image of topography. However, the friction force remains equal on all terraces of Cd-arachidate bilayers. The higher friction is found on the silicon substrate, lower friction on the Cd-arachidate film which acts as a lubricant. The ratio in friction is 10:1 for silicon compared to Cd-arachidate estimated by analysing the forward and backward scan, known as friction loop. Because of the differences in the friction force, the technique of friction force microscopy allows to distinguish between different materials. Further investigations on mixed LB films were already discussed and described elsewhere [9, 10].

References

[1] G. Binnig, C.F. Quate and Ch. Gerber, *Phys. Rev. Lett.* **56**, 930 (1986).
[2] For a review see: J. Frommer and E. Meyer, *J. Phys.: Condens. Matter* **3**, S1 (1991).
[3] R. Lüthi, *Diploma Thesis*, University of Basel (1991).
[4] G. Meyer and N.M. Amer, *Appl. Phys. Lett.* **56**, 21 (1990).
[5] O. Marti, J. Colchero, J. Mlynek, *Nanotechnology* **1**, 141 (1990).
[6] D. Brodbeck et al., *Ultramicroscopy*, in press (1992).
[7] E. Meyer et al., *Nature* **349**, 398 (1991).
[8] For detailed description of preparation see: M. Schreck et al., *Thin Solid Films* **175**, 95 (1989).
[9] E. Meyer, R.M. Overney, R. Lüthi, D. Brodbeck, L. Howald, J. Frommer, H.-J. Güntherodt, O. Wolter, M. Fujihira, H. Takano, Y. Gotoh, *International Conference of Metallic Compounds and thin Films*, San Diego, April (1992).
[10] R. Overney et al., *submitted*, (1992).

Ein bidirektionales Kraftmikroskop für Oberflächenuntersuchungen im Ultrahochvakuum

L. Howald, R. Lüthi, E. Meyer, H. Haefke, R. Overney,
G. Gerth *, H. Rudin und H.-J. Güntherodt

Institut für Physik, Klingelbergstr. 82, 4056 Basel; *MPI, O-4050 Halle (Saale)

A scanning force microscope for remote controlled operation in ultra high vacuum is described. The normal and lateral forces, acting on the sensor, can be measured simultaneously with the tunneling current between sensor tip and sample. The optical beam deflection detector and the sample position can be adjusted by means of three compact inertial stepping motors.

Das hier vorgestellte Rasterkraftmikroskop (RKM) wurde im Hinblick auf Messungen im Ultrahochvakuum (UHV) entwickelt. Das Instrument ist Bestandteil einer UHV-Anlage, die neben der RKM-Kammer eine Analysen- und eine Präparationskammer umfasst. In der Analysenkammer können LEED- und Auger-Messungen ausgeführt werden. In der Präparationskammer können Proben gespalten und in einer Aufdampfstation dünne Schichten hergestellt werden. Die Proben werden im UHV zwischen den verschiedenen Kammern transferiert.

Der Kraftsensor des Instruments arbeitet nach dem bekannten Prinzip der Laserstrahlablenkung: ein Lichtzeiger wird auf der Rückseite einer einseitig eingespannten, feinen Blattfeder reflektiert und fällt dann auf eine positionsempfindliche Fotodiode. Am freien Ende der Feder ist eine möglichst scharfe Sensorspitze angebracht. Während eine Probe unter der Spitze zeilenförmig bewegt (gerastert) wird, verwertet ein elektronischer Regelkreis die optisch verstärkten Biegebewegungen der Blattfeder als Spannungssignale. Gegenüber anderen Detektionsmethoden hat die Laserstrahlablenkung den Vorteil, dass leicht auch lateral auf die Sensorspitze wirkende Kräfte über Torsionsbewegungen der Blattfeder detektiert werden können [1, 2]. Mit den simultan gemessenen Normal- und Lateralkräften lassen sich Reibungsphänomene auf Nanometerskala studieren [3].

Grund- und Aufriss des Instruments sind zusammen mit einer Legende im nebenstehenden Bild dargestellt. Der Schlitten **8** liegt mit seiner planen Unterseite auf drei Auflagepunkten, von denen zwei mit Piezostellgliedern **9** horizontal bewegt werden können. Werden nun beide Stellglieder gleichzeitig mit einer Sägezahn-Spannung angesteuert, so ziehen sie während der langsamen Auslenkung den Schlitten mit und schnellen anschliessend, unter dem trägen Schlitten hinweg, in ihre Ausgangslage zurück. Die Anpresskraft des Schlittens wird mit Permanentmagneten auf etwa das fünffache Eigengewicht erhöht. Dieser Antrieb kann den Schlitten um mehrere Millimeter in zwei Dimensionen verfahren und um eine vertikale Achse drehen. Die Einzelschritte messen zwischen 5 und 100nm. Nach dem gleichen Trägheitsprinzip arbeiten zwei Schrittmotoren mit Kugelrotor, die im Detektionsteil zwei Planspiegel bewegen [4]. Jeder Spiegel kann um zwei orthogonale Achsen gedreht werden.

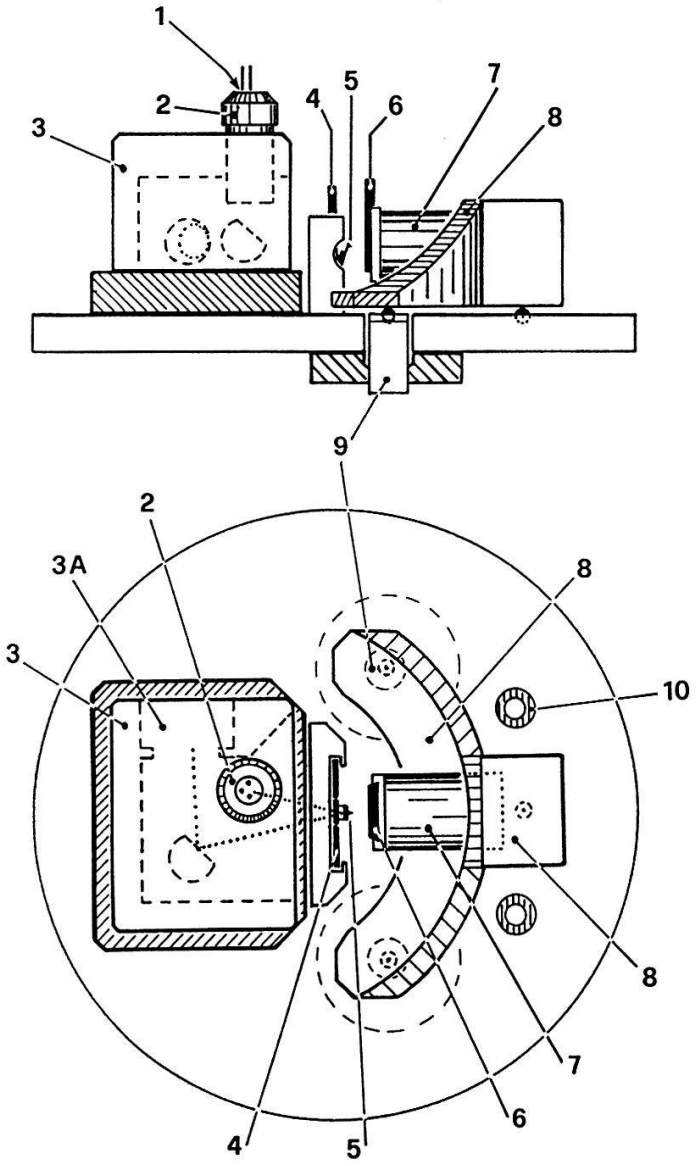

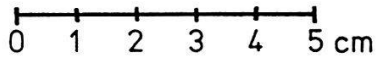

1. Lichtquelle (Laserdiode oder opt. Fiber).
2. Optik, die das Licht auf die Blattfeder fokussiert.
3. Detektorgehäuse, das zwei Umlenkspiegel sowie den Quadranten- Fotodetektor samt Vorverstärker enthält (Hybridschaltung in Schacht **3A**).
4. Auswechselbare Halteplatte für **5**.
5. Blattfeder mit Spitze (Kraftsensor).
6. Auswechselbare Probenhalterung.
7. Röhrenpiezo, auf **8** befestigt, rastert die Probe.
8. Schlitten des Trägheitsantriebs für Grob- und Feinpositionierung der Probe.
9. Zwei Röhrenpiezos, die durch Biegebewegung den Schlitten schrittweise verschieben können.
10. Mechanische Anschläge für den Schlitten (nur im Grundriss eingezeichnet).

Vor einer Messung wird, falls nötig, mit einem Pinzettenmanipulator im UHV eine frische Blattfeder in die Halterung eingeschoben. Danach muss mit den beiden motorisierten Umlenkspiegeln der Strahlengang im Detektionsteil neu justiert werden. Der Schlitten kann nun aus seiner Parkposition heraus (ganz rechts) die Probe gegen den Sensor annähern, bis der Messabstand erreicht ist. Die Halterung der Blattfeder beherbergt einen zusätzlichen Vorverstärker, der gleichzeitige Tunnel- und Kraftmikroskopie ermöglichen wird. Das ganze Instrument sitzt auf einer schwingungsgedämpften Federaufhängung im Innern der RKM-Kammer. Zwei Sichtfenster erlauben die optische Überwachung aller Motorbewegungen.

Referenzen

[1] G. Meyer and N.M. Amer, Appl. Phys. Lett. **56**, 2100 (1990).
[2] O. Marti, J. Colchero and J. Mlynek, Nanotechnology **1**, 141 (1990).
[3] Siehe auch SPG-Beitrag von R. Lüthi et al. in diesem Band.
[4] L. Howald, H. Rudin and H.-J. Güntherodt: " A Piezoelectric Inertial Stepping Motor with Spherical Rotor ", to be published in Rev. Sci. Instrum.

Chain folding of polyethylene observed by SFM

L.M. Eng*, H. Fuchs+, K.D. Jandt++, and J. Petermann++

BASF AG, Polymer Research Laboratory,
ZKM/T - J 543, D-W 6700 Ludwigshafen, Germany.

We report on the investigation of the surface of uniaxially stretched polyethylene (PE) polymer films with the scanning force microscope (SFM). Our SFM results may well be compared with those obtained by transmission electron microscopy showing a stacked lamellar morphology on the μm-scale. High resolution SFM imaging on the crystalline PE lamellae reveals the dense packing of PE polymer chains on the atomic level (pitch height: 0.26 ± 0.02 nm, and interchain separation: 0.50 ± 0.02 nm). Additionally, imaging at the edge of the folded chain lamellar crystals indicated the adjacent reentry of individual PE chains.

Polyethylene (PE) is one of the most important polymeric materials due to its mechanical properties, the processing capabilities and chemical inertness. In many cases the physical and chemical processes at the interface between this polymer and other materials (e.g. biomaterials [1]) determine its use. However, little is known on the surface morphology since most methods conventionally used for the detection of surface properties lack a sufficiently high spatial resolution. The recently developed scanning force microscope (SFM) [2] seems to be well suited for the local inspection of surface properties especially in the case of non-conducting samples. We prepared highly oriented semi-crystalline PE samples by slowly drawing them from the melt. Free standing ultra thin PE films (with a thickness of approximately 20 nm) were deposited onto substrates of highly oriented pyrolytic graphite (HOPG) and carbon coated copper grids for SFM and TEM investigations, respectively.

Fig. 1 presents a SFM image of the ultradrawn PE polymer film taken over a viewing field of 1 x 1 μm^2. The drawing direction crosses the image from top to bottom. The crystalline PE lamellae are clearly visible made up of densely packed folded hydrocrabon chains and aligned perpendicularly to the drawing direction. Due to the preparation conditions (i.e. temperature, concentration, etc.) the lamellae have an uniform thickness of ~30 nm. Their width, however, extends over more than 200 nm and they partially interlock with neighbouring crystals. A TEM study confirmed the stacked lamellar morphology as imaged by SFM on the μm- scale (see inset in Fig. 1) [3]. It further allowed to deduce the orthorhombic unit cell parameters of the densely packed crystalline lamellae in excellent agreement with the bulk lattice spacings known from X-ray diffraction (a = 0.495 nm, b = 0.742 nm, and c = 0.255 nm) [4]. Furthermore, since the [001] direction of the PE film is aligned with the substrate surface, our SFM investigation allowed an analysis of the {hk0} planes of the lamellae on the nm-scale. High resolution SFM

* Université de Genève, Groupe de Physique Appliquée Biomédical, 20, rue de l'Ecole de Médecine, CH-1211 Genève 4, Suisse.

++ TU Hamburg Harburg, Polymer Composites Group, Denickestr. 15, D-W 2100 Hamburg 90, FRG.

+ To whom correspondence should be addressed.

imaging showed (see Fig. 2) that the inter-chain spacing measures 0.50 ± 0.02 nm while the PE pitch height measures 0.26 ± 0.02 nm. Our SFM experiments are thus performed on {h00} crystal planes. In contrast, our recent high-resolution investigation by scanning tunneling microscopy (STM) [5] showed some different packing of the hydrocarbon chains [6] which probably was induced by strong interfacial forces as well as molecular reorientation at the PE/HOPG interface. It should be noted that it is our special kind of sample preparation which allows us to get these lattice planes accessible; solution grown PE single crystals, in contrast, normally attach flat on the substrate surface allowing an investigation of the {001} planes only. When scanning at the edge of single PE lamella, it was even possible to investigate the mechanism of chain folding for which several models [7] and theoretical calculations have been postulated [8]. Our SFM results reveal the adjacent reentry of neighbouring chains as well as a fold period reduction for increasing heights above the substrate surface (in [010] direction) possibly due to a energetically minimized configuration.

In conclusion, high resolution SFM imaging on crystals of the stacked lamellar PE film reveals the dense packing of hydrocarbon chains on the {h00} planes. At the edge of the lamellae, evidence for the adjacent reentry of individual PE chains was found.

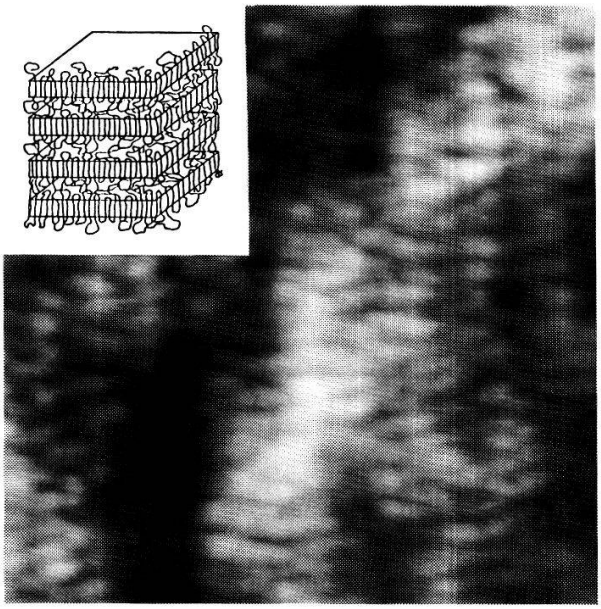

Fig. 1: SFM image of the uniaxially stretched PE polymer surface taken over a 1 x 1 μm² viewing field. The inset in the upper left corner illustrates the stacked lamellar morphology of the PE film.

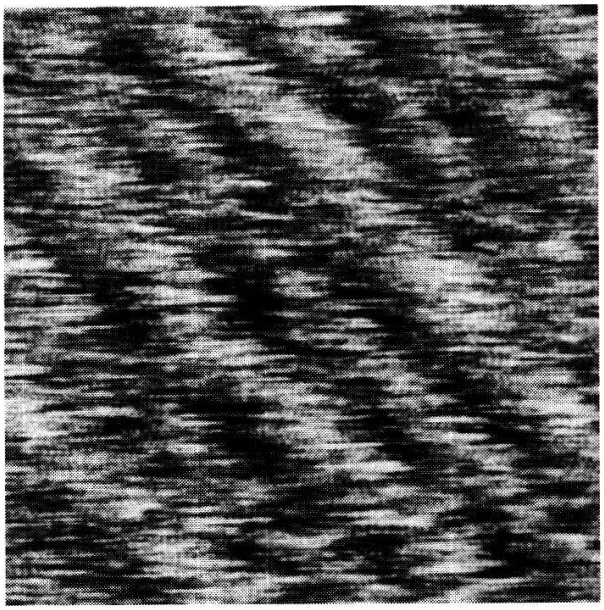

Fig. 2: High resolution SFM image taken over a 2.4 x 2.4 nm² surface area. Note that the pitch height within a single PE chain measures 0.26 ± 0.02 nm while individual PE chains are separated by 0.50 ± 0.02 nm.

References

[1] P. Eyerer, Z. *Werkstofftech.* **17**, 384, 422, 444 (1986).
[2] G. Binnig, C.F. Quate, and Ch. Gerber, *Phys. Rev. Lett.* **56**, 930 (1986).
[3] L.M. Eng, K.D. Jandt, H. Fuchs, and J. Petermann, in preparation.
[4] B. Wunderlich, Crystal Structure, Morphology, Defects, in: *Macromolecular Physics*, Vol.1 (Academic Press, New York, 1973).
[5] G. Binnig and H. Rohrer, *Helv. Phys. Acta* **55**, 726 (1982).
[6] K.D. Jandt, M. Buhk, J Petermann, L.M. Eng, anf H. Fuchs, *Polym. Bull.* **27**, 101 (1991).
[7] F.Khoury and E.Passaglia, The Morphology of Crystalline Synthetic Polymers, in: *Treatise on Solid State Chemistry*, Vol.3: Crystalline and Noncrystalline Solids, ed.: N.B.Hannay (Plenum Press, New York - London, 1976).
[8] P.E. McMahon, R.L. McCullough, and A.A. Schlegel, *J. Appl. Phys.* **38**, 4123 (1967).

Micro- and Nanostructures on Silver Halide Surfaces I. Preparation and Characterization of AgBr Samples

H. Haefke, D. Bürgler, G. Gerth†, L. Howald, E. Meyer, U.D. Schwarz

R. Steiger‡, G. Tarrach and R. Wiesendanger

Institute of Physics, University of Basel, Klingelbergstrasse 82, CH-4056 Basel,
† MPI of Microstructure Physics, D-4050 Halle (Saale), ‡ Ilford AG, CH-1700 Fribourg

We have prepared two types of well-defined AgBr samples as model systems for surface investigations. Both model systems (monodisperse microcrystal ensembles and evaporated thin films) were characterized by IR spectroscopy and XPS, respectively. In the case of thin film preparation the AgBr vapour beam was analyzed by mass spectrometry.

Modern high-sensitivity photographic materials are complex systems consisting mainly of silver halide microcrystals (often called emulsion grains) embedded in a gelatin matrix. The photographic properties of silver halide emulsions (photographic emulsions are dispersions of finely divided silver halide microcrystals in a gel) are strongly affected by the structure and morphology of the microcrystals. Therefore, the characteristic of their surface structures is of considerable importance. Surface defects such as steps, kinks, dislocation ermergences, impurities a.o. are of specific interest because the latent image formation occurs at such defect sites. Due to the complexity of such practical photographic emulsions it is rather difficult to establish experiments which can supply more detailed information on the photographic elementary process. Thus, investigations in this field are connected with the choice of suitable model systems such as single crystals, evaporated thin films and model emulsions. Several types of photographic systems are given in the following block diagram:

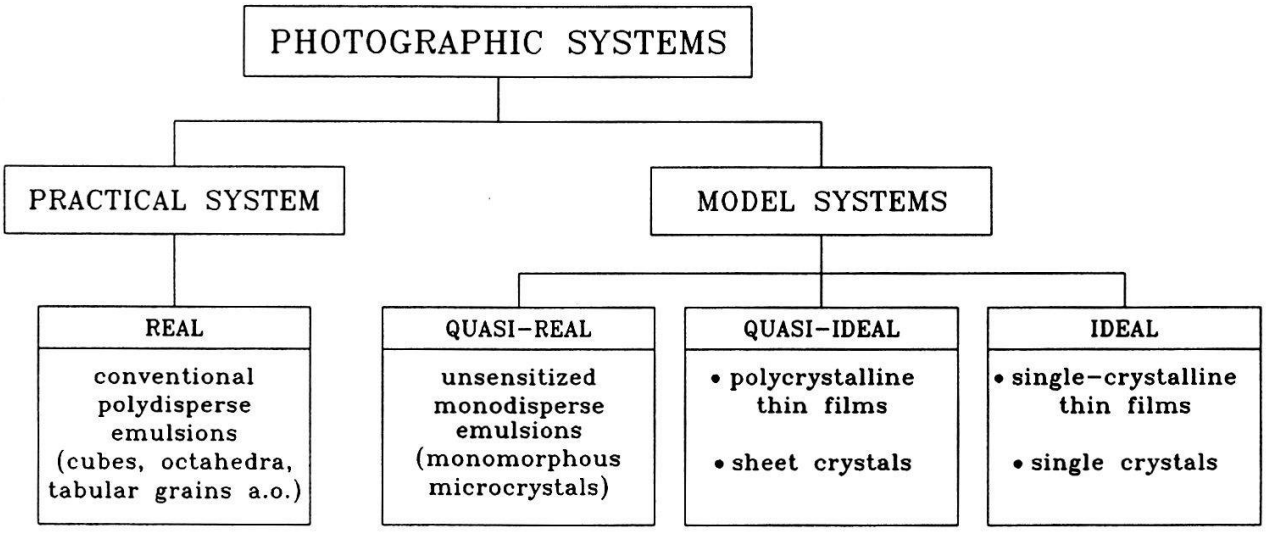

We have studied the surface topography of AgBr microcrystals (bounded by {100} or {111} faces) by atomic force microscopy (AFM) [1] and the growth and surface structure of epitaxial films of AgBr(001) and AgBr(111) by the method of surface decoration and AFM [2]. The aim of this paper is to show the difficulties associated with the sample preparation and necessity of the sample characterization.

Monomorphous AgBr microcrystals were grown by precipitation reactions in cubic, octahedral or tabular habits. The monodisperse model emulsions of gelatin-protected microcrystals were coated on glass substrates and the adhering gelatin was removed by enzymatic degradation. Since remainders of gelatin can distort AFM imaging with the consequence that the top surfaces of the microcrystals seem to be very corrugated. In spite of careful preparation it could not be prevent that infrared spectra of the samples showed occasionally vibrations attributable to small amounts of gelatin [3].

Epitaxial AgBr thin films were grown by vapour deposition on in situ cleaved NaCl and mica crystals in a UHV chamber (base pressure: 8×10^{-11} mbar). Because of the high reactivity of silver halides, especially in the molten state, it was necessary to design a special evaporator. AgBr was evaporated from a platinum effusion cell surrounded by a cooling water jacket so as to allow direct sight to the substrate crystal only by the AgBr melt but not by the hot parts of the evaporator.
The molecular beam of gaseous species effusing from the AgBr evaporator was analyzed by a quadrupole mass spectrometer [4]. Mass spectra covering a mass range of m/e = 20 - 700 amu. The intensities of the ions were measured as function of cell temperature between 500 and 690 °C. The following singly ionized species were identified: Br^+, Ag^+, Br_2^+, $AgBr^+$, Ag_2^+, $AgBr_2^+$, Ag_2Br^+, Ag_3^+, $AgBr_3^+$, $Ag_2Br_2^+$, Ag_3Br^+, $Ag_3Br_2^+$, $Ag_3Br_3^+$ and Ag_4Br_3. The most abundant species in the mass spectra were Ag_3Br^+, Ag_2Br^+ and Ag^+ with the highest relative intensities. Our study does not indicate the appearance of volatile bromides originating from chemical reactions of bromine with parts of the vacuum chamber.
The analysis of the chemical structure of the AgBr films was performed by angle-resolved XPS (Mg K_α radiation) [5]. All samples were mounted in a gold-plated holder. In order to minimize beam damages from x-rays the samples were cooled to about 100 K. The "normal" spectra (escape angle 90°) show, within the limits of experimental uncertainty, that the AgBr films are stoichiometric. However, angle-resolved spectra (escape angles between 50 and 120°) indicate a deficiency of silver ions in the topmost surface layers of the (100) and (111) oriented AgBr films. This is in agreement with the space-charge model of silver halides predicting a negative surface charge due to an excess of bromine ions and a compensating subsurface ionic space charge.

References

[1] U.D. Schwarz et al., Helv. Phys. Acta, this issue.
[2] G. Gerth, L. Howald and H. Haefke, Helv. Phys. Acta, this issue.
[3] R. Steiger, unpublished data.
[4] G. Gerth and H. Haefke, in preparation.
[5] H. Haefke et al., in preparation.

Micro- and Nanostructures on Silver Halide Surfaces II. Morphology of Photographic AgBr Microcrystals

U. D. Schwarz, J. Bohonek†, H. Haefke, T. A. Jung, E. Meyer

R. Steiger† and H.-J. Güntherodt

Institute of Physics, University of Basel, Klingelbergstrasse 82, CH-4056 Basel,
† Ilford AG, CH-1700 Fribourg

AgBr microcrystals from different photographic emulsions were precipitated on a glass substrate and investigated by means of atomic force microscopy. Size and form of individual crystals were determined; on their surfaces, microstructures as well as nanostructures were resolved. Apart from orientated growth hills, we found a superstructure with a period of 5 to 6 nm on the top surfaces of tabular AgBr microcrystals.

The atomic force microscopy (AFM) has proved to be a powerful method of investigating the structure of many kinds of surfaces. The aim of this paper is to demonstrate that AFM is well-suited to image beam sensitive materials such as silver halides with high resolution. Furthermore, our work on AgBr microcrystals extends the AFM's use to the solid components of colloidal systems.

A short introduction in the motivation and problematic of imaging silver halide surfaces by AFM and in the sample preparation is given in Ref. 1. These questions, with special focus on photographic emulsions, will be extensively discussed elsewhere [2,3]. Here, we present results on cubic, octahedral and tabular AgBr microcrystals precipitated from colloidal dispersions on glass substrates.

Fig. 1, 2 and 3 show force micrographs of monodisperse cubic, octahedral and tabular emulsions, respectively. The quadratic (Fig. 1), triangular (Fig. 2) or hexagonal (Fig. 3) shapes of the microcrystals are clearly resolved. Due to the tip shape, the slopes at the edges of the microcrystals reflect the finite aspect ratio of the imaging tip [2,3]. The side lengths of the cubes are determined to be 470 nm $\pm$ 50 nm and the side lengths and the heights of the octahedrons to 550 nm $\pm$ 50 nm and 460 nm $\pm$ 50 nm, respectively. These two values fit quite well with the ideal case that the height of an octahedron should be 0.82 times the side length, what can be derived from geometrical considerations.

The investigated tabular AgBr microcrystals have diameters between 1 and 5 μm and heights between 100 and 400 nm. On their top surfaces, we observed growth hills and surface features of unknown origins (see Ref. 3). At higher magnification, measurements did not yet reveal atomic resolution, but we observed a superstructure (Fig. 4). This superstructure consists of lines in two directions aligned to the $\langle 110 \rangle$ directions of the AgBr lattice. Two-dimensional Fourier analysis (inset in Fig. 4) exhibits periodicities between 5 and 6 nm. We presume that this superstructure has the same origin as the superstructures found before by surface decoration and AFM on vapour-deposited AgBr thin films [4-6].

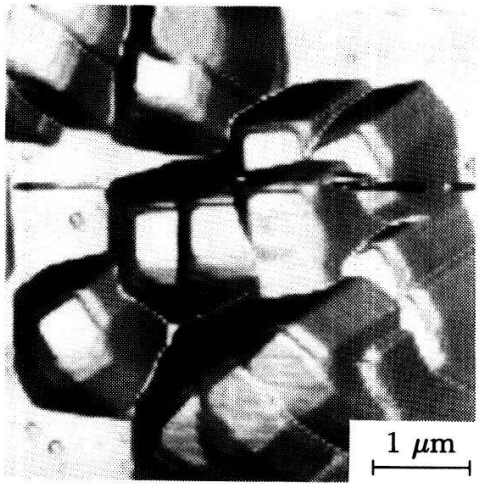

Fig. 1: Cubic AgBr microcrystals. Occasional, the microcrystals are stacked upon each other (lower part of the image).

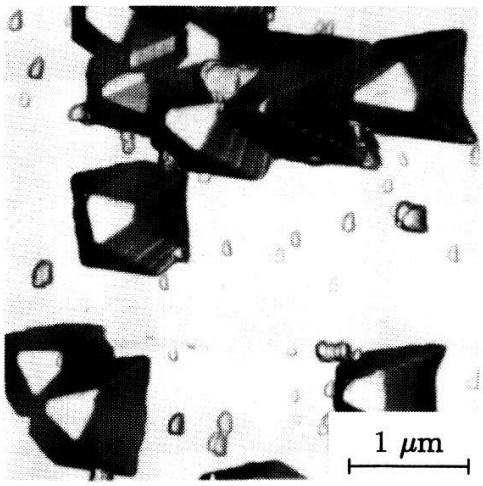

Fig. 2: Octahedral AgBr microcrystals. Only their triangular top surface can be imaged by the AFM tip.

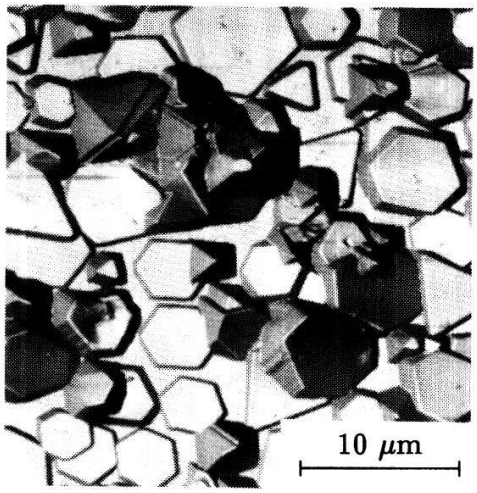

Fig. 3: Tabular AgBr microcrystals. On several of their top surfaces, AFM reveals features of some nanometer in height.

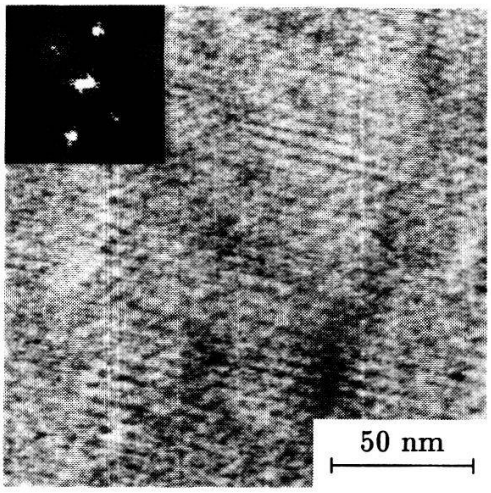

Fig. 4: Superstructure on the (111) top surface of a tabular AgBr microcrystal. The period of the lines is 5-6 nm and their intersection angle 60°. Inset: Two-dimensional Fourier spectrum.

References

[1] H. Haefke et al., Helv. Phys. Acta, this issue.
[2] U. D. Schwarz et al., to appear in J. Imaging Sci.
[3] U. D. Schwarz et al., to appear in Ultramicroscopy.
[4] H. Haefke and M. Krohn, Surf. Sci. Lett. **261**, L39 (1992).
[5] H. Haefke et al., to appear in Ultramicroscopy.
[6] G. Gerth et al., Helv. Phys. Acta, this issue.

Micro- and Nanostructures on Silver Halide Surfaces

III. Growth and Structure of Vapour-Deposited AgBr Thin Films

G. Gerth, M. Krohn†, L. Howald‡ and H. Haefke‡

Max-Planck-Institute of Microstructure Physics, D-4050 Halle (Saale),
† D-4070 Halle (Saale), Murmanskerstrasse 9,
‡ Institute of Physics, University of Basel, CH-4056 Basel

Epitaxial thin films of AgBr(001) and AgBr(111) of well-defined structures produced under suitable choice of substrate and deposition conditions have been examined by the method of surface decoration and atomic force microscopy.

Thin film growth of AgBr on cleavage faces of NaCl and mica have been performed in a UHV chamber.

On NaCl(001) surfaces the single-crystalline AgBr films grow by two-dimensional spreading of atomic steps on their (001) top surfaces [1-3].

On mica(001) substrates the growing three-dimensional islands (cf. Fig. 1) show a liquid-like behaviour on coalescence with their neighbours which is characterized by a regression of the island borders and secondary nucleation in the newly denuded areas. The top surfaces of the AgBr islands are {111} faces and one of their azimuthal <110> directions is parallel to the crystallographic *a*-axis of mica [4]. As this arrangement permits two possible positions being in twin orientation to each other. The finally resulting continuous film (Fig. 2) is (111) oriented but it consists of two different types of twin domains. The twin domains are revealed by grooves at the film surface. In Figs. 1 and 2 the film surface has been characterized by electron microscopy replica technique involving surface decoration by deposition of small gold clusters. At higher magnification (Fig. 2, especially the inset) the gold clusters prove to decorate a hexagonal superstructure [5,6] which we think to be due to the polar character of the AgBr(111) surface. The lattice spacings of the superstructure being near 6 nm is also revealed by atomic force microscopy (Fig. 3a). At higher resolution (Fig. 3b) AFM reveals also the atomic surface lattice of that surface.

References

[1] H. Haefke, M. Krohn and A. Panov, J. Crystal Growth **49**, 7 (1980).
[2] H. Haefke, E. Meyer, H.-J. Güntherodt, G. Gerth and M. Krohn, J. Imaging Sci. **35**, 290 (1991).
[3] E. Meyer, H.-J. Güntherodt, H. Haefke, G. Gerth and M. Krohn, Europhys. Lett. **15**, 319 (1991).
[4] D.W. Pashley, Proc. Phys. Soc. (London) **A 65**, 33 (1952).
[5] J.F. Hamilton and L.E. Brady, Surf. Sci. **23**, 389 (1970).
[6] H. Haefke and M. Krohn, Surf. Sci. **261**, L39 (1992).

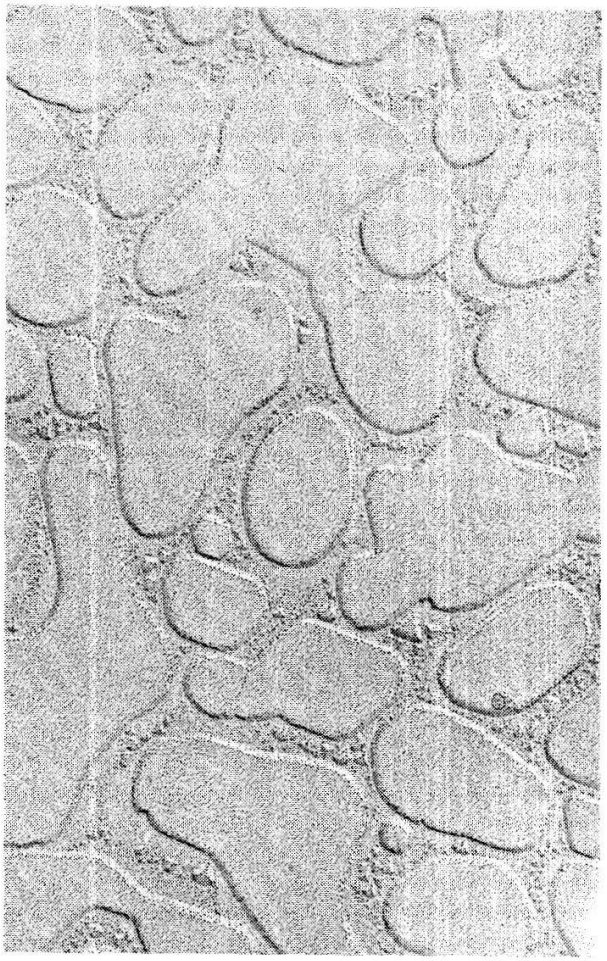

Fig. 1: Coalescence of 3-d AgBr islands growing on mica during UHV vapour deposition at 100 °C.

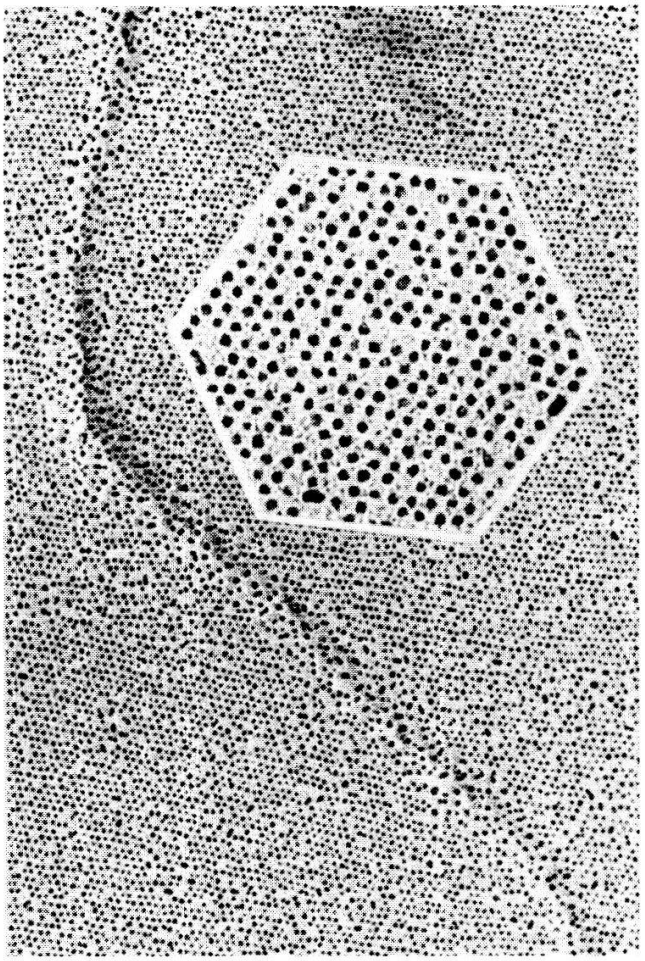

Fig. 2: Twin domains and hexagonal superstructure on the (111) surface of AgBr vapour-deposited at 100 °C on mica.

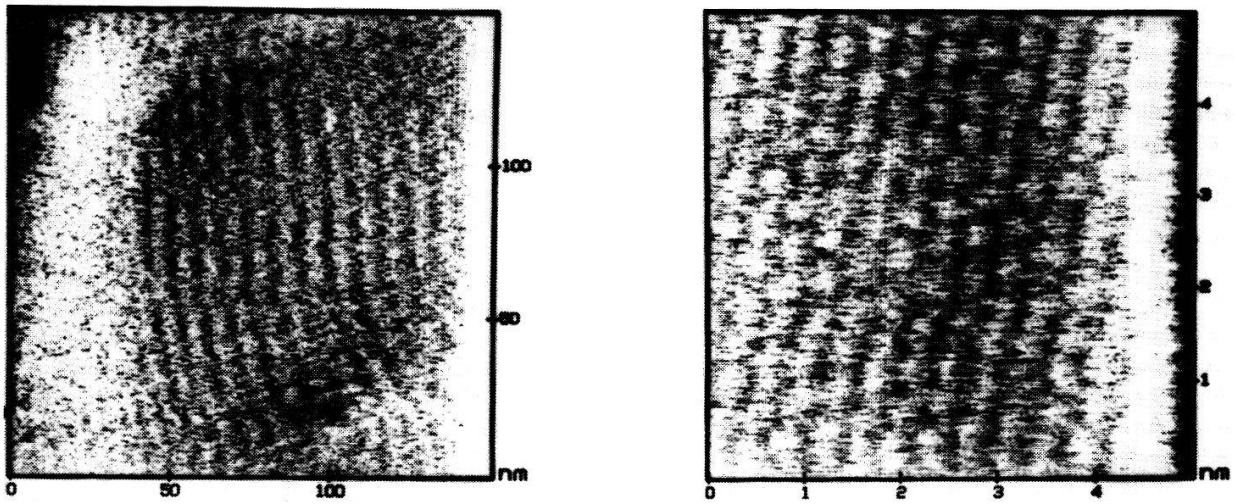

Fig. 3: Structure of (111) surface of AgBr revealed by AFM , a) superstructure, b) atomic structure.

A new pion-nucleon interaction model

P.F.A. Goudsmit, H.J. Leisi and E. Matsinos

Institute for Intermediate Energy Physics, ETH Zürich, CH-5232 Villigen PSI

We show that the GLM model, along with a prescription implementing the unitarity condition, perfectly describes the complete (real and imaginary) s- and p-wave $\pi - N$ amplitude from threshold up to the 33-resonance region, including the $\pi - N$ Σ-term.

We recently introduced a $\pi - N$ interaction model (the 'GLM model') for the description of the $\pi - N$ amplitude in the low-energy region [1,2]. According to our model, the $\pi - N$ interaction proceeds through the t-channel diagrams with scalar-isoscalar and ρ-meson exchanges, as well as the s- and u-channel diagrams with a nucleon or a Δ-isobar in the intermediate state. We have proven that this model can account for the s-wave (up to the 33-resonance region) and for the p-wave (up to pion CM kinetic energy of 80 MeV) $\pi - N$ amplitude, as well as for the $\pi - N$ Σ-term. A completely general treatment of the Δ-isobar (with free variation of the parameter Z, which is associated with the $\pi N \Delta$ interaction) was found to be essential in order to account for the energy dependence of the s-wave part of the $\pi - N$ amplitude.

These results were obtained by supplementing the tree-level calculations with a complex Δ-isobar mass [2]. This supplement, however, does not alter the values of the parameters of our model, as deduced from a fit to the $\pi - N$ phase shifts and other data.

Very recently, Birbrair and Gridnev [3] suggested a somewhat different prescription to implement unitarity in our model; this prescription enables us to extend the (real) tree-level amplitudes $f_\alpha(k)$ toward higher energies:

$$\tilde{f}_\alpha(k) = \frac{f_\alpha(k)}{1 - ikf_\alpha(k)} \tag{1}$$

where α denotes the total isospin and spin of each partial wave and k is the CM momentum of the incident π-meson; the amplitudes $\tilde{f}_\alpha(k)$ have now real and imaginary parts.

In the present work, we demonstrate that the tree-level calculations, supplemented with prescription (1), lead to a perfect description of all the s- and p-wave coefficients of the $\pi - N$ amplitude, from threshold up to the 33-resonance region (see fig. 1).

References

[1] P.F.A. Goudsmit, H.J. Leisi and E. Matsinos, Phys. Lett. **B271** (1991) 290.

[2] P.F.A. Goudsmit, H.J. Leisi and E. Matsinos, submitted to the Physical Review Letters; ETHZ-IMP PR/92-4 (February 1992).

[3] B.L. Birbrair and A.B. Gridnev, private communication (March 1992); P.F.A. Goudsmit, H.J. Leisi, E. Matsinos, B.L. Birbrair and A.B. Gridnev, in preparation.

[4] O. Dumbrajs et al., Nucl. Phys. **B216** (1983) 277; corrected by a factor of two (G.C. Oades, private communication).

[5] R. Koch and E. Pietarinen, Nucl. Phys. **A336** (1980) 331.

[6] D.V. Bugg, private communication (November 1991).

Figure 1. The energy dependence of the s- and p-wave coefficients of the real part of the $\pi - N$ amplitude for $g_\rho^{(V)} = 5.26$ [4] (ε denotes the kinetic energy of the π-meson in the CM system). The data, shown, correspond to Koch's [5] (crosses) and Bugg's [6] (diamonds) phase-shift results. The solid lines represent the predictions of the GLM model. The six parameters of the model were obtained from a fit to Koch's phase shifts in the energy interval 15 MeV $< \varepsilon <$ 70 MeV.

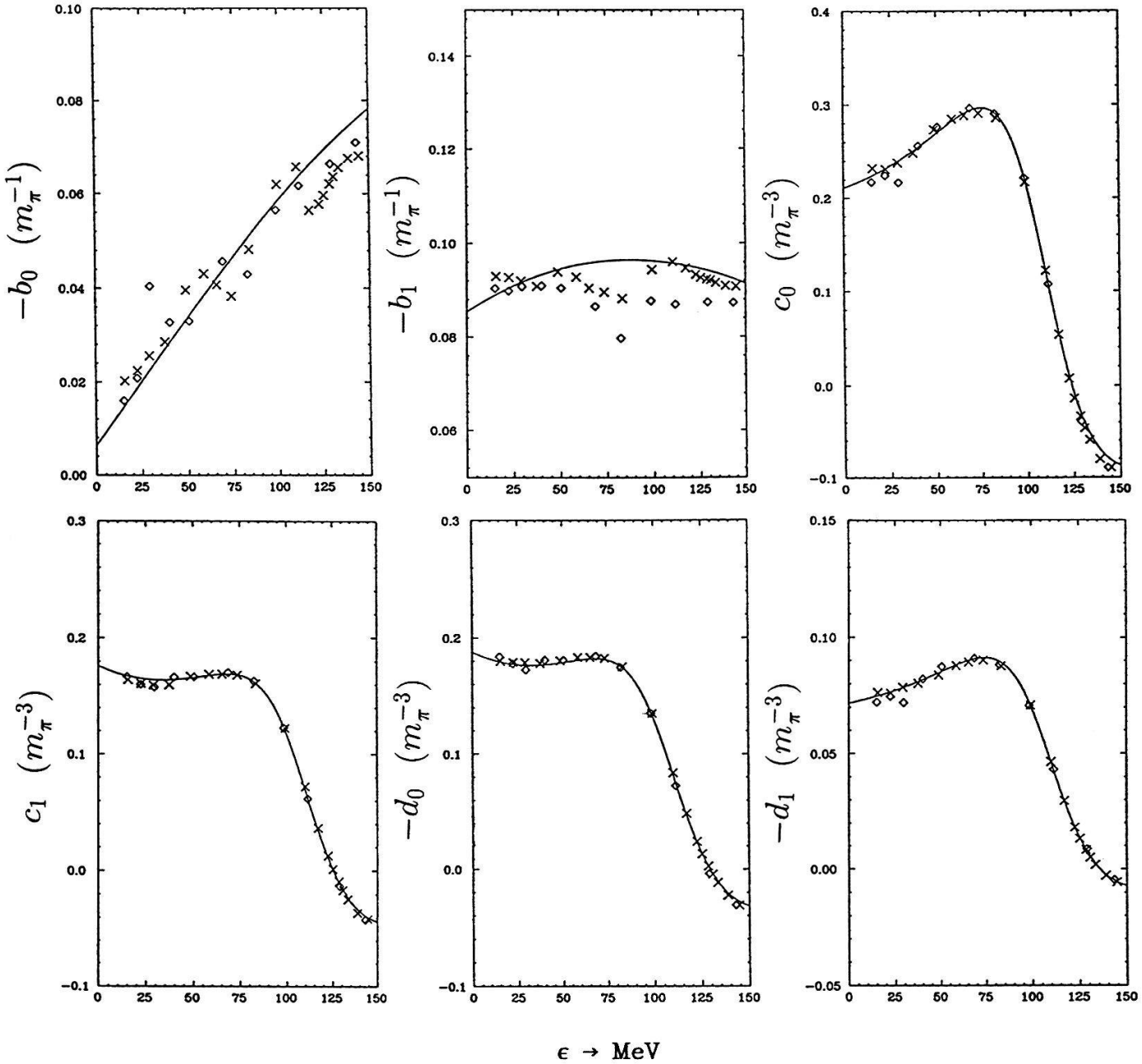

SPIN CORRELATIONS IN NEUTRON-PROTON SCATTERING.

R. Binz°, B. van den Brandt•, R. Büchle°, M. Daum•, Ph. Demierre*, J. Franz°, G. Gaillard*, N. Hamann*, R. Hess*, J.A. Konter•, C. Lechanoine–Leluc*, F. Lehar#, S. Mango•, R. Peschina°, D. Rapin*. E. Rössle°, P.A. Schmelzbach•, H. Schmitt°, R. Todenhagen°

(o) Fakultät für Physik der Universität Freiburg, D-7800 Freiburg, Germany,
(⋆) DPNC, University of Geneva, CH 1211 Geneva, Switzerland,
(•) PSI, Paul Scherrer Institut, CH 5234 Villigen-PSI, Switzerland,
(∗) CERN, on leave from Fakultät für Physik der Universität Freiburg,
(#) DAPNIA, CEN-Saclay, F-91191 Gif-sur-Yvette, France

Abstract

This paper presents a short overview of the neutron-proton results obtained with the polarized neutron beam created at PSI in the nE1 beam line.

The experimental information on the neutron-proton scattering is still rather poor as compared to the proton-proton case, due to the lack of good polarized data [1]. Only recently the situation began to change, and one can expect more high-precision polarization data in the near future, especially from Saclay above 800 MeV [2] and from the Paul Scherrer Institut (PSI) below 600 MeV [3]. At PSI, the new polarized neutron beam facility NA2 became operational in march 1992 [4]. The design of this new beam line is based on the extensive study performed on the SIN-PSI nE1 beam since 1986 [5]. This polarized neutron beam nE1 was produceded successfully using a longitudinal spin transfer of the 590 MeV proton beam on a carbon target, by the charge exchange reaction $C(\vec{p},\vec{n})X$ at 3.4°. The beam polarization was about 50% near 500 MeV and as low as 20% near 200 MeV [6]. This beam was used to measure the analyzing power $A_{no}(T,\theta)$, the spin correlation parameters $A_{nn}(T,\theta)$, $A_{ss}(T,\theta)$, $A_{kk}(T,\theta)$ and $A_{sk}(T,\theta)$ in elastic np scattering, and the spin dependent cross section differences $\Delta\sigma_L(T)$ and $\Delta\sigma_T(T)$ [7]. T is the beam energy and θ is the cm scattering angle of the neutron. The results at 540 MeV are presented below, in the notations of ref. [8].

The analyzing power and the spin correlation parameters have been measured with the neutron beam polarized either vertically (P_{bn}), transversally (P_{bs}) or longitudinally (P_{bk}). The polarized proton target consisted of 8 cm^3 butanol (PPT) and was polarized either vertically or horizontally. A two-arm spectrometer covered the angular range of the backward scattering and observed both, the recoil proton (trajectory and TOF) using four drift chambers and scintillation counters, and the scattered neutrons (direction and TOF) using eight scintillator bars of 8x20x130 cm^3. The neutron beam energy spectrun is continuous and the energy of each incoming neutron has to be measured using its TOF relative to the rf-signal (17 or 50 MHz) of the accelerator. The energy domain of the experiment, 100-580 MeV, was divided into six bins centered at 140, 220, 300, 380, 460 and 540 MeV. The analysis was mainly performed by R. Peschina [9]. Figure 1 shows the results for the A_{nn}, A_{ss}, A_{kk} and A_{sk} parameters at 540 MeV together with the other existing data and with phase shifts analysis predictions (PSA). Our results at lower energies, not shown here, have larger errors due to the lower beam polarization.

The spin dependent cross section differences $\Delta\sigma_L$ and $\Delta\sigma_T$ [10], and of the spin correlation parameters $A_{nn}(180^o)$ and $A_{kk}(180^o)$ were also measured. Then, using these four quantities and σ_o and $I_o(180^o)$, the spin independent total and differential cross-sections, R. Binz reconstructed directly, *for the first time*, the three non zero helicity amplitudes of the n-p scattering at 180°, ϕ_1, ϕ_2 and ϕ_4 [6]. 0° and 180° are closely related by the isospin decomposition, $\phi^{np} = 0.5(\phi^{I=1} + \phi^{I=0})$, and by the symmetry properties of the amplitudes. The $\mathrm{Im}(\phi^{I=1})$ were taken from the proton-proton scattering. Three additional signs ambiguities were removed by assuming that the sign of

the spin transfer parameters $K_{on"no}(180°)$ and $K_{ok"ko}(180°)$ for the free np scattering is the same as the one for the quasi-elastic scattering in the charge exchange reaction $C(\vec{p},\vec{n})X$ [5]. Figure 2 shows the amplitudes reconstruction at 540 MeV as well as the PSA predictions. These amplitudes are almost real and a large discrepency with the PSA is found for the real part of ϕ_4.

This work has been partly funded by the Federal Minister for Research and Technology (BMFT) under the contract No 06 FR 263 I, and by the Fonds National Suisse pour la Recherche Scientifique.

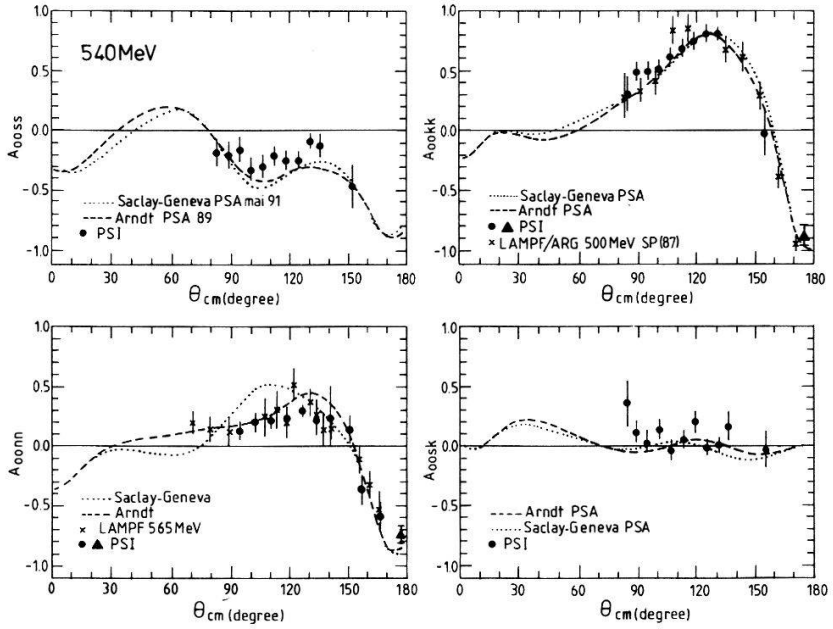

Fig. 1. Measurements of the spin correlation parameters A_{nn}, A_{ss}, A_{kk} and A_{sk} in elastic np scattering integrated between 500 and 580 MeV. Our error bars are statistical only. We corrected for the sign of A_{sk} (=- A_{XZ}) in the predictions of the Arndt's PSA because of the conventions.

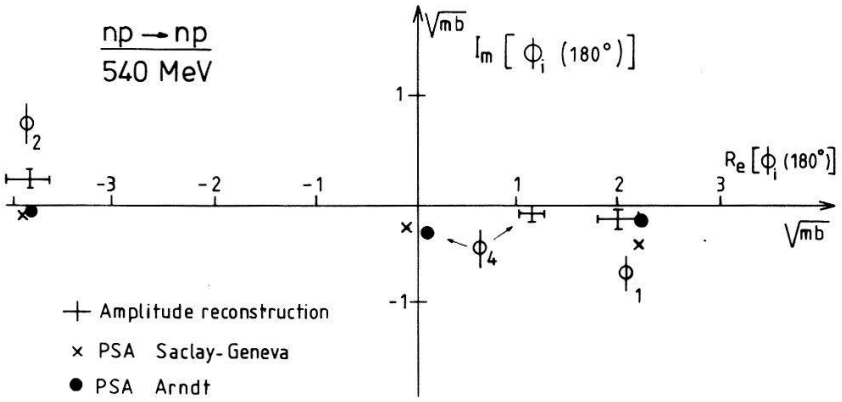

Fig. 2. The direct reconstruction of the three non zero helicity amplitudes of the n-p scattering ϕ_1, ϕ_2 and ϕ_4 at 180° and 540 MeV (see the text).

[1] C. Lechanoine-Leluc et al., *Journal de Physique* (Paris) **48** (1987) 985.
[2] J. Ball et al., LNS-Saclay Proposal 1991 N° 225.
[3] R. Binz et al., PSI-NA1-Proposal R 87-12.1 (1987).
[4] A. Amidouch et al., *PSI Annual Report* (1991) Annex I.
[5] R. Binz et al., *SIN Newsletter* **19** (1987) NL48, SIN Jahresbericht 1986.
[6] R. Binz, Ph.D Thesis, Fakultät für Physik der Universität Freiburg, (1991).
R. Binz et al., *Physics Letters* **B231** (1989) 323.
[7] R. Binz et al., *Nucl. Phys.* **A508** (1990) 276c.
R. Binz et al., *PSI Annual Report* (1990) Annex I, p. 37, p. 39 and p.41.
[8] J. Bystricky et al., *Journal de Physique* (Paris) **45** (1984) 207.
[9] R. Peschina, Ph.D Thesis, Fakultät für Physik der Universität Freiburg, (in preparation).
[10] R. Binz et al., *Nucl. Phys.* **A533** (1991) 601.

Continuous-Time Limit for Maps with Colored Noise

P. Reimann and P. Talkner

Paul Scherrer Institut, CH-5232 Villigen and
Institut für Physik, Klingelbergstr. 82, CH-4056 Basel

Nonlinear dynamical systems under the influence of colored noise have attained considerable interest in recent years. In spite of the great effort important properties of this problem are still not yet understood [1].

As a particular model we consider a particle with coordinate x moving in an external potential $V(x)$ under the influence of an exponentially correlated random force

$$\dot{x} = -V'(x) + \tau^{-1/2} y \quad , \quad \dot{y} = -\tau^{-1} y + \sqrt{2D\tau^{-1}}\,\xi(t) \tag{1}$$

where $\xi(t)$ is Gaussian white noise, τ denotes the correlation time, and D the strength of the colored noise $\tau^{-1/2}y$. For $V(x)$ we choose a continuously differentiable piecewise parabolic symmetric double well potential [2] with wells at $x = \pm 1$ and a barrier at $x = 0$. The well and barrier frequencies are denoted by $\omega_0^2 = V''(\pm 1)$ and $\omega_b^2 = -V''(0)$, respectively.

By discretization of the time t we obtain a two-dimensional noisy map

$$x_{n+1} = x_n - aV'(x_n) + y_n \quad , \quad y_{n+1} = A\,y_n + \sqrt{\epsilon/2}\,\xi_n \tag{2}$$

where a denotes the time step and ξ_n are independent Gaussian random numbers with vanishing mean and unit correlation. Further we defined $x_n := x(na)$, $y_n := \tau^{-1/2} a y(na)$, $A := 1 - a\tau^{-1}$, and $\epsilon := 4D\tau^{-2}a^3$.

In this note we consider the invariant density $W(x,y)$ of the process (2) in the limit of weak noise ϵ and vanishing time step a. In the limit of weak noise $W(x,y)$ becomes

$$W(x,y) = Z(x,y)\ \exp\{-\Phi(x,y)/\epsilon\} \tag{3}$$

where $\Phi(x,y)$ denotes the generalized potential and $Z(x,y)$ the prefactor. For an arbitrary but finite a, the generalized potential $\Phi(x,y)$ may be determined by means of an implicit variational principle [3].

With

$$\phi(x,y)/D := \lim_{a\to 0} \Phi(x, y\cdot a/\sqrt{\tau})/\epsilon \tag{4}$$

we find the central result

$$\phi(x,y) = \frac{1}{2} \min_{\lambda \geq 0, \Theta = \pm 1} \{b_\lambda (x e^{-\lambda\tau\omega_b^2} + \Theta)^2 + (1 - b_\lambda c_\lambda^2)^{-1} (y - b_\lambda c_\lambda (x e^{-\lambda\tau\omega_b^2} + \Theta))^2\} \quad . \tag{5}$$

The coefficients b_λ and c_λ are defined by

$$b_\lambda = \left(\frac{1}{2\,\Delta\phi} + \frac{2\tau^2\,(\omega_b^2+\omega_0^2)\;e^{-\lambda(1+\tau\omega_b^2)}}{(1+\tau\omega_b^2)(1-\tau\omega_b^2)(1+\tau\omega_0^2)} - \frac{e^{-2\lambda\tau\omega_b^2}}{\omega_b^2(1-\tau\omega_b^2)} \right)^{-1}$$

$$c_\lambda = \frac{\tau^{1/2}\;e^{-\lambda\tau\omega_b^2}}{1-\tau\omega_b^2} - \frac{\tau^{3/2}\;(\omega_b^2+\omega_0^2)\;e^{-\lambda}}{(1-\tau\omega_b^2)(1+\tau\omega_0^2)} \qquad (6)$$

where $\Delta\phi$ denotes the difference of the generalized potential at the barrier and the well

$$\Delta\phi = (V(0)-V(1))\;\left(1+\frac{\tau^2\;\omega_b^2\;\omega_0^2}{1+\tau\,(\omega_b^2+\omega_0^2)}\right) \quad . \qquad (7)$$

Whereas this result (7) agrees with [2], the reduced potential $\phi(x)$ derived from (5) does slightly differ from the findings in [2]. Because of singularities in the higher derivatives of the potential $V(x)$ Eq.(7) cannot be conferred to the results of [4] as far as the corrections to the leading order expressions in the limiting cases of small and large correlation time are concerned.

The generalized potential (5) approaches the correct parabolic behavior near the stable fixed point [5]

$$\phi(1+x,y)-\phi(1,0) = \frac{1}{2}(1+\tau\omega_0^2)(\omega_0^2x^2+(\sqrt{\tau}\omega_0^2x-y)^2) \quad . \qquad (8)$$

As long as $\tau\omega_b^2 < 1$ the same form of $\phi(x,y)$ holds also near the unstable fixed point with ω_0^2 replaced by $-\omega_b^2$. When $\tau\omega_b^2 > 1$ the generalized potential becomes non-analytic. For the reduced potential $\phi(x)$ one obtains from (5) for small x-values $\phi(0)-\phi(x) \propto |x|^{1+\omega_b^2\tau}$ in agreement with [2], [4] and with [5] in the large τ limit. In the limit of small correlation time the known form of $\phi(x)$ [6] is recovered from (5).

The prefactor $Z(x,y)$ is constant for $\tau = 0$ and has a minimum at the unstable fixed point for $\tau > 0$. From this fact in combination with the above mentioned behavior of the generalized potential it is possible to show that for $\omega_b^2\tau > 1$ the invariant density has no longer a saddle at the unstable fixed point but a relative minimum for small enough noise strengths D. This explains the phenomenon known as 'holes in the invariant density' observed in numerical simulations [7].

It can be shown that the above results qualitatively hold true for more general potentials $V(x)$.

References

[1] P.Hänggi, P.Jung, F.Marchesoni, J.Stat.Phys.**54**, 1367, 1989.
[2] J.F.Luciani, A.D.Verga, Europhys.Lett.**4**, 255, 1987.
[3] P.Reimann, P.Talkner, Phys.Rev.A **44**, 6348, 1991.
[4] A.J.Bray, A.J.McKane, T.J.Newman, Phys.Rev.A **41**, 657, 1990.
[5] H.Gang, L.Zhi-heng, Phys.Rev.A **44**, 8027, 1991.
[6] H.S.Wio et al., Phys.Rev.A **40**, 7312, 1989.
[7] G.Debnath et al., Phys.Rev.A **42**, 703, 1990.

Probability and Obejective Events in Quantum Mechanics

Markus Simonius

Inst. f. Mittelenergiephysik, Eidg. Techn. Hochschule, CH-8093 Zürich, Switzerland

The problem of measurement in quantum mechanics is reanalyzed within a general, strictly probabilistic framework (without reduction postulate). Based on a novel comprehensive definition of measurement the natural emergence of objective events is demonstrated and consistency in spite of superpositions is pointed out.

The object of this note is to point out that, besides the *probability* for the occurrence of events in a given arrangement, quantum mechanics can consistently represent also the individual objective events themselves, where *the basic property defining an event and guaranteeing its objectivity, is, that it can be observed or read in at least two independent, mutually non-interfering ways with necessarily agreeing results.*

General Framework.— To a given system belongs a set $\mathcal{S}$ of states, a set $\mathcal{O}$ of observables and a function $(\cdot,\cdot) : \mathcal{O} \times \mathcal{S} \to [0,1]$ interpreted as probability $(A,X) = Prob(e=1)$ for the occurrence of an event $e \in \{0,1\}$ in a single observation or *trial* on a state $X \in \mathcal{S}$ with a given observable $A \in \mathcal{O}$ where $e=1$ means that the event occurs and $e=0$ that it does not. Conventionally $(A,X) = Tr[AX]$ where A and X are hermitian operators on an appropriate hilbert space $\mathcal{H}$ obeying $0 \leq A \leq 1$ and $0 \leq X$, $Tr[X]=1$, respectively, with Tr denoting the trace over $\mathcal{H}$. $\mathcal{O}$ and $\mathcal{S}$ are mutually separating. To each $A \in \mathcal{O}$ a complement $\bar{A} \in \mathcal{O}$ exists which is defined by $(\bar{A},X) = 1-(A,X)\ \forall X \in \mathcal{S}$ (and thus connected to A by the replacement of the event e by its negation $(1-e)$).

$\mathcal{S}$ is convex under classical (incoherent) mixing: $X_1, X_2 \in \mathcal{S}$ implies $X = |c_1|^2 X_1 + |c_2|^2 X_2 \in \mathcal{S}$ with $(A, |c_1|^2 X_1 + |c_2|^2 X_2) = |c_1|^2 (A,X_1) + |c_2|^2 (A,X_2)\ \forall A \in \mathcal{O}$ where $|c_1|^2 + |c_2|^2 = 1$ here and throughout the following.

Discrimination and Interference.— An observable $A \in \mathcal{O}$ *discriminates* between two states $X, Y \in \mathcal{S}$ if $(A,X)=1$ and $(A,Y)=0$ or vice versa and thus if $|(A,X)-(A,Y)|=1$. If such an observable exists X and Y are *orthogonal.* A state X is a *(general) superposition* of two orthogonal states X_1 and X_2 with some fixed weights $|c_1|^2$ and $|c_2|^2$ if

$$(A,X) = |c_2|^2 (A,X_2)\ \ \forall A : (A,X_1) = 0 \ \text{ and } \ (A,X) = |c_1|^2 (A,X_1)\ \ \forall A : (A,X_2) = 0. \quad (1)$$

The (convex) set of all states X with this property is denoted by $\mathcal{S}(|c_1|^2 X_1, |c_2|^2 X_2)$. It contains the incoherent mixture $|c_1|^2 X_1 + |c_2|^2 X_2$. An observable A is *insensitive to interference* between X_1 and X_2 if $(A,X) = (A, |c_1|^2 X_1 + |c_2|^2 X_2)\ \forall X \in \mathcal{S}(|c_1|^2 X_1, |c_2|^2 X_2)$.

Measurements.—In a measurement an object undergoes some interaction or interactions with one or several other systems acting as probes or measuring devices etc. such that afterwards there are at least two separated channels (identified by greek upper indices) consisting of different systems on which mutually undisturbing observations, using channel observables or *readings* $A^\mu \in \mathcal{O}^\mu$, $\mu = 1,2,...$, may be performed in order to obtain information on the object. In a single measurement or trial on a fixed initial state $X \in \mathcal{S}$ of the object one can obtain simultaneously a set of events $\{e^\mu\}$ corresponding to fixed readings A^μ, one for each channel μ separately. These events can be combined to give *coincidence events*

$\prod e^\mu$, $\mu \in M$ where M denotes a subset of channels. The measurement is characterized by a function $m(\{A^\mu,\ \mu \in M\}; X)$, also denoted $m(A^1; X)$ or $m(A^1, A^2; X)$ etc., which depends on the readings A^μ, $\mu \in M$ and the initial state $X \in \mathcal{S}$ of the object and is interpreted as the probability for such coincidences, $m(\{A^\mu, \mu \in M\}; X) = Prob(\prod_{\mu \in M} e^\mu = 1)$. It completely specifies the measurement including dependence on initial states of probes or measuring devices etc. The function m extends to arbitrary observables on the total final state of the measurement and has the following *defining properties:*

[0] $m(; X) = 1\ \forall X \in \mathcal{S}$ (no reading). [1] $0 \leq m \leq 1$.

[2] Convex linearity in $X \in \mathcal{S}$ as for (A, X).

[3] Linearity in the final state observables.

[4] Separability or mutual non-disturbance of readings of different channels expressed by

$$m(A^\mu, A^\nu; X) + m(A^\mu, \bar{A}^\nu; X) = m(A^\mu; X) \tag{2}$$

$(\mu \neq \nu)$ for all $A^{\mu,\nu} \in \mathcal{O}^{\mu,\nu}$ independent of A^ν, and correspondingly for an arbitrary number of channels or A^μ and A^ν replaced by observations on any two disjoint sets of channels. Here the l.h.s. means that the event corresponding to A^ν is ignored though it has been obtained, and the r.h.s that no observation of channel ν is performed at all.

Measurements can be composed, the number of channels enlarged, and information transmitted to new ones by performing measurements on channels of previous ones. Upon reading the "reader", whether photon or human being, herself becomes a channel.

Discriminating Measurements and Objectivity.— A channel μ of a measurement *discriminates* between two states X_1 and X_2 (requiring X_1 and X_2 to be orthogonal) if reading of that channel alone, without further observation, allows one to discriminate between X_1 and X_2. A corresponding reading A^μ *discriminates* X_1 *against* X_2 if $m(A^\mu; X_i) = \delta_{i1}$.

From eqs. (1) and (2) and the fact that for fixed readings A^μ, $\mu \in M$ a measurement realizes an observable $A \in \mathcal{O}$ such that $(A, X) = m(\{A^\mu,\ \mu \in M\}; X)$ one obtains

Theorem *Consider a measurement with channels $\mu \in M$ which discriminate between two states X_1 and X_2 and readings A^μ, $\mu \in M$, which discriminate X_1 against X_2. Then*

$$m(A^\mu, \bar{A}^\nu; X) = m(\bar{A}^\mu, A^\nu; X) = 0 \quad \forall X \in \mathcal{S}(|c_1|^2 X_1, |c_2|^2 X_2),\ \mu, \nu \in M,\ \mu \neq \nu \tag{3}$$

implying that for all $X \in \mathcal{S}(|c_1|^2 X_1, |c_2|^2 X_2)$ two such readings agree with probability one.

Corollary (Objective Events) *A measurement which discriminates between two states X_1 and X_2 performed on any superposition X between them produces, for each trial, a result, stored in its discriminating channels, which constitutes an (objective) event for an observable A which discriminates between X_1 and X_2. This event can be obtained or read from each discriminating channel of the measurement separately.*

Thus objective events as defined in the introduction emerge automatically from an appropriate definition of mesurements within a strictly probabilistic formulation. Only the response of each channel seperately to the two states X_1 and X_2 is presupposed and nothing about superpositions between them nor about correlations among different channels.

In contradistinction to other approaches the definition and emergence of objective events is compatible with the in priciple observability of interference effects at any time. While a complete discussion of this would exceed space limitations, the rational behind it is in fact very simple: *One just cannot violate the defining equations (1) of superpositions however complicated one chooses the arrangement for an observation to be.*